Electrically Pumped Vertical-Cavity Amplifiers

Greibe, Tine

Publication date:
2007

Document Version
Publisher's PDF, also known as Version of record

Ph.D. Thesis

Electrically Pumped Vertical-Cavity Amplifiers

Tine Greibe
Nanophotonics
Department of Communication, Optics and Materials
Ørsteds Plads 345V
DK-2800 Kgs. Lyngby
Denmark

COM•DTU

Acknowledgment

I would like to thank my former supervisor, Dan Birkedal, now at *Alight Technologies, Farum, Denmark*, for giving me the chance to do research in the field of Nanophotonics at COM· DTU. I am especially grateful to my present supervisors Associate Professor Kresten Yvind and Professor Jørn M. Hvam for adopting me and my project and for giving me very qualified supervision.

I would like to thank Claus B. Sørensen, Niels Bohr Institute, Copenhagen University, for great help with the MBE-growth of the NBI-wafer. Also, thanks to Optical Research Center, Tampere University, Finland, for growing of wafer.

Great thanks to Benjamin Rudin, Aude-Reine Bellancourt, Deran Maas and Heiko Unold, Swiss Federal Institute of Technology, Zürich, for collaborating on the processing of the NBI-wafer.

Thanks to Mike Van der Poel and Peter Uhd Jepsen for help with characterisation of saturable absorbers and to Svend Bischoff, *Alight Technologies*, for helping with the *SILVACO*-simulations. Thanks to Jens Adler Nielsen for *many* fruitful discussions.

I would like to thank the group of Nanophotonics for a great atmosphere, we have had many nice lunch sessions and outstanding ice-cream moments. Thank you for taking care of my intake of saccharose, I really appreciate that.

Thanks to family and friends for listening to *numerous* lectures and slide-shows on interesting laser technology and semiconductor physics. Thank you for being there, all ears, when I needed you.

Jeg kunne *aldrig* have gjort det uden dig, Jens.

Abstract

In this work, the design of electrically pumped vertical-cavity semiconductor optical amplifiers (eVCAs) for use in a mode-locked external-cavity laser has been developed, investigated and analysed.

Four different eVCAs, one top-emitting and three bottom-emitting structures, have been designed and produced, of which only the top-emitting was tested in an external laser cavity. The other designs have encountered problems either in the growth of the wafers or in the processing of the devices, leaving them with insufficient gain for an external cavity laser.

The top-emitting design does not have enough lateral current spreading to support large aperture diameters. The output power is thus very limited in these devices. The top-emitting design is, however, estimated to be able to mode-lock in an external cavity with a saturable absorber with a very low, but realisable, saturation fluence.

The prospects of one of our bottom-emitting designs are good. It has an optical output power that is promising for use in an external-cavity mode-locked laser. The growth of the structure however went wrong and the structure has no net gain, which spoiled our chances to investigate it further in an external cavity.

Detailed descriptions of the structure designs, clean room processing procedures and characterisations of the designs are presented in this thesis. Furthermore, comprehensive simulations of carrier distributions in the quantum well sections and the gain saturation of the different designs are performed and discussed.

The thesis concludes with recommendations for further work towards the realisation of compact electrically pumped mode-locked vertical external-cavity surface emitting lasers.

Resumé

Denne afhandling omhandler designet af elektrisk pumpede vertikal-kavitets optiske forstærkere (eVCA) til brug i vertikale ekstern-kavitets pulsede lasere.

Fire forskellige eVCA'ere, en top-emitterende og tre bund-emitterende, er blevet designet og produceret, af hvilke kun den top-emitterende er blevet testet i en ekstern-kavitets laser. De andre design har haft problemer i enten dyrkningen af strukturerne eller i processeringen af eVCA'erne. Disse design har derfor ikke forstærkning nok til at kunne fungere i en ekstern-kavitets laser.

Den top-emitterende eVCA har ikke nok lateral strøm-spredning til store aperturer. Udgangseffekten af dette design er derfor begrænset. Den er dog estimeret til at kunne benyttes i en ekstern-kavitets pulset laser med en absorber med en lille, men realiserbar, mætbarhed.

En af de bund-emitterende design har en optisk udgangseffekt der er lovende for anvendelse i en ekstern-kavitets pulset laser. Desværre blev strukturen dyrket forkert og har ingen forstærkning, hvilket forhindrede os i at teste designet i en ekstern-kavitets pulset laser.

Afhandlingen inkluderer en detaljeret gennemgang af de forskellige design samt uddybende beskrivelser af processerings-procedurerne. Endvidere præsenteres modelleringer af designenes mætbare forstærkning og fordelingen af ladningsbærere i kvantebrøndene i de forskellige design.

Afhandlingen præsenterer afslutningsvis anbefalinger til videre arbejde med realiseringen af kompakte elektrisk pumpede vertikale ekstern-kavitets pulsede lasere.

Contents

Chapter 1

Introduction

1.1 Introduction

Semiconductor lasers gradually appear more and more often in our everyday lives; continuous-wave (CW) semiconductor lasers are used in e.g. laser-pointers, computer mice and reading and writing of DVDs and CDs. Furthermore, they have a promising application in pumping devices in optical circuits. Pulsed semiconductor lasers are used in re-clocking or pumping of devices in telecommunication systems, red-green-blue (RGB) displays, lasermarking and medical surgery.

This project aims for the creation of a compact electrically pumped pulsed vertical external-cavity surface emitting laser, i.e. an electrically pumped VECSEL or eVECSEL, this is a combination of the well-investigated worlds of vertical-cavity surface emitting lasers (VCSELs) *and* optically pumped pulsed VECSELs. The project focuses on the design and fabrication of the *gain section* of the electrically pumped VECSEL, which is called an electrically pumped vertical-cavity amplifier, abbreviated to eVCA.

1.2 Vertical External-Cavity Surface Emitting Lasers (VECSELs)

Most of the lasers we meet in our everyday lives are semiconductor edge-emitting lasers (in-plane lasers); the lasers are built as a sandwich structure in which current is injected perpendicularly to the structure. The active layers, most commonly *quantum wells* (QWs), are located in the middle of the structure and are embedded in layers that confine the injected carriers to the active layer. The light propagates in plane with the quantum wells and thus experiences gain in the whole length of the device. The lasers

can be cut from wafers in any size needed, and the cuts define the mirrors of the cavity. The wafers for such lasers can be grown by molecular beam epitaxy (MBE) or metal-organic chemical vapor deposition or vapour phase epitaxy (MOCVD/MOVPE). The main disadvantage of the edge-emitting lasers is that the output beam is roughly confined to the quantum-wells and thus has a highly divergent shape and is therefore difficult to couple into a fibre. The edge-emitting lasers have been produced since the sixties and many structures have been investigated in the following years.

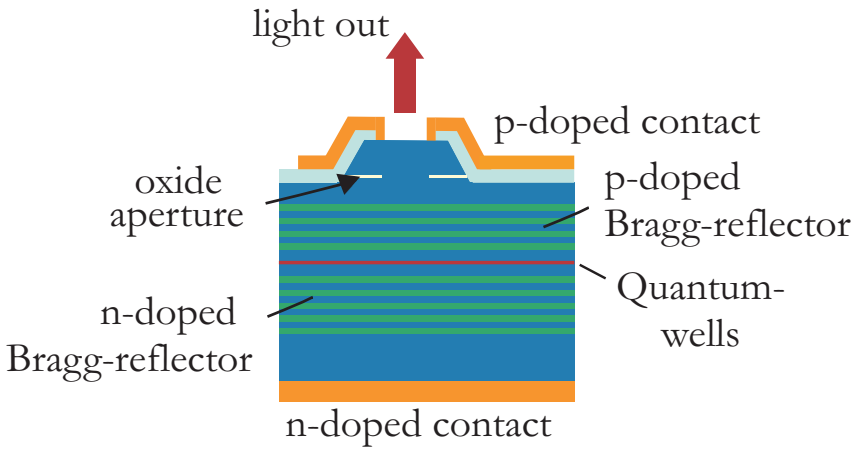

Figure 1.1: A vertical-cavity surface emitting laser (VCSEL). Light is emitted through the top surface of the device.

The semiconductor vertical-cavity surface emitting lasers (VCSELs) saw the light of day in the late seventies [1]. The light from a VCSEL propagates perpendicular to the gain-section, i.e. the quantum wells, and is emitted through the top surface of the wafer. As the light experiences a smaller net gain per pass compared to the edge-emitting laser, highly reflective mirrors are needed. These mirrors consist of alternating layers of high and low refractive index materials and can be grown into the structure as illustrated in 1.1. As the mirrors normally are much deeper than the active region they are called *distributed* Bragg reflectors (DBRs). A VCSEL has great advantages over the edge-emitting lasers as they provide circular, near-diffraction-limited output beams that are easily coupled into an optical fibre or focused to small spots. Furthermore, the power output is more or less scalable with the size of the aperture [2]. The built-in DBRs mean that the lasers can be tested on the wafer, i.e. no cleaving is needed, and *arrays* of lasers can be processed simultaneously.

A disadvantage of the VCSEL is the difficulty in making a high-power (i.e. large-aperture) *single-mode* VCSEL due to nonuniformities of the carrier density and/or refractive index across the aperture. One solution is to create buried anti-guiding VCSELs (i.e. where the transversal variation of the refractive index is lower in the core of the VCSEL than the cladding of the VCSEL) which have an enhanced mode selection [3]. Another recently developed technique is mode selection by printed structures in the surface of the aperture of the laser [4–7], or etched micro lenses into the surface of the VCSEL [8, 9]. This can increase the single-mode output power from around 3 mW [10] to around 7 mW [4].

A different way to control the mode of the laser is by forming an external-cavity laser; figure 1.2 is an example of an external-cavity laser formed by a gain section, i.e. a VCSEL without a top-mirror, to the left, optically connected to a highly reflective ($90-98\%$) curved mirror, to the right, that also works as an output coupler. The gain section, which contains a number of quantum wells and a $\simeq 100$ % reflecting DBR, can be grown by MBE or MOVPE. Due to higher diffraction losses of the higher order transversal laser modes (the higher order transversal modes expand faster than the fundamental mode), a properly designed VECSEL will lase in the fundamental mode. The first high-power optically pumped continous-wave VECSEL was presented by Kuznetsov et al. in 1997 and consisted of a gain section and a curved mirror as in figure 1.2. The external-cavity laser had a maximum output power of 0.5 W in first order mode when pumped at around 1.5 W [11].

The gain section of the lasers can be pumped optically or electrically (by injecting current, as in a VCSEL). The electrically pumped gain section is built as a *pin*-diode. The active layers, the quantum wells, are positioned in the *i*-section, i.e. the undoped region of the diode. The carriers are injected from each side of the diode and meet in the quantum wells in the undoped region, emitting light at the designed wavelength. The gain section can be equipped with a thin DBR on top in order to increase the total gain of the structure.

1.3 Mode-locked Lasers

In mode-locked lasers, either an external or internal modulation locks the longitudinal modes of the laser in phase, and the light is emitted in pulses. Active mode-locking uses an externally controlled modulator to modulate either the cavity loss or the gain. A passively mode-locked laser has no modulator but modulates the intra-cavity intensity by e.g. a saturable ab-

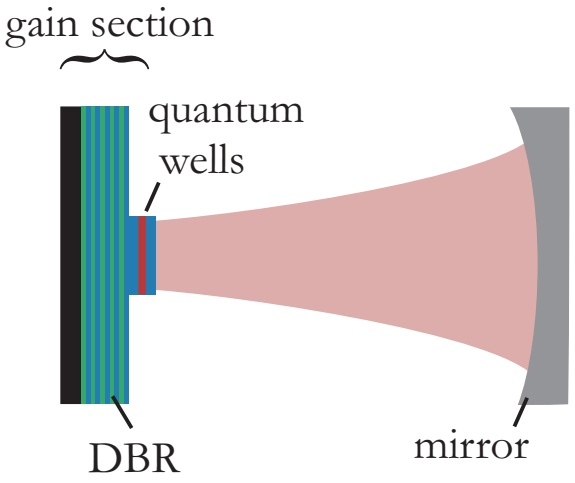

Figure 1.2: A vertical-external cavity surface emitting laser (VECSEL) formed by a gain section (to the left) and an external curved mirror.

sorber.

The history of mode-locking goes back to 1963 [12] when K. Gürs and R. Müller published an article titled "Breitband-Modulation durch Steuerung der Emission eines optischen Masers (Auskopple-Modulation)". This article describes the first indication of what is later known as *mode-locking* of ruby lasers. Many groups followed with active mode-locking of e.g. He-Ne lasers [13], and passive mode-locking in 1965 with a saturable dye normally used in Q-switched ruby lasers [14]. In 1972, Ippen et al. achieved passive mode-locking of an optically pumped dye laser using a dye molecule (DODCI) dissolved in methanol as a saturable absorber; the solvent had a very long recovery lifetime (several hundred ps), and it was not clear for the authors how they could obtain 1.5 ps pulses with this absorber [15]. Later, it has been shown that also the gain recovery time and the group delay dispersion of the devices in the laser cavity influence the pulse widths [16, 17].

The first semiconductor diode laser was actively mode-locked by Ho et al. in 1978; the group formed a VECSEL as illustrated in figure 1.2 with an $AlGaAs$ continous wave laser diode and a curved mirror and modulated the current injection of the diode at a frequency corresponding to the round-trip time in the cavity (3 GHz) [18]. The group obtained pulses of around 20 ps. In 1980, Ippen et al. obtained $\simeq 5$ ps pulses with an average power of 5 mW and a repetition rate of 850 MHz by mode-locking a semiconductor strip buried heterostructure diode in an external cavity [19]. The strip

buried structure had crystal defects that acted as an absorbing medium, the absorber and gain section was thus an *integrated* device. However, it had poor possibilities for adjusting the absorbing effects as the defects were in-grown *randomly* in the gain section.

Hoogland et al. presented the first VECSEL mode-locked by a semiconductor saturable absorber in 2000 (22 ps, 22 mW average output power at $> 4\ GHz$) [20]. The gain section was optically pumped, and since then, several groups have obtained excellent results with optically pumped mode-locked external-cavity lasers [21–24]. In 2005, the optically pumped VECSELs with semiconductor saturable absorbers had reached a repetition rate of 10 GHz, an average power of 1.4 W, and pulse durations of 6.1 ps. This particular laser was fed optically by a 17 W 808 nm CW-laser [25].

In the challenge of scaling down the size of the pulsed laser, it seems advantageous to avoid the pumping laser by electrically pumping the gain section. In 1993, Jiang et al. presented the first electrically pumped mode-locked VECSEL; The gain section consisted of a $1\mu m$ thick $GaAs$ active layer grown on a $AlAs/AlGaAs$ DBR. The gain section was positioned on a -172 °C cold finger and driven by a pulsed current less than 100 kHz in order to avoid heating. Active mode-locking was achieved by adding an RF signal, and pulse durations of $81 - 122\ ps$ were recorded [26].

Recently, a group from Brown University, Novalux Inc. and MIT Cambridge published their experimental results with mode-locked eVECSELs. Their first electrically pumped laser from 2003 was a Z-formed cavity with two concave mirrors, a gain section from Novalux Inc. and an absorber section similar to the structures developed by Keller et al. [27]. This laser performed 57 ps pulses at a wavelength of 980 nm with 1 W peak power (40 mW average) with a repetition rate of 1.1 GHz [24,28]. A linear cavity formed by a gain section optically connected to an absorbing section via a micro lens is more compact than the Z-formed cavity and offers much higher repetition rates. In 2004, the group presented a linear cavity formed by the same devices as above and with output-coupling through a double antireflection-coated beam splitter inside the external cavity. Pulse widths of 15 ps at a wavelength of 980 nm and a repetition rate of 15 GHz were obtained [29]. Unfortunately, the output power was not mentioned.

Of other pulse sources in the 1 μm spectral range there are diode pumped mode-locked *solid state lasers* with $Nd:YVO_4$, $Nd:YAG$ and $Nd:GdVO_4$ crystals as gain media. A $Nd:YVO_4$ solid state laser has been passively modelocked at 1064 nm with a repetition rate of $\sim 30\ GHz$ with pulses of $\sim 7\ ps$ and a maximum average output power of 80 mW [30]. Much higher average output powers of 2.1 W can be reached at a repeti-

tion rate of $\sim$ 10 GHz [31]. A $Nd : GdVO_4$ solid state laser has been mode-locked at 1063 nm with a repetition rate of $\sim$ 10 GHz with pulses of $\sim$ 12 ps and a maximum average output power of 500 mW [32]. Recently, $Nd : YAG$ have been mode-locked at 1064 nm at 130 MHz with 8.3 ps pulses and an output power of 1.59 W [33]. All the diode-pumped solid-state lasers mentioned here are passively mode-locked with semiconductor saturable absorbers (SESAMs), described in [27]. The diode-pumped solid state lasers are known as compact, reliable, efficient and thermally stable pulsed laser sources. However, sub-picosesond pulses are harder to obtain with passive mode-locked solid state lasers since their large gain saturation fluence leads to increased Q-switching instabilities at high repetition rates [34, 35].

One advantage of the semiconductor lasers is the future prospect of integration of the gain and absorber media, thus making compact, monolithic mode-locked lasers with very high repetition rates.

Monolithic $InGaAsP$ *edge-emitting* devices can offer very high repetition rates due to their short cavity length. Mode-locked edge-emitting devices can have repetition rates larger than 200 GHz [36], and even higher repetition rates (up to THz) can be obtained by harmonic mode-locking [35,37]. The high repetition rates do, however, come at the expense of a lower output power. A monolithic edge-emitting laser at 40 GHz gives $\sim$ 7 mW average power in 2.8 ps pulses at 1530 nm [38], i.e. at lower repetition rates the monolithic edge-emitters can not compete with the solid state lasers when it comes to the output power.

Many groups have contributed with theoretical analysis of pulse shaping in passively mode-locked lasers with saturable absorbers [12, 17, 39, 40]. Lately, Mulet et al. presented a time-domain description of an electrically driven passively mode-locked VECSEL similar to that of Jasim et al. [41]. The model showed stable mode-locking with pulses of around 10 ps at a repetition-rate of 15 GHz in accordance with the experimental results of [29]. Furthermore, the simulations gave some qualified suggestions to improve the pulse-width of the generated pulses.

1.4 Perspectives and applications of compact CW and pulsed VECSELs

Red-green-blue (RGB) laser sources have recently been used in displays and projectors [42–44]. The monochromatic laser light gives brilliant saturated colours. Also, the large depth of focus of the laser sources gives a sharp image even on curved surfaces. The RGB laser sources are based on

multiple second-harmonic generation (SHG) in LiB_3O_5 (LBO) crystals. To our knowledge, the first produced laser projector was presented by Moulton *et al.* [42], who uses a Nd:YLF 50 W (average) Q-switched pump laser at 1047 nm which by use of three LBO crystals ends up in three laser outputs at 628 nm, 524 nm and 449 nm with output powers of 1.42 W, 1.33 W and 0.85 W respectively. The system is built into a liquid-crystal display (LCD) projector. Brunner *et al.* [43] optimised the projector by using a passively mode-locked Yb:YAG disk laser with an average output power of 80 W and produces 8 W in red, 23 W in green and 10.1 W in blue.

For small displays such as in portable projectors, an replacement of the bulky Nd:YLF or Yb:YAG lasers with compact eVECSELs may be an advantageous step forward. Edge-emitting lasers are difficult to focus to a tight spot on the crystals, why VECSELs are most promising lasers in this field. However, the output power of the LBO crystals are proportional with the input power squared, the output power of such a device would therefore derease dramatically; assuming an output power of 100 mW of the eVECSEL, the RGB output would be in the order of 0.01 mW per colour.

However, intracavity frequency doubling increases the power onto the nonlinear crystal; Novalux has fabricated an electrically pumped CW NECSEL (Novalux external-cavity surface-emitting laser) with an intracavity non-linear crystal and obtained 2 mW output power at 488 nm and 5 mW at 462 and 532 nm [45]. The output power was increased to $\sim$ 34 mW when the NECSEL was pulse driven [46]. One of Novalux' standard electrically pumped CW NECSELs provides an output power of 500 mW at 980 nm [47].

The compactness of the electrical pumped VECSEL also suggests use in surgery, where lasers are more and more used. The most common lasers are the CO_2 laser with wavelength of $\sim$ 9.6 μm, Nd:YAG lasers with wavelengths of $\sim$ 1064 nm, argon lasers with wavelength of 458-515 nm, dye lasers of 585 nm [48] or diode lasers with wavelength of 810 or 904 nm [49]. Many of the lasers used in surgery have very long pulses and small repetition rates, i.e. they are either Q-switched or pulse driven.

Haemoglobin has an absorption peak at 585 nm [48]. Lasers of this wavelength are used for removing of damaged vessels in the outer skin or improving scars in the skin. Michel *et al.* describes experiments performed with a pulsed dye laser with a beam width of 5 mm, the fluence from $2-4$ J/cm^2 at a pulse duration of 250 μs. This is obtainable in a external laser cavity with a repetition rate in the kHz regime with an average output power of 100 mW.

Lasers of infrared wavelengths causes tissue heating, and these lasers are most often used for surgery instead of a scalpel. In some cases, the lasers are pulsed in order to control the thermal heating [49].

Another feature of the infrared pulsed laser is photo-acoustic imaging of blood vessels. using an Nd:YAG laser, described by Siphanto *et al.*. The laser emitted light at 1064 nm in 14 ns pulses with a repetition rate of 50 Hz. The energy density used in all experiments was below 50 mJ/cm^2 [50].

Another field that recently have gained from compact high-power lasers is laser marking, which is used as printing signs or textures into products. Laser marking with a Ti:Sa laser with an average output power of 0.1 W mode-locked at 1 kHz has been showed to reduce corrosion on implants to human bodies or tools used for surgery [51].

Use of optical devices in telecommunication systems reduce the switching energy and furthermore reduce the size of the system devices [52]. When optical devices are used in interconnects, the bandwidth will increase and the inter-connect delay will be reduced [53]. The efficient coupling between VECSELs and fibers makes the use of VECSEL in all-optical devices obvious. All-optical fiber signal processing devices such as Kerr fiber modulators (KFMs) uses co-propagating light sources with very small average powers in the mW range [54]. As the devices are used in telecommunication, wavelengths of 1540-1560 nm are required.

The main obstacle for use of the eVECSEL in the fields above is the low output power. With the output powers obtained by Jasim *et al.* [28,29] the eVECSELs will only be useful in laser marking and telecommunication optical switching and interconnecting. The rest of the applications need higher output powers.

The main advantages of the eVECSELs compared with the optical pumped VECSELs are the compactness and the thus easy integration into many systems and devices. Also, the development of an eVECSEL is a step forward to the monolithic mode-locked eVECSEL.

1.5 This thesis

This thesis presents the design and fabrication of an electrically pumped vertical-cavity amplifier (eVCA) to use in an vertical external-cavity mode-locked laser. Chapter 2 gives an introduction to the concept of mode-locking and the requirements to the eVCA and the absorber section in the laser cavity. The design of each layer in the eVCA is discussed in detail in chapter 3. This section also contains results from simulations of the carrier distribution in the different types of quantum well sections of the eVCAs,

which are performed in the program *SILVACO*, and simulations of the gain saturation of different structures of eVCAs, which are performed in MATLAB. The four eVCA-designs of this thesis are introduced in chapter 4 which also describes the clean room processing of the designs. Chapter 5 presents the characterisation of the eVCAs and finally chapter 6 discusses the results of this thesis and suggests future work in this field. Appendixes A, B and C illuminate the calculation of strain and gain in quantum wells, the calculation of gain saturation in the eVCAs and the simulations performed in *SILVACO*. Finally, appendix D presents the growth recipes of the designed eVCAs, and a table of symbols and abbreviations in this thesis is found in appendix E.

Chapter 2

Concept and design of mode-locked lasers

2.1 Concept of mode-locking

In a longitudinal multimode CW laser, the individual phases of the cavity modes fluctuate randomly leading to an almost constant output intensity. If, however, the longitudinal laser modes are locked in phase, as is the case in a mode-locked laser, the output intensity is concentrated in pulses. The more modes that are locked, the shorter the pulses.

A laser cavity with a longitudinal mode frequency ω_1 modulated at a frequency $\Delta\omega$ will generate sidebands at $\omega_1+\Delta\omega$ and $\omega_1-\Delta\omega$ in phase with the modulation signal. If we let the modulated signal $\Delta\omega$ be equal to the mode spacing of the cavity modes, the sidebands will be generated on top of the cavity modes. If the modulation is strong enough, the longitudinal cavity modes are thus forced to be *locked in phase*.

The intensity, $I(t)$, of N equidistant longitudinal modes with mode frequency spacing ω_n, amplitudes A_n and phase φ_n is equal to [55]

$$I(t) = |\sum_{n=0}^{N-1} A_n e^{j(n\omega_n t+\varphi_n)}|^2 \tag{2.1}$$

The intensities of 6 longitudinal modes is illustrated in figure 2.1; here, the intensities are calculated for 6 modes of the same amplitude, not in phase (**a**), 6 modes, not with same amplitude, all in phase (**b**), 6 modes of same amplitude, all in phase (**c**) and 6 modes of Gaussian distributed amplitudes, all in phase (**d**).

The amplitudes of the side bands play an important role; if the amplitudes fluctuate, sub-pulses will dominate the background intensity in an

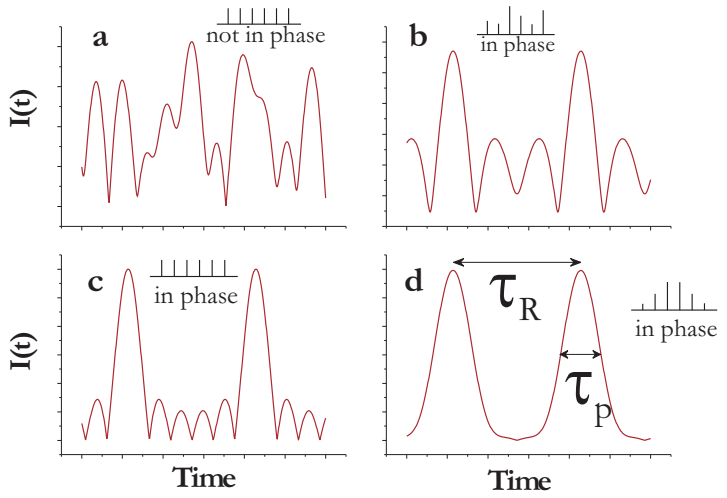

Figure 2.1: The beating of modes illustrated in the time-regime where six modes are **a:** of same amplitude, not in phase **b:** not same amplitude, in phase **c:** of same amplitude, in phase **d:** of Gaussian amplitude, in phase. τ_R is the round-trip time of the laser and τ_p the FWHM pulse width of the pulses. Inspired by [55]

irregular way as illustrated in figure 2.1**b**. Therefore, in order to obtain nice pulses, side-modes of constant amplitudes should be generated (figure 2.1**c**) or controlled to have a Gaussian envelope (figure 2.1**d**).

The Gaussian-shaped pulse of figure 2.1 **d** has a full-width half maximum (FWHM) pulse-width equal to

$$\tau_p = \frac{0.44}{N\Delta\omega} \tag{2.2}$$

where N is the number of locked modes and $\Delta\omega$ is the mode spacing. The factor 0.441 is the time-bandwidth product for Gaussian pulses [56]. The mode spacing is equal to

$$\Delta\omega = \frac{2\pi}{\tau_R} \tag{2.3}$$

τ_R being the round-trip time of the cavity.

2.1.1 Passive mode-locking with a saturable absorber

Semiconductor saturable absorbers can either be an inverse-biased device, where the recovery time is determined by the sweep-out of the carriers by the electrical field *or* a passive (non-biased) device, where the recovery time is determined by the thermalisation and recombination times of the carriers.

When a pulse of light with sufficient photon energy hits a semiconductor saturable absorber, carriers are excited from the valence band to the conduction band. If the pulse energy is high enough, the upward transition will saturate due to depletion of carriers in the valence band or full occupied states in the conduction band. The carriers will re-organise via intraband carrier-carrier scattering to a quasi-Fermi distribution, i.e. local equilibrium distributions of the electrons and the holes in the conduction band and valence band respectively. This occurs on a *femtosecond* timescale. Subsequently, the carriers thermalise to the lattice temperature via carrier-phonon scattering, and this occurs on a timescale of *picoseconds* to *nanoseconds*. Finally, all carriers re-organise to a global Fermi-distribution via recombinations, possibly via deep-level states. After this re-organisation, the absorber has recovered and full absorption is re-established.

In a simple model, the saturable absorber has a non-linear intensity absorption of

$$A(t) = \frac{A_0}{1 + F_p(t)/F_{sat}} \tag{2.4}$$

where A_0 is the unsaturated intensity absorption, $F_p(t)$ is the fluence of the pulse of light and F_{sat} is the saturation fluence of the absorber, both measured in units of energy per unit area. The saturation fluence is here defined as the pulse fluence where the intensity absorption has decreased to $A_0/2$. The saturable absorber has a pulse-shortening effect as long as the pulse in the cavity is intense enough to saturate the absorber. As the pulse travels through the absorber, only the leading edge will be absorbed thus reducing the width of the pulse.

The absorbing material is most often incorporated into a structure, e.g. epitaxially grown *on* or *into* a DBR. The structure can be inserted as an end mirror in the laser cavity as illustrated in figure 2.2. The fluence of the incoming light is thus easily controlled by the spot size on the saturable absorber.

Figure 2.3 shows the temporal evolution of the gain in the gain section and the absorption in the absorber section in a mode-locked laser in a coordinate system that follows the pulses. The moment the pulse enters

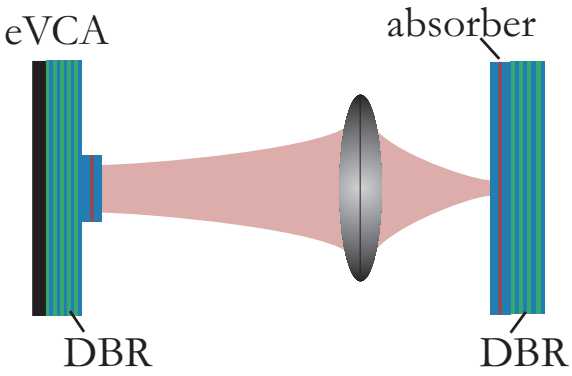

Figure 2.2: An example of a passive mode-locked laser; the gain section, an eVCA, to the left and a saturable absorber on a Bragg-mirror to the right.

the absorber, there is net absorption in the cavity, and the leading edge of the pulse will thus be attenuated. The pulse saturates the absorber and a window of net gain opens up a passage to the pulse. Gain in semiconductors is achieved by population inversion which can be depleted by a strong pulse, much like the absorption discussed above, effectively saturating the gain. The saturation of the gain closes the window of net gain. This means, that the absorber must saturate more than the gain in order to open a window of net gain to the pulse. Furthermore, a fast recovery of the absorber or a saturation of the gain closes the window of net gain.

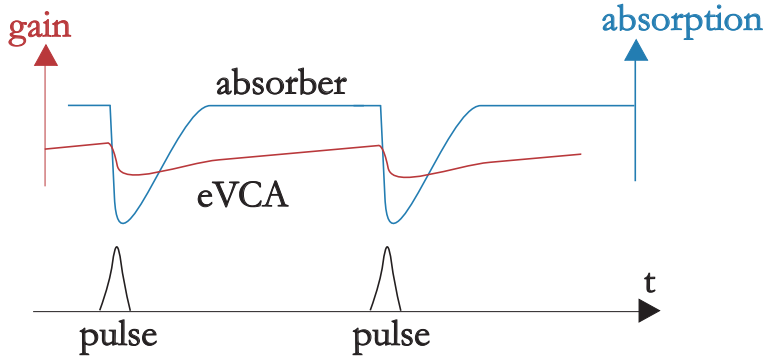

Figure 2.3: The absorption and the gain of the absorber and the eVCA in the time-domain. The saturation of the absorber leads to a window of net gain.

Besides the dynamics indicated in the gain and absorber curves of figure 2.3, an interplay between a positive group delay dispersion and the non-

linear phase change of the gain and absorber sections can lead to quasi-soliton pulses much shorter than the window of net gain [17].

When a pulse is reflected on a section with a nonlinear gain, the electromagnetic field experiences a phase change, ϕ, proportional to the linewidth enhancement factor, α_H, and the change in the gain of the section during the reflection of the pulse, i.e.

$$\frac{\delta\phi}{\delta t} = -\frac{1}{2}\alpha_H \frac{\delta G}{\delta t} \tag{2.5}$$

A time-dependent phase change corresponds to a spectral broadening of the pulse.

Furthermore, the group delay dispersion of a section leads to a wavelength dependent phase change proportional to the product of the group delay dispersion of the section and the square of the spectral bandwidth of the pulse [57].

These two phase changes are opposite in sign and can thus compensate each other. The compensation requires a positive group delay dispersion of the sections in the mode-locked laser cavity. Paschotta et al. [57] has simulated the pulse duration of quasi-soliton pulses in an external cavity mode-locked laser with a gain section and an absorber section. Since the phase change of the pulse field due to the nonlinear gain and the nonlinear absorption depends on α_H, this phase change depends strongly on the carrier density in the amplifying and absorbing layers [57]. Also, the time-dependent gain (and absorption) $g(t)$ (and $a(t)$) depends on the intra-cavity pulse energy and also the fluence (energy per area) on the gain and absorber structures. In order to obtain quasi-soliton mode-locking, the saturable absorption and saturation energies of the absorber must thus be optimised together with the intracavity pulse energy, the gain saturation energy and the total cavity dispersion [57]. This optimisation is a complicated matter that requires numerical analysis. Paschotta et al. finds a stable quasi-soliton mode-locking in a external cavity with a positive round trip group delay dispersion $> 3000\ fs^2$. Soliton mode-locking with pulse durations of $< 500\ fs$ has experimentally been observed in VECSELs with an optically pumped semiconductor gain section with a group delay dispersion of $< 900\ fs^2$ [23].

The saturation of the absorber section depends on the type of structure the absorbing material is grown *on* or *into*. Many groups have fabricated semiconductor saturable absorber structures, and they have been given many names; saturable Bragg Reflectors (SBRs) [58], Semiconducting Saturable Absorber Mirrors (SESAMs) [27], Saturable Absorber Mirror (SAMs) [59]. The top part of Figure 2.4 shows an example of an absorber

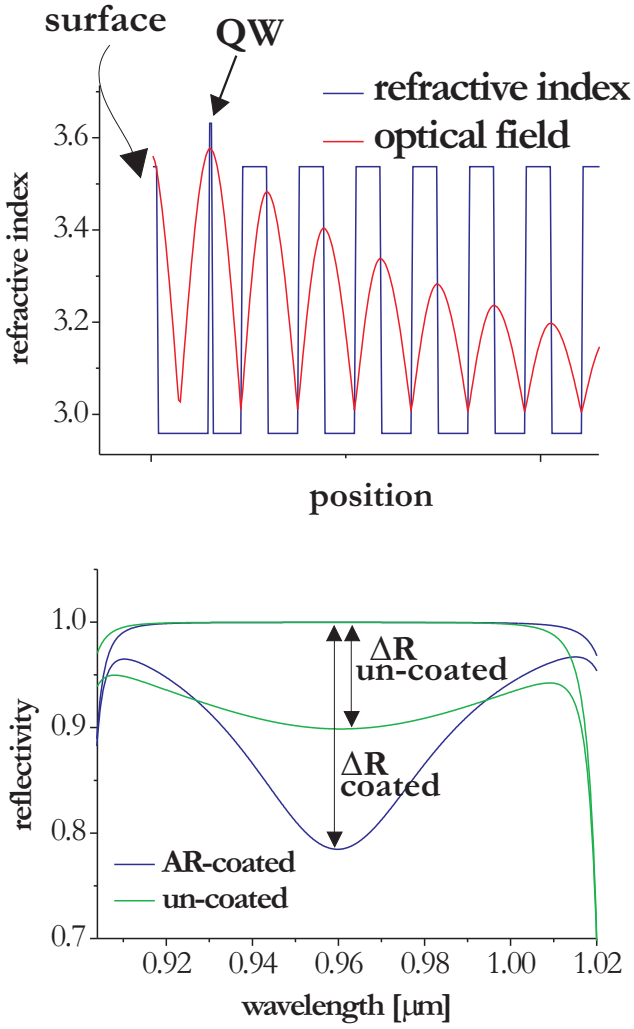

Figure 2.4: An example of an absorber structure; The top graph illustrates the refractive index (blue) of absorber structure and the optical field (red) in the structure. A single 8-nm $In_{0.17}Ga_{0.83}As$ quantum well (arrow) is positioned in an antinode of the optical field. The calculated reflectivity of this structure is shown in the bottom graph. The reflectivity of the un-coated absorber is represented by the green line and the reflectivity of the AR-coated absorber by the blue line. For both structures, the reflectivity is calculated without absorption in the quantum wells and with an absorption coefficient of 2000 cm^{-1} in the quantum wells. ΔR is the difference of the reflectivity with and without absorption.

structure designed to a wavelength of 960 nm. It consists of a 28-period $GaAs/AlAs$ DBR (only 6 periods are visible on the figure) and a single 8-nm $In_{0.17}Ga_{0.83}As$ quantum well (marked with arrow) positioned in an antinode of the optical field close to the surface of the structure. The reflectivity of this particular structure and the optical field inside this structure has been calculated in MATLAB by a transfer-matrix method [60]. The calculated reflectivity of this structure is shown in the bottom graph. The reflectivity of the un-coated absorber is represented by the green line and the reflectivity of the AR-coated absorber by the blue line. For both structures, the reflectivity is calculated without absorption in the quantum wells and with an absorption coefficient of 2000 cm^{-1} in the quantum wells. The modulation depth, ΔR, is defined as the variation in reflectivity for a saturated absorber structure (i.e. at large pulse fluences) and a non-saturated absorber structure (i.e. at small pulse fluences). At 960 nm, $\Delta R \simeq 10\%$ for the un-coated and $\Delta R \simeq 20\%$ for the AR-coated absorber. No wavelength-dependent absorption in the quantum well is included. The reflectivity of the saturated absorber structure, R_{ns}, is not equal to 100 % due to the non-saturable loss in the absorber structure. This loss originates in transmission losses in the DBR, free-carrier absorption and defect recombinations, and these losses should be minimised. In case of figure 2.4, the reflectivity of the saturated absorber is equal to 99.98 %.

At high pulse fluences, the modulation depth of the absorber might roll over. At short pulse durations, this roll over can be explained by two-photon absorption (TPA), however at larger pulse durations, this roll over might also be caused by other types of absorptions such as free-carrier absorption, Auger-recombination and lattice heating [61]. The reflectivity of an absorber structure averaged over a pulse with fluence F_p can in a simple absorber model where the absorber recovery time is assumed longer than the pulse durations be expressed by [62]

$$R_{abs}(F_p) = R_{ns}\frac{ln(1+\frac{R_{ns}-\Delta R}{R_{ns}}(e^{F_p/F_{sat}}-1))}{F_p/F_{sat}}(e^{-F_p/F_2}) \tag{2.6}$$

F_2 is the roll over parameter, expressed in units of mJ/cm^2. F_2 is equal to [62]

$$F_2 \simeq \frac{\tau_p}{\beta_{TPA} z_{eff}} \tag{2.7}$$

where β_{TPA} is the two photon absorption coefficient expressed in units of cm/MW, τ_p is the pulse duration and z_{eff} is the effective absorber thickness, which includes the penetration depth of the optical field into the

DBR. The saturation fluence of an absorber can be adjusted by changing the position of the absorbing layer (quantum well) relative to the optical field or by changing the structure of the device.

Figure 2.5 shows the calculated reflectivity of an absorber structure, R_{abs}, with a roll over parameter, F_2, of 500 mJ/cm^2, 50 mJ/cm^2 and without roll over. The calculations are based on equation 2.6, and in all three plots, ΔR is set to 0.8 %, F_{sat} is set to 40 $\mu J/cm^2$ and R_{ns} to 99.8 %. The modulation is illustrated at two different pulse fluences; roll over leads to a smaller modulation variation at higher pulse fluences. If the roll over parameter is comparable with the saturation fluence, the roll over will eliminate the effect of saturation in the absorber [61]. The two-photon absorption depends on the material surrounding the quantum well in the absorber. As the two-photon absorption in $AlAs$ at $960 - 980$ nm is negligible [63], surrounding layers of $AlAs$ can with advantage be used in absorber structures instead of $GaAs$.

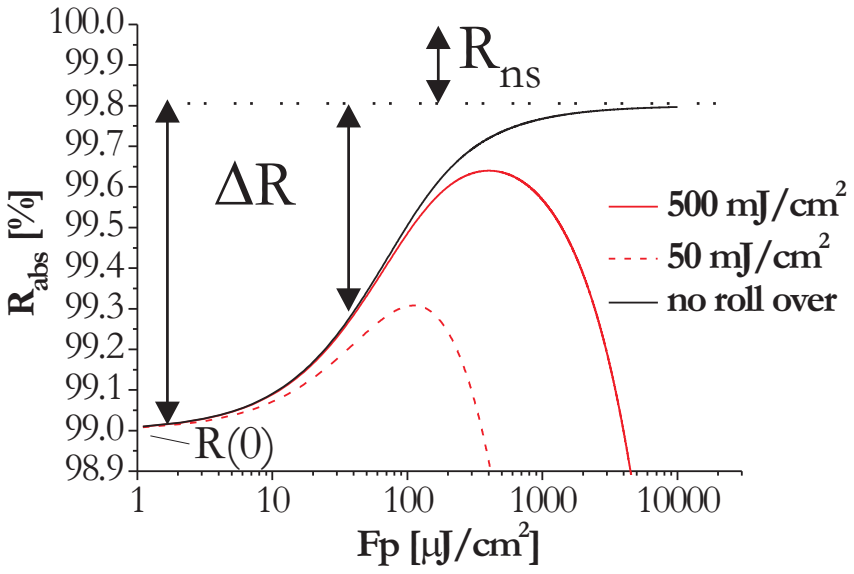

Figure 2.5: The non-linear reflectivity of an absorber without roll over (black curve) and with roll over parameters of 500 mJ/cm^2 (red curve) and 50 mJ/cm^2 (dashed red curve).

2.1.2 Absorber material

The recovery time of a passive saturable absorber is determined by the intra- and interband thermalisation times as mentioned earlier. An advantage of quantum well saturable absorbers over bulk saturable absorbers is a faster intraband thermalisation time due to a higher density of states near band edge. The interband thermalisation time can be controlled by creating trapping or recombination centers, which can be done in several ways. Semiconductor devices with deep-level recombination or trapping centers have been developed by many groups and several approaches have been presented; ion implantation or irradiation, proton bombardment, defect growth of quantum wells, use of surface recombination centers in quantum wells, and low-temperature (LT) grown quantum wells. A list of different types of absorbers and their properties found in literature is presented in table 2.1.

Ion implantating or irradiating or proton bombardement of semiconductor devices creates recombination and trapping centres, however, it also introduce a higher non-saturable loss and a smaller modulation depth. Rapid thermal annealing of the absorber structure has been found to reduce the non-saturable losses and improve the modulation depth while the short lifetime was preserved [64–66].

A different solution is to grow the absorber layer on a lattice-mismatched material, which automatically will lead to defects in the absorbing layer [67]. Alternatively, the absorber layer can be grown close to the surface of the device and in this way use the surface recombination traps to decrease the carrier life time. The non-saturable losses are estimated to be negligible in this kind of device [68].

Another approach to a reduced carrier lifetime is low-temperature MBE-growth; when a material containing As, e.g. $InGaAs$, is grown at low temperatures (350 °C or less), As will not enter the material correctly. The excess of As atoms leads to interstitial As, clusters of As in the material or Ga vacancies. These defects in the $InGaAs$ crystal leads to extra energy levels in the $InGaAs$ bandgap, that work as trapping and recombination centers, and the carrier lifetimes is thus reduced [71]. Since this behavior is connected to the excess of As-atoms, a similar reduction is expected in other materials containing As. LT-growth of absorber layers containing As is e.g. used in quantum well and quantum dot devices [69] and [70]. The non-saturable absorption of LT-grown $InGaAs/GaAs$ quantum wells increases as the growth-temperature decreases [72], so a thin absorber can be advantageous.

type	λ $[nm]$	ΔR [%]	R_{ns} [%]	F_{sat} $[\mu J/cm^2]$	τ_A $[ps]$	reference
ion-impl.	1060	0.7	$1 \rightarrow 0.5$	20	> 11	[64]
ion irradiated	1040	$14 \rightarrow 17.4$	$19.5 \rightarrow 11$	$4.5 \rightarrow 2.9$	$0.8 \rightarrow 1.1$	[65]
proton bomb.	1550	4	~ 2	< 172	1	[66]
$GaAs/CaF_2$	830	2.2	2.7	36	1.2	[67]
Surface QW	1550	0.5	negligible	~ 100	21-180	[68]
LT-grown QW	1314	0.6	0.04	11.2	-	[69]
LT-grown QW	1314	3.9	0.3	1.1	-	[69]
LT-grown QD	960	3.1	0.3	1.7	-	[70]

Table 2.1: Different types of saturable absorbers from literature. The parameters in the ion-implantated and ion-irradiated saturable absorber have been varied by annealing at different temperatures.

2.2 Choice of cavity

The choice of cavity determines the spot size on the saturable absorber and thus determines the pulse fluence on the absorber. The choice of cavity is thus connected to the aperture size of the gain section and the saturation fluence of the absorber.

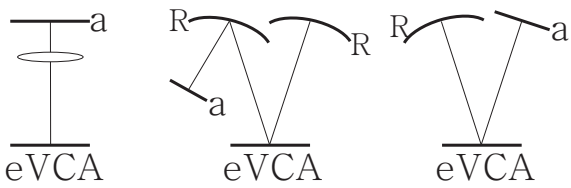

Figure 2.6: Three types of cavities; linear (left), Z-cavity (middle) and V-cavity (right). The reflectors and absorbers are tagged R and a, the gain sections are tagged eVCA.

The Z-cavity and V-cavity have some advantages over the linear cavity. Firstly, curved mirrors, denoted R in figure 2.6, can be designed with low transmission losses, whereas lenses normally have a transmission loss of ~ 0.6 %, even when AR-coated. Another important advantage of the Z- and V-cavities is that they allow double passing of the eVCA, thus leading to twice as much gain per round trip in the cavity.

The Z-cavity is most flexible as the spot sizes on the absorber and eVCA can be adjusted individually. The absorber spot size and repetition

rate in the more compact V-cavity and linear cavity are solely determined by the radius of curvature of the curved mirror or focal length of lens and cannot be tuned individually.

The linear cavity is the most compact cavity. Zhang *et al.* tested these particular cavities with an electrically pumped gain section and obtained a repetition rate of 6 GHz with the linear cavity compared to $3.5 - 4.0$ GHz with the V and Z cavity respectively [24].

The possibility of integrating the gain section and absorber in one monolithic device has not been pursued to date. Since the fluence on the absorber in such a device is not adjustable by changing the spot size on the absorber, the saturation fluence of the absorber should be tailored to fit the gain saturation, output power and area. The repetition rate in such a monolithic vertical-cavity mode-locked device would however be very large. At constant intra-cavity powers, the fluence on the absorber decreases as the repetition rate increases. Absorbers with small fluences, such as the quantum dot or low-temperature grown absorbers discussed in the previous section, thus seem promising for integrated mode-locked lasers [69, 70].

Alternatively, the integrated device can contain a micro lens that focuses the output beam of the gain section on the absorber. Some groups have integrated VCSELs or VECSELs and micro lenses, forming high power single mode lasers. The lenses are either formed by growing curved membrane-DBRs [9] or by growing the DBR on a $GaAs$ layer that is etched to have a lens shape [8, 73].

Chapter 3

Design of eVCA

3.1 Introduction

This section focuses on the design of the electrically pumped vertical-cavity amplifier, eVCA. An example of an eVCA is shown in figure 3.1, which displays the refractive index of the eVCA and the intensity of the optical field calculated in MATLAB by a transfer matrix method. The surface of the eVCA is located to the left. The active region consists of 2 sections of quantum wells, both positioned in the antinode of the optical field. Each section contains 3 quantum wells and the wells are separated by barriers, i.e. material with a larger energy gap than the wells. The two sections of quantum wells are separated by a spacer layer so that the quantum wells are positioned in the antinode of the optical field. The sections of quantum wells are embedded by cladding layers that confine the carriers to the quantum well sections. The quantum well sections are grown on top of a $GaAs/AlAs$ DBR, which is seen on the right side of the quantum wells.

Quantum wells are more efficient active materials than bulk materials since they have a larger density of states at the band edge which increases the differential gain and thus the quantum efficiency of the device. Furthermore, the energy levels in a quantum well are easily controlled by changing the thickness of the well or the material composition of the well or the barriers embedding the well.

In order to inject current into the eVCA, the structure is built as a *pin* diode where the quantum wells are positioned in the intrinsic region. The layers around the quantum well section is thus n and p doped. The epitaxial layers of the eVCA should be designed in a way that ensures a maximum of the optical intensity in the quantum wells and a minimum of the optical field intensity in the highly doped layers in order to reduce

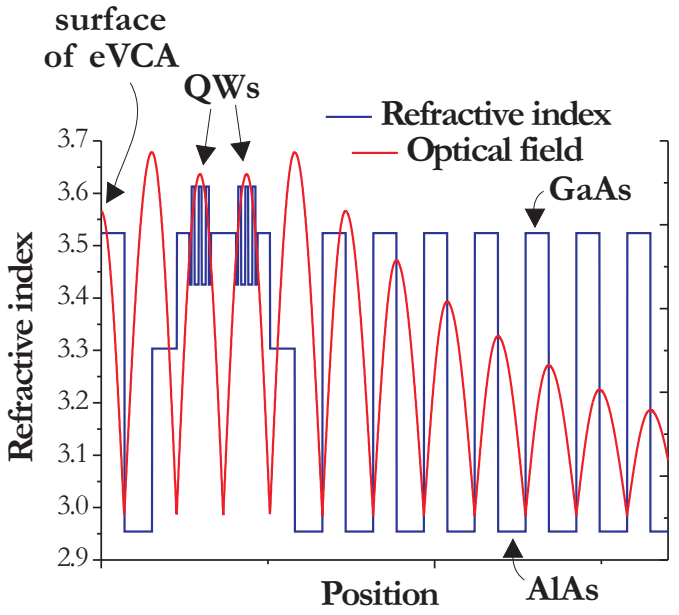

Figure 3.1: An example of an eVCA structure showing the refractive index (blue) of the structure and optical field (red) calculated by a transfer-matrix method. The active region consists of 2 sections of 3 quantum wells, each section positioned in the antinode of the optical field.

free-carrier absorption. Furthermore, the eVCA should be designed in a way that ensures a high carrier density in the quantum wells and also a homogeneous lateral carrier density across the aperture of the eVCA. In addition, the structure should have a low thermal resistance, a high gain saturation fluence *and* a large small-signal gain.

Section 3.2 presents the two types of eVCAs in this thesis; the top-emitting and the bottom-emitting type. The rest of the sections in this chapter illuminate the different regions of the eVCAs; the quantum well region in section 3.3, the choice of barrier and spacer material in section 3.4, the doping of the eVCA in section 3.5, the distributed Bragg-reflectors in section 3.6, the current-confining oxide layer in section 3.7, the current-spreading layers that laterally spreads the current in the eVCA in section 3.8, and the contacts on the eVCAs in 3.9. Section 3.10 discusses the group delay dispersion and full width at half maximum gain bandwidth of the eVCAs. Section 3.11 discusses the gain saturation power and the change of reflectivity of the eVCA during passage of a pulse. Finally, section 3.12

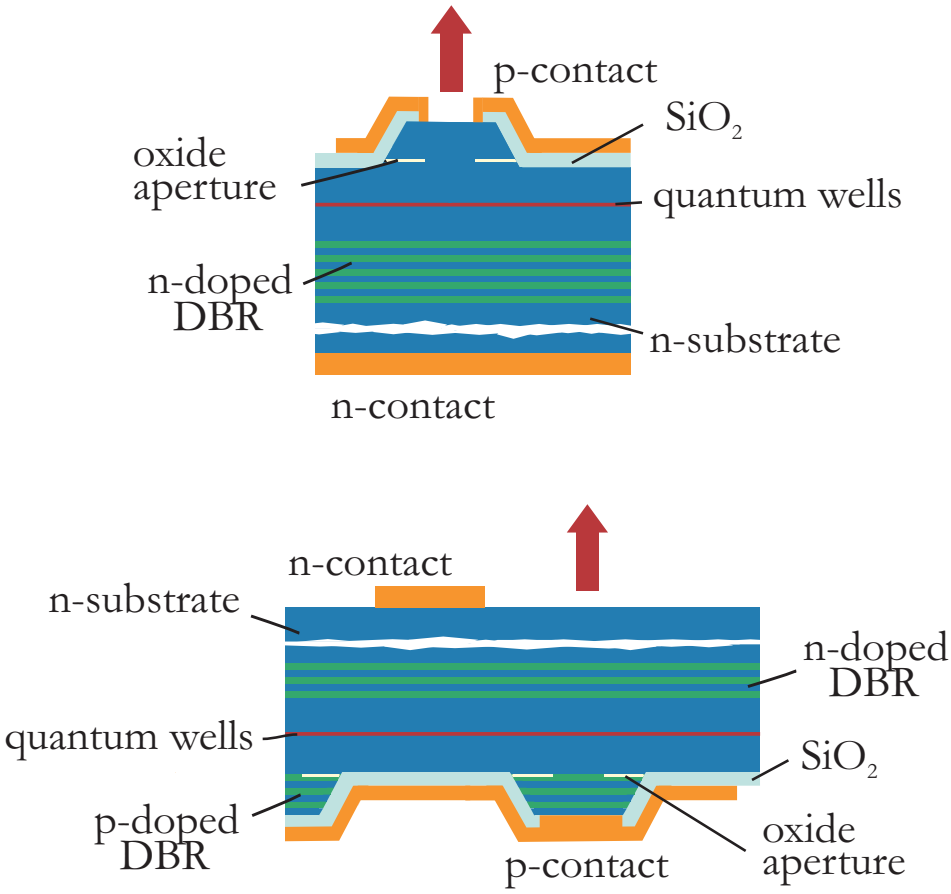

Figure 3.2: A top-emitting eVCA (top) and a bottom-emitting eVCA (bottom).

summarises the chapter.

3.2 Top- and bottom-emitting eVCA

Figure 3.2 shows two types of eVCAs; a top-emitting and a bottom-emitting. The layer thicknesses are not to scale.

The top-emitting structure consists of an n-doped DBR grown on the substrate (in this case n-doped). The intrinsic region containing the quantum wells is positioned on top of the DBR and is topped with a current-confining oxide layer (yellow line) and a highly p-doped *GaAs* cap layer. The current is applied through the substrate via the n-, and p-type con-

tacts. The p-type contact is ring-shaped in order to allow the light to emit through the top surface.

The bottom sketch illustrates a bottom-emitting structure. This structure is mounted up side down on the p-DBR and light is emitted through the substrate. The n-contact is in case of figure 3.2 positioned on the substrate, which can be lapped mechanically and chemically to a thickness of around 50 μm. However, contacting on the substrate requires a doped substrate which absorbs photons (free-carrier absorption). On the n-side of the quantum well section, one can choose to have a few layers of an n-doped "top" DBR in order to increase the net gain of the structure. Although an n-doped DBR increases the net gain, it will also decrease the gain saturation fluence and the full width at half maximum (FWHM) bandwidth of the gain. The reduction in the bandwidth leads to a strongly wavelength-dependent gain and introduces a group delay dispersion in the structure. The group delay dispersion and gain saturation is treated in section 3.10.

In order to reduce the free-carrier absorption in the substrate, *all* the substrate can be removed mechanically and chemically; in this case one would need to grow an etch-stop layer right next to the substrate. As the emitted light in this case will not be absorbed by travelling through the substrate, the structure requires a smaller top DBR in order to achieve the same gain.

The advantages of a bottom-emitting eVCA are many-fold; the quantum wells and the p-DBR where Joule-heating is generated, see section 3.6, are closer to a heat sink on which the sample can be mounted. Furthermore, as the mobility of the holes is lower than the mobility of electrons, it is more difficult to spread holes to achieve a uniform lateral hole-density across the aperture in a top-emitting structure. In a bottom-emitting eVCA, the p-doped contact covers the entire active area. This means that the lateral hole-density profile in the quantum well region is more uniform in large area bottom-emitting structures compared with top-emitting structures. In order to further enhance the overall lateral carrier uniformity in a bottom-emitting eVCA, current-spreading layers (see section 3.8) can be grown on the n-side of the quantum well section in order to spread the electrons from the n-contact to the active area of the device.

As the maximum output power of a top-emitting VCSEL is often limited by the lateral current spreading in the device, many groups have investigated the bottom-emitting VCSELs [74–77]. The bottom-emitting structures have far better lateral current spreading that allows much larger apertures than the top-emitting structures [75]. As the output power of the devices scales with the area of the device, bottom-emitting VCSELs

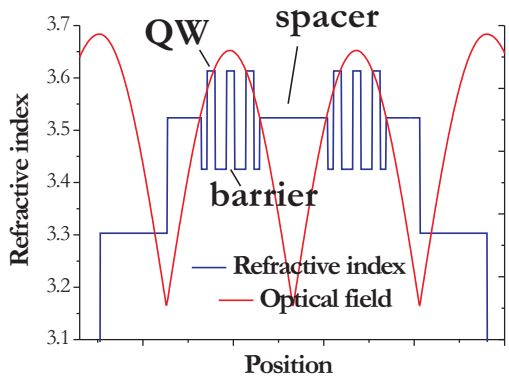

Figure 3.3: The refractive index (blue line) and the optical field (red line) of a quantum well region with two sections of 3 quantum wells. Each section is positioned in the antinode of the optical field.

are promising structures for high output power devices. Bottom-emitting VCSELs with an aperture diameter up to 570 μm and output power of 1.95 W have been produced [77].

Bottom-emitting structures are also used in optically pumped mode-locked VECSELs; The average output power is increased by one order of magnitude compared to VECSELs with top-emitting structures due to a far more efficient removal of the heat generated in the structure [22].

3.3 Quantum well region

In structures presented in this thesis, the quantum well section is an integer number of half wavelengths thick and consists of a number (typically 3-9) $In_{1-x}Ga_xAs$ quantum wells positioned in the antinode of the optical field, as illustrated in figure 3.3. The quantum wells are surrounded by barriers of either $Al_yGa_{1-y}As$ or $GaAs_yP_{1-y}$. The quantum wells and barriers are embedded in $Al_yGa_{1-y}As$ spacer layers with thicknesses to fulfil the $\lambda/2$-requirement for the standing waves.

The quantum well region is in most VCSELs and electrically pumped diodes left un-doped. The carrier-distribution and thus the gain in the region can, however, be enhanced by proper doping of the barriers or cladding layers, which will be discussed in section 3.4.1.

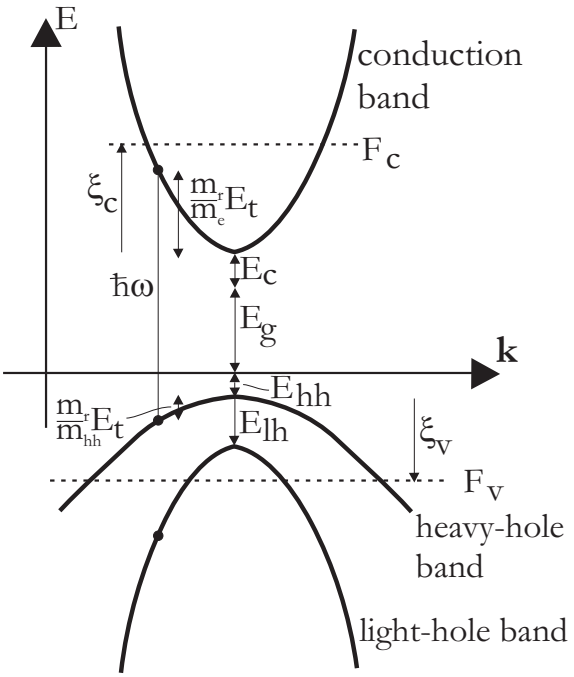

Figure 3.4: The conduction band, heavy-hole band and light-hole band of a (strained) quantum well. ξ_c and ξ_v are the separations from the quasi-Fermi levels, F_c and F_v to the conduction band and valence band edge respectively, and both separations are defined as positive when located in the conduction and valence band respectively.

3.3.1 Gain and absorption in quantum wells

The gain an optical field experiences in a quantum well of thickness d is equal to $e^{\Gamma g d}$, where Γ is the confinement factor which is proportional to the overlap between the standing optical field and the quantum well (see appendix B page 160) and g is the gain coefficient of the material in units of cm^{-1}. The gain coefficient of a quantum well is in this section calculated as a function of the separations, ξ_c and ξ_v, of the quasi-Fermi levels from the conduction band and valence band edges as illustrated and defined in figure 3.4. ξ_c and ξ_v are defined as positive when the electron and hole quasi-Fermi levels are located in the the conduction and valence bands respectively.

The figure 3.4 illustrates the energy bands of a strained quantum well where the heavy hole and light hole band is separated. Strain of materials is treated in section 3.3.3 and appendix A.

The gain coefficient for a photon of energy $\hbar\omega$ when it interacts with a

transition from the n^{th} electron sub-band to the m^{th} valence sub-band of a quantum well is expressed by [78]

$$g(\hbar\omega) = \sum_{n,m} C_0 |I_{hm}^{en}|^2 \rho_r^{2D} |\widehat{e} \cdot \overline{p}_{cv}|^2 \cdot [f_c(E_t = \hbar\omega - E_{hm}^{en}) - f_v(E_t = \hbar\omega - E_{hm}^{en})] H(\hbar\omega - E_{hm}^{en}) \quad (3.1)$$

The factor C_0 is among other things inversely proportional to the photon energy, $\hbar\omega$. $|I_{hm}^{en}|^2$ is the overlap integral of the conduction band and valence band envelope functions and is assumed here to be equal to 1 for transitions where $m = n$ and otherwise 0. ρ_r^{2D} is the joint density of states in the quantum well and

$$|\widehat{e} \cdot \overline{p}_{cv}|^2 = |\langle u_c | \hat{\mathbf{e}} \cdot \mathbf{p} | u_v \rangle|^2 \quad (3.2)$$

is the optical matrix element, where u_c and u_v are the wave-functions of the conduction band and valence band, respectively. The polarisation, $\hat{\mathbf{e}}$, of the interacting light and the momentum of the involved carriers, $\mathbf{p}$, thus play a role in the strength of interaction. The optical matrix element is different from conduction band to heavy hole or light hole transition, and the heavy hole and light hole contribution to the gain is thus polarisation dependent; the conduction band to heavy hole transition only interacts with light polarised in plane with the quantum well (TE mode). The conduction band to light hole transition interacts both with light polarised in plane and perpendicular to the quantum well (TM mode).

f_c and f_v are the Fermi-Dirac carrier distribution functions and $H(\hbar\omega - E_{hm}^{en})$ is a step function equal to one when the photon energy is equal to or larger than the band gap energy between the n^{th} electron sub-band and m^{th} valence sub-band and otherwise zero. Expressions of the optical matrix-element for heavy-hole and light-hole transitions as well as more detailed descriptions of all factors in equation 3.1 are presented in appendix A.

The calculated gain coefficient of the transverse electric (TE) and transverse magnetic (TM) polarised light in a 8-nm $In_{0.17}Ga_{0.83}As$ quantum well with $GaAs$ barriers is plotted in the top of figure 3.5. The conduction band to heavy hole transition of this well is located at ~ 980 nm, and the conduction band to light hole transition is located at ~ 900 nm. Both quasi-Fermi levels in this calculation are assumed to be located 0.2 eV into the conduction band and valence band, i.e. both ξ_c and ξ_v are equal to 0.2 eV. In the bottom graph of same figure, the maximum gain coefficient of the TE light in the conduction band to heavy hole transition (~ 980 nm) is plotted versus the separation of the electron quasi-Fermi level to the conduction

band, ξ_c, for two different values of ξ_v (0 eV and 0.2 eV). The maximum gain coefficient at these separation values is around 4300 cm^{-1}. The graph shows the importance of increasing *both* the conduction band separation and valence band separation to get a high gain coefficient.

A quantum well for use in a eVCA have a typical width of $6 - 10$ nm. A wide quantum well has sub-bands fairly close to each other and thus an increased probability of populating neighboring bands. A narrow quantum well has a ground-state level close to the cladding layer (or barrier) leading to a less confined state and also unwanted population of carriers in the cladding or barrier layers.

The optical transition of the quantum well is in this section calculated for a single carrier in the well. The optical transition is broadened due to a finite state lifetime. The gain in figure 3.5 is thus convoluted with a Gaussian linewidth with a full width half maximum of 100 fs [60]. Additional broadening of the optical transitions of the quantum wells is not considered here.

3.3.2 Many-body and temperature effects

The optical transition of the quantum well may be shifted by effects such as band gap shrinkage and exciton states. The shift in the band gap due to exciton states is an effect that disappears at high carrier densities (due to carrier screening of the Coulomb interaction) whereas the band gap shrinkage is dominating at high carrier densities.

Band gap shrinkage arises from increased nearest-neighbour overlap of carriers at high sheet carrier densities, n_{2D}. The band gap shrinkage of a quantum well has a $n_{2D}^{1/1.3}$-dependence at low carrier densities and a $n_{2D}^{1/3}$-dependence at high carrier densities [79]. The band gap shrinkage amounts to around 20 meV at sheet carrier densities above 10^{12} cm^{-2} in lattice-matched quantum wells, and even higher for strained quantum wells (due to increased carrier density in the heavy hole band) [80]. This means a shift of the optical transition shown in figure 3.5 from 980 nm to 995 nm.

However, contrary to a VCSEL, the eVCA is operated at high injection currents. Band filling shifts the wavelength of the optical transition downwards. In eVCAs, the band filling is estimated to almost compensate the band gap shrinkage of the quantum wells, wherefore the optical transition of the quantum wells in eVCA are designed only ~ 5 nm lower than the desired transition.

Another issue is the temperature-induced band gap shift; the temperature-dependent shift in the band gap energy is expressed by the empirical Vaarshni equation [81]

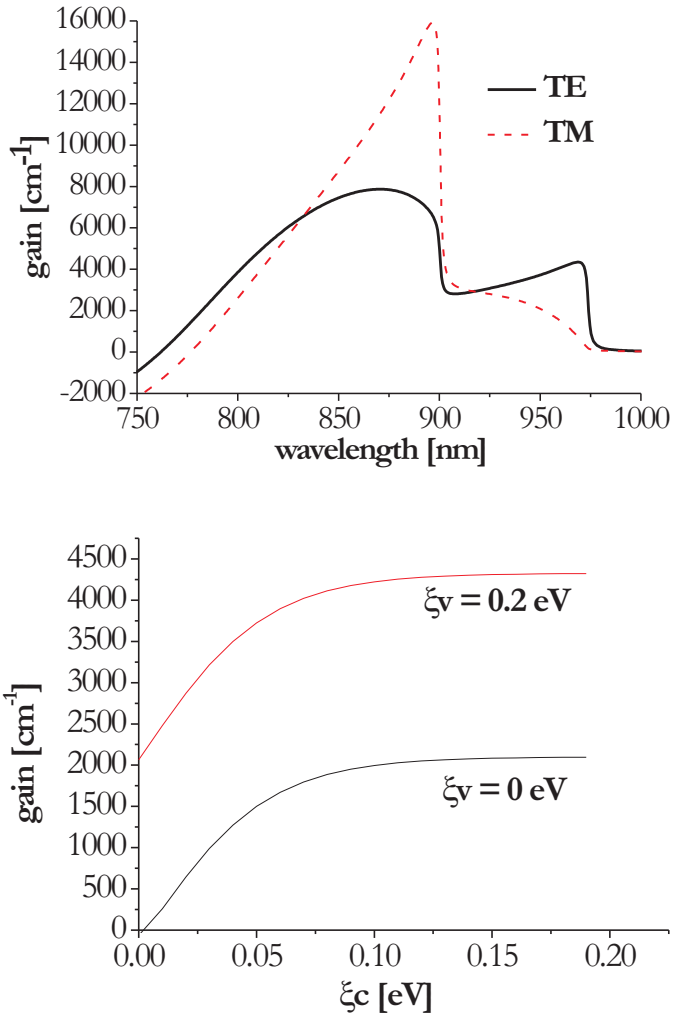

Figure 3.5: Top: gain coefficient of a $In_{0.17}Ga_{0.83}As$ quantum well on $GaAs$ designed with a conduction band to heavy hole transition at $\sim 980nm$. Bottom: the gain coefficient of the TE-polarised light of the conduction band to heavy hole transition as the separation of the electron quasi-Fermi Levels to the conduction bands, ξ_c, is increased from 0 to 0.18 at two different values of ξ_v.

$$E_g(T) = E_g(0) - \frac{\alpha_1 T^2}{\alpha_2 + T} \tag{3.3}$$

For $In_{0.2}Ga_{0.8}As$, α_1 and α_2 are $7.73 \cdot 10^{-4}$ eV/K and 458 K respectively [82], which gives a band-gap reduction of ~ 4 meV (a shift from 980 nm to ~ 983 nm) for a temperature change from 300 K to 350 K.

3.3.3 Strain of quantum wells

Epitaxially grown material is strained if the lattice constant is changed from its native lattice constant. The strain, ε is defined by

$$\varepsilon = \frac{a_{sub} - a_0}{a_0} \tag{3.4}$$

where a_{sub} and a_0 are the native in-plane lattice constants of the substrate and the unstrained quantum well material, respectively.

In structures presented in this thesis, the quantum well material, $In_{1-x}Ga_xAs$, where $0.80 < x \lesssim 0.83$, has an in-plane lattice constant of $5.72 - 5.74\mathring{A}$ while the host material, $GaAs$, has an in-plane lattice constant of $5.65\mathring{A}$. Since the host material has a lattice constant *smaller* than the quantum well material, the quantum well is said to be under *compressive* strain.

The hydrostatic (isotropic) component of the strain arises as the volume of the unit cell of the quantum well material is changed, and this shifts the band gap of the material. The shear (anisotropic) strain introduces a separation of the heavy hole and light hole bands at $\mathbf{k} = 0$. This separation leads to a smaller interaction between the heavy hole and light hole bands, which favours the conduction band to heavy hole band transition. Furthermore, the strain reduces the in-plane effective mass of the heavy hole band, i.e. increases the heavy hole band curvature to be closer to the curvature of the conduction band [78]. This leads to a more symmetrical separation of the quasi-Fermi levels and, as a result, the strained material has a lower transparency carrier density, which leads to a reduced carrier injection level. Due to this, the Auger recombination rate is reduced and the differential quantum efficiency is enhanced, leading to an increased differential gain and reduced internal loss [83].

A strained layer has a certain critical thickness after which the cells of the strained material *relax* into their original structure, leading to a number of unwanted dislocations in the crystal. Strain accumulates in the structure, i.e. strained material *distributed* in the grown structure can lead to dislocations in the structure. The critical thickness of $In_{0.2}Ga_{0.8}As$

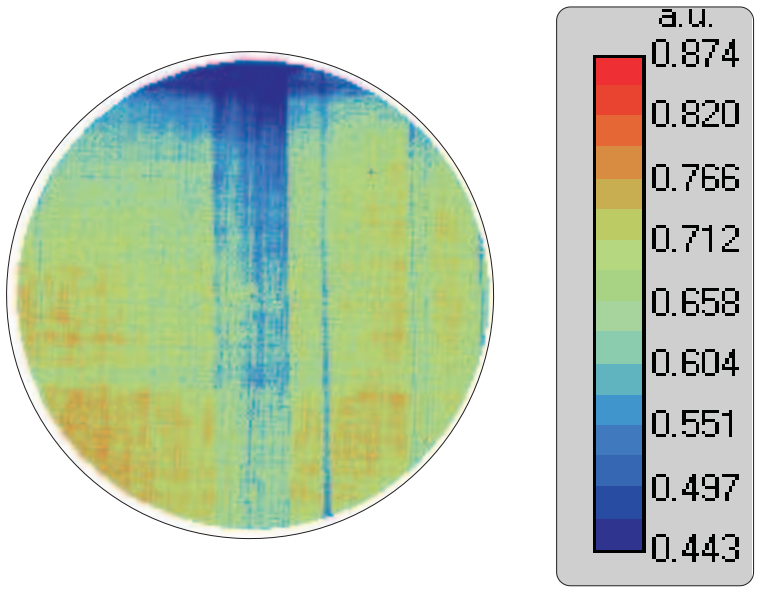

Figure 3.6: The intensity of the photoluminescence of a wafer (2 inches in diameter) with nine 8 nm $In_{0.2}Ga_{0.8}As$ quantum wells grown on $GaAs$. Streaks in the intensity indicate dislocations in the structure.

grown on $GaAs$ has been found experimentally to be around 26 nm [84]. Above this thickness, misfit dislocations appear on the surface of the structure. These local dislocations are accompanied with threading dislocations that disseminate through the epitaxial layers. The dislocations likely lead to deep-level states where carriers are recombining non-radiatively or are trapped. These dislocations are thus visible as dark lines in the nearfield of the emitted light or as streaks in the intensity of the photoluminescence as illustrated in figure 3.6, which shows the photoluminescence of nine 8 nm $In_{0.20}Ga_{0.80}As$ quantum wells grown on $GaAs$.

In order to guarantee no defects, one may strain-compensate by introducing a material that is *tensilely* strained, i.e. strained with an opposite sign. As $GaAsP$ has a lattice constant smaller than $GaAs$ (the lattice constant of $GaAs_{0.75}P_{0.25}$ is $\simeq 5.60$ $\mathring{A}$ [82]), epitaxial layers of $GaAsP$ in the compressively strained $In_xGa_{1-x}As/GaAs$ structure thus compensate for the strain and prevent defect formations. The thickness of the $GaAsP$-layers can be adjusted so as to compensate the strain completely.

Appendix A offers comprehensive calculations of the change in band positions in strained materials. The effect of strain in terms of shifting of

energy bands is included in the gain calculations of the previous section.

3.3.4 Segregation of *Indium*

When growing *In*-based materials such as $InGaAs$ quantum wells, the *In*-atoms are highly motivated to float to the surface of the growing wafer, i.e. change position with atoms on the surface of the wafer [85]. This surface segregation of In means that e.g. the interface of an $InGaAs$ quantum well on an $AlGaAs$ barrier will be graded in composition instead of abrupt. The thickness of composition-graded interfaces of $In_{1-x}Ga_xAs/GaAs$ quantum wells with $0.80 < x < 0.95$ can be as high as $2 - 3.5\ nm$ at a growth temperature of 520^oC. For a quantum well of composition $x \simeq 0.9$ and width $10\ nm$ this corresponds to a calculated shift in the quantum well transition energy from $1.430\ eV$ to $1.441\ eV$ when segregation is introduced, i.e. a shift of around 0.6 %. The calculated value of the shift of the transition is experimentally verified on quantum wells grown at 515 °C with a III/V-flux ratio of 1/8 [85]. Segregation of In also occurs in MOCVD-grown structures [86].

In order to avoid segregation of In, the growth temperature should be decreased as soon as In is introduced in the structure.

3.4 Barrier and spacer material

The barrier and spacer material has a great influence on the carrier distribution in the quantum well region and thus a great influence on the quasi-Fermi levels in the wells. In order to optimise the carrier distribution in the quantum well region, three different quantum well sections have been simulated using $SILVACO$.

The program $SILVACO$, which is presented in detail in appendix C, simulates the electrical and thermal behavior of 2-, or 3- dimensional semiconductor devices. It uses numerical techniques to solve the physical models of e.g. drift, diffusion and lattice heating using Fermi-Dirac or Boltzmann statistics, and can include radiative recombinations as well as non-radiative recombinations such as Shockley-Read-Hall and Auger recombinations.

The structure simulated is illustrated in figure 3.7; the quantum well section with 3 quantum wells is sandwiched between $\sim 2\ \mu m$ thick highly doped layers ($3 \cdot 10^{18}\ cm^{-3}$) of GaAs. The structure is disc-shaped and has a diameter of $10\ \mu m$. As we in these simulations are not interested in aperture-related (lateral) carrier distributions in the quantum wells we let the top and bottom contacts cover the whole top and bottom areas of the structure.

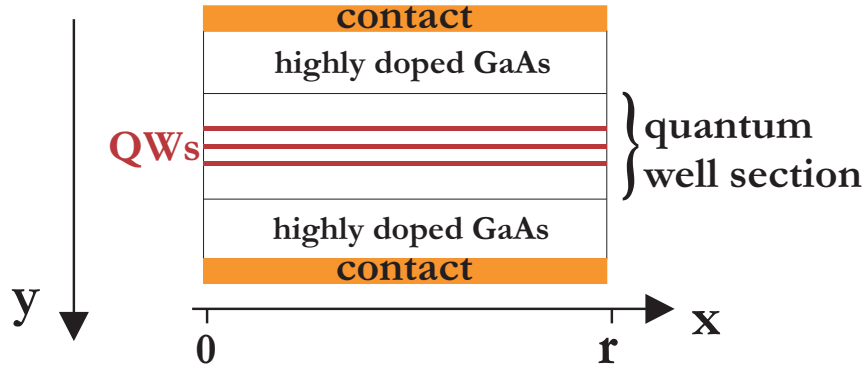

Figure 3.7: The structure simulated in *SILVACO*. Only the middle layers (marked with bracket) containing the quantum wells (QWs) are changed in the designs.

The three quantum well sections of the three designs each have 3 InGaAs quantum wells. The three designs differ in the barrier and spacer material which is illustrated in figure 3.8. The $InGaAs/AlGaAs$ design has $Al_{0.15}Ga_{0.85}As$ barriers and $Al_{0.4}Ga_{0.6}As$ spacer layers. The spacer layers have a thickness that fulfil the $\lambda/2$ requirement of the quantum well section. The $InGaAs/GaAs$ design has $GaAs$ barriers and $GaAs$ spacer layers and the $InGaAs/GaAsP$ design has $GaAs_{0.75}P_{0.25}$ barriers and $GaAs$ spacer layers. The quantum well sections are left un-doped in a region corresponding to a half wavelength of the standing optical wave. Outside this section, the doping levels of all three designs are alike.

The compositions and thicknesses of the quantum wells are designed to give an optical transition of 960 nm in the $InGaAs/AlGaAs$ design and an optical transition of 980 nm in the $InGaAs/GaAs$ and $InGaAs/GaAsP$ designs. The $InGaAs/GaAsP$ design is a strain-compensated design with 9 nm quantum wells and 12 nm barriers, whereas the two other designs have 8 nm quantum wells and 10 nm barriers. The quantum well designs matches the quantum well designs of actual eVCAs presented later in this thesis.

Stimulated emission is not included in the simulations of the carrier distribution. This means that the simulations assumes a neglecting top mirror reflectivity and furthermore, the gain saturation due to stimulated emission is neglected. The simulations are thus a LED analysis of the eVCA which would be a bad approximation if the simulated structure was a CW laser, e.g. a VCSEL. However, for small pulsation frequencies, i.e. where

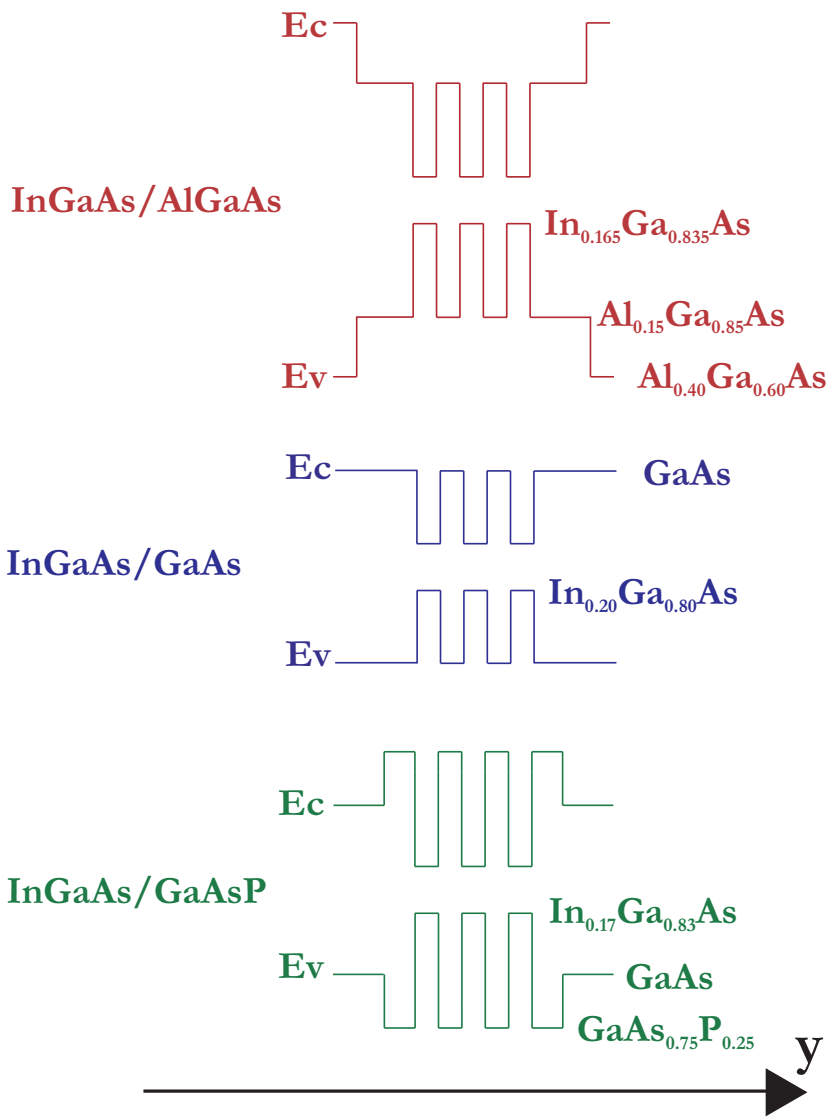

Figure 3.8: The conduction band, E_c, and valence band, E_v, of the three different quantum well sections simulated in *SILVACO*; the *InGaAs/AlGaAs* design (red), *InGaAs/GaAs* design (blue) and *InGaAs/GaAsP* design (green).

the gain recovery time is much smaller than the round trip time of the laser cavity, the eVCA is essentially a resonant-cavity light-emitting diode (RCLED) or a vertical-cavity semiconductor optical amplifier (VCSOA),

except for the short time the pulse is bouncing off the eVCA where the eVCA typically saturates.

The results of the simulations are interfaced to $TONYPLOT$, which is a program in $SILVACO$ that graphically illustrates the carrier densities, band line-up, quasi-Fermi levels etc. in the designs at different applied voltages. The carrier distributions in the structures can e.g. be plotted in $TONYPLOT$ by defining a cut-line in the y direction from top contact to bottom contact and plot the energy bands and quasi-Fermi levels along this cut-line.

The voltage across the structures is ramped up well above transparency. Transparency is reached when the separation of the quasi-Fermi levels exactly equals the band gap of the quantum wells. Table 3.1 sums up the applied voltages (and currents) at transparency, I_{tr} and V_{tr}, and well above transparency, I_2 and V_2. The $InGaAs/AlGaAs$ has a remarkably low transparency current compared to the two other designs. As revealed later in this section, the large transparency currents of the $InGaAs/GaAs$ and $InGaAs/GaAsP$ designs are due to a much higher (non-radiative) recombination rate in these structures.

design	V_{tr} $[V]$	I_{tr} $[mA]$	V_2 $[V]$	I_2 $[mA]$
$InGaAs/AlGaAs$	1.30	$5.83 \cdot 10^{-3}$	1.50	0.465
$InGaAs/GaAs$	1.33	5.23	1.40	25.7
$InGaAs/GaAsP$	1.28	1.71	1.40	55.2

Table 3.1: The voltage and current at transparency and well above transparency.

The energy bands and quasi-Fermi levels around transparency and well above transparency of the three designs are plotted in cut-lines from top contact to bottom contact. The result of the $InGaAs/AlGaAs$ design is illustrated in figure 3.9. The graphs show the bands and quasi-Fermi levels close to transparency (top graph) and well above transparency (bottom graph); the conduction band energy, E_c (red line), and quasi-Fermi level of the electrons, F_c (black line) and the valence band energy, E_v (cyan line), and quasi-Fermi level of the holes, F_v (blue line). The different materials of the structure are separated with black lines. The quantum wells are thus the middle three sections marked with **QW**. The black line to the right of the quantum wells marks the $Al_{0.15}Ga_{0.85}As/Al_{0.40}Ga_{0.60}As$ interface. The bends in the bands to the left of this interface originate in the doping of the structure; the quantum wells and the regions adjacent to the quantum wells are un-doped whereas the outer regions are doped with $3 \cdot 10^{18}$ cm^{-3}

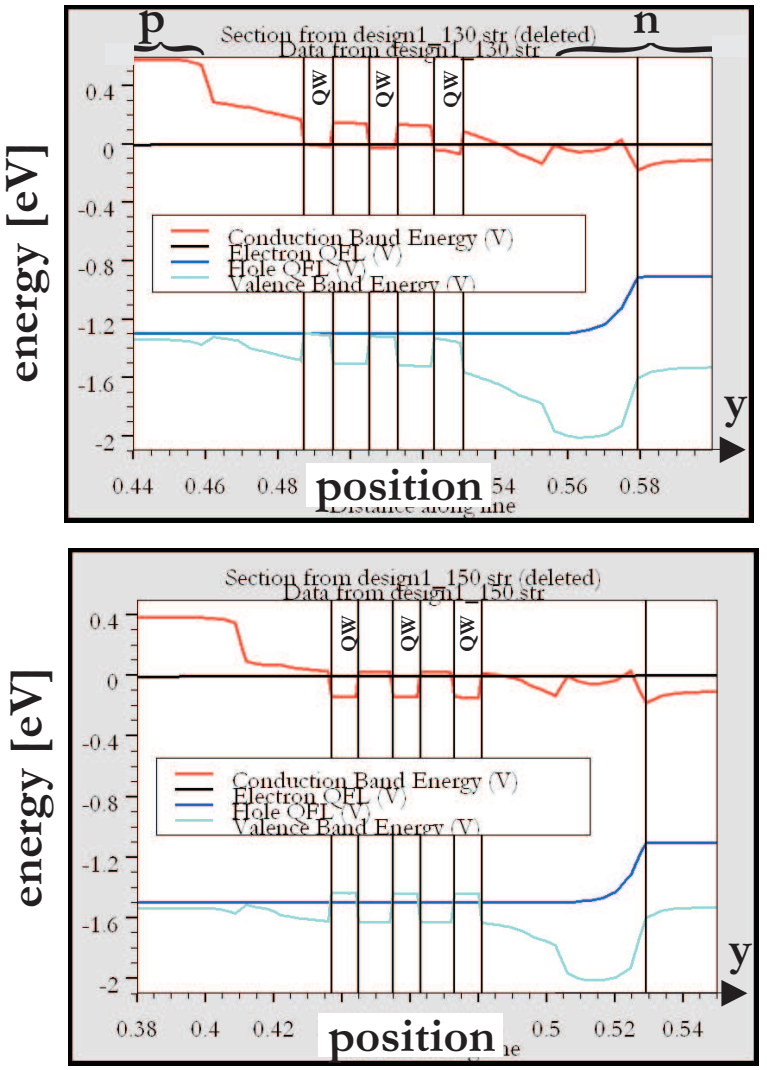

Figure 3.9: The conduction band and valence band and quasi-Fermi levels in the *InGaAs/AlGaAs*-design at transparency (top) and well above transparency (bottom).

as mentioned earlier.

The electron quasi-Fermi level on the n-side of the structure close to the quantum wells is lifted above the conduction band energy, which means that some electrons are trapped outside the quantum well region. However, as the current is increased (bottom graph), the separation of the electron quasi-Fermi level from the conduction band has only increased in the quantum wells. Furthermore, it is clear from the top graph of figure 3.9 that the density of electrons is larger in the well close to the n-doped side whereas the density of the holes is larger in the quantum well close to the p-doped side. This tendency also disappears at higher injection currents.

The energy bands and quasi-Fermi levels of the $InGaAs/GaAs$ and $InGaAs/GaAsP$ designs are shown in figure 3.10 and 3.11. The separations of the hole quasi-Fermi level to the valence band well above transparency in these two designs are not as high as the $InGaAs/AlGaAs$ design. In the $InGaAs/GaAs$ design (figure 3.10), the hole quasi-Fermi level is barely separated from the valence energy band at high injection currents. Furthermore, the electrons are trapped in the regions outside the quantum wells; they are separated from the quantum wells by a barrier created by the undoped layer of $GaAs$ adjacent to the quantum wells. This effect does not disappear at higher injection currents (bottom graph). The same effect appears in the $InGaAs/GaAsP$ design (figure 3.11), and here it is the barrier material that creates a barrier between the highly doped regions and the quantum wells. The high carrier density outside the quantum well region leads to a high non-radiative recombination rate outside the quantum well and a high current density at transparency.

The separations of the quasi-Fermi levels to the energy bands in the quantum wells, ξ_c and ξ_v, have been measured in all three wells of the three designs at increasing injection currents. The result is illustrated in the top graph of figure 3.12. The filled symbols represent the separation (in units of eV) of the electron quasi-Fermi level to the conduction band and the empty symbols represent the hole quasi-Fermi level to the valence band. The applied current is here expressed in current density, J, in units of A/cm^2. It is clear that the separations of the quasi-Fermi levels to the energy bands obtained in the $InGaAs/AlGaAs$ structure are higher than in the other designs. The separations in the $InGaAs/AlGaAs$-design saturate at 0.32 eV and 0.15 eV for the conduction and valence band respectively. The separations of the two other designs saturate at around 0.08 eV and 0.016 eV. At smaller current injections, where the devices would operate when working as amplifiers in lasers, the separation values of the $InGaAs/AlGaAs$ design are around one order of magnitude bigger

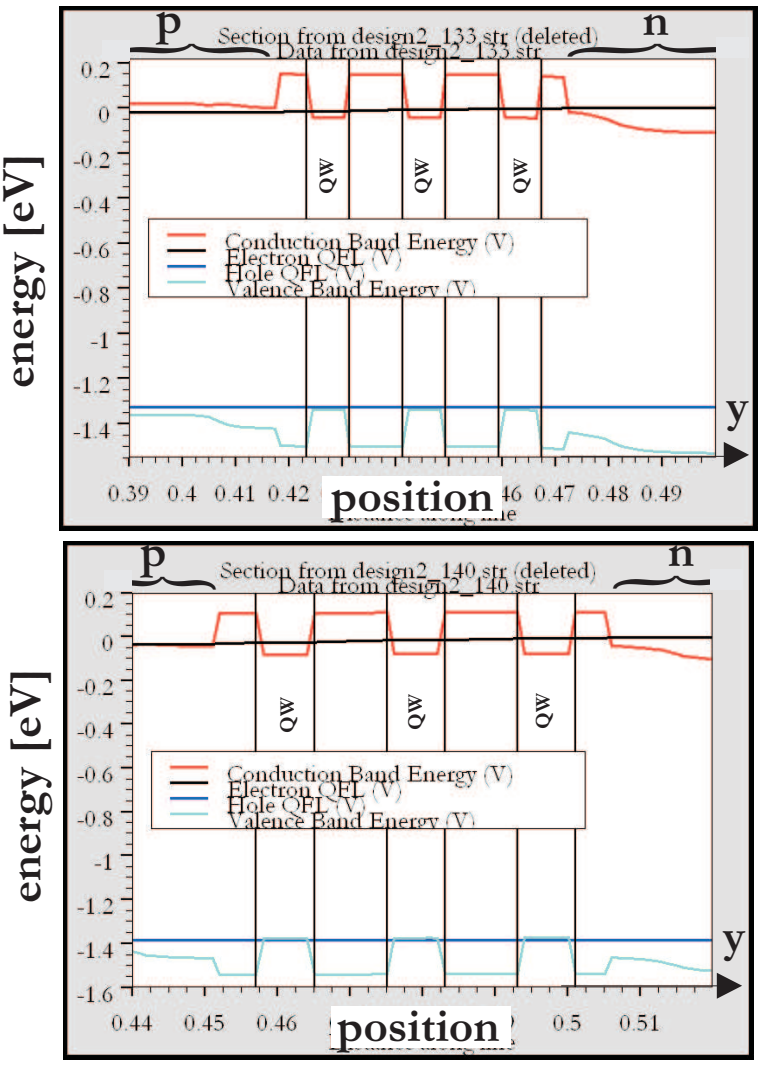

Figure 3.10: The conduction band and valence band and quasi-Fermi levels in the *InGaAs/GaAs*-design at transparency (top) and well above transparency (bottom).

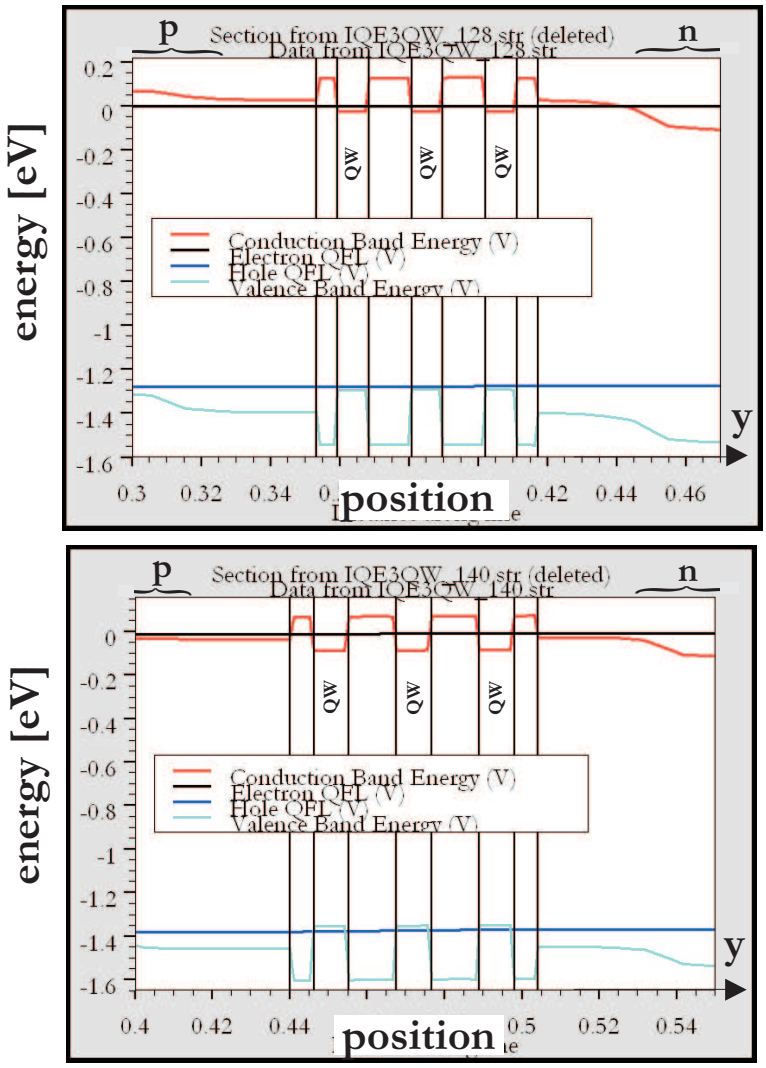

Figure 3.11: The conduction band and valence band and quasi-Fermi levels in the *InGaAs/GaAsP*-structure around transparency (top) and well above transparency (bottom).

than in the other two designs.

The bottom graph of figure 3.12 shows the gain coefficients in the three designs at the saturated separation values from the top graph of figure 3.12. The maximum gain coefficient at the design wavelength for the $InGaAs/AlGaAs$, $InGaAs/GaAs$ and $InGaAs/GaAsP$ designs are 4650, 2619 and 2732 cm^{-1} respectively.

As discussed earlier in this section, the energy bands and quasi-Fermi levels of the three designs (figure 3.9, 3.10 and 3.11) show that a considerable amount of carriers will recombine outside the quantum wells. The total recombination rate (black line) and the *radiative* recombination rate (red line) of the $InGaAs/GaAs$-design at 1.4 V is illustrated in figure 3.13. The $InGaAs$ quantum wells are illustrated with blue areas and the $GaAs$ regions are green. The $TONYPLOT$ program allows integration of the curves in figure 3.13, thus enabling the possibility of summing up the radiative recombination rates inside and outside the quantum wells. The radiative recombination rates have been calculated by using graphs similar to figure 3.13 for all three designs at different applied current densities. The result is illustrated in figure 3.14, which shows the radiative recombination rates inside (filled symbols) and outside (empty symbols) the quantum wells in units of $s^{-1}cm^{-2}$. The radiative recombination rate in the quantum wells increases to $\sim 2.7 \cdot 10^{22}$ $s^{-1}cm^{-2}$ in the $InGaAs/AlGaAs$ design and only around $\sim 4 \cdot 10^{20}$ $s^{-1}cm^{-2}$ in the two other designs. The radiative recombination rate *outside* the quantum well region exceeds the recombination rate in the wells at a current density of $\sim 22 \cdot 10^3$ A/cm^2 in the $InGaAs/AlGaAs$ design. In the two other designs, the radiative recombination rate outside the quantum wells is larger than the radiative recombination rate inside the quantum wells at all injection currents.

The sum of the radiative recombination rate inside and outside the quantum wells is not the same for all three structures due to the fact that the $InGaAs/GaAs$ and $InGaAs/GaAsP$ designs have a much higher non-radiative recombination rate in the overall structure.

The above simulations show a clear indication of a better carrier distribution in the $InGaAs/AlGaAs$ design compared to the $InGaAs/GaAs$ and $InGaAs/GaAsP$ design. It should, however, be kept in mind that as the $InGaAs/GaAsP$ design is a strain-compensated design, more than three wells of this material combination can be grown in the eVCA, whereas only three wells of the $InGaAs/AlGaAs$ or $InGaAs/GaAs$ combination can be grown without ending up with dislocations in the structure. The single pass gain of three 9-nm $InGaAs/AlGaAs$ quantum wells with a gain coefficient of 4650 cm^{-1} is equal to $e^{gd} = 1.013$. The single pass gain

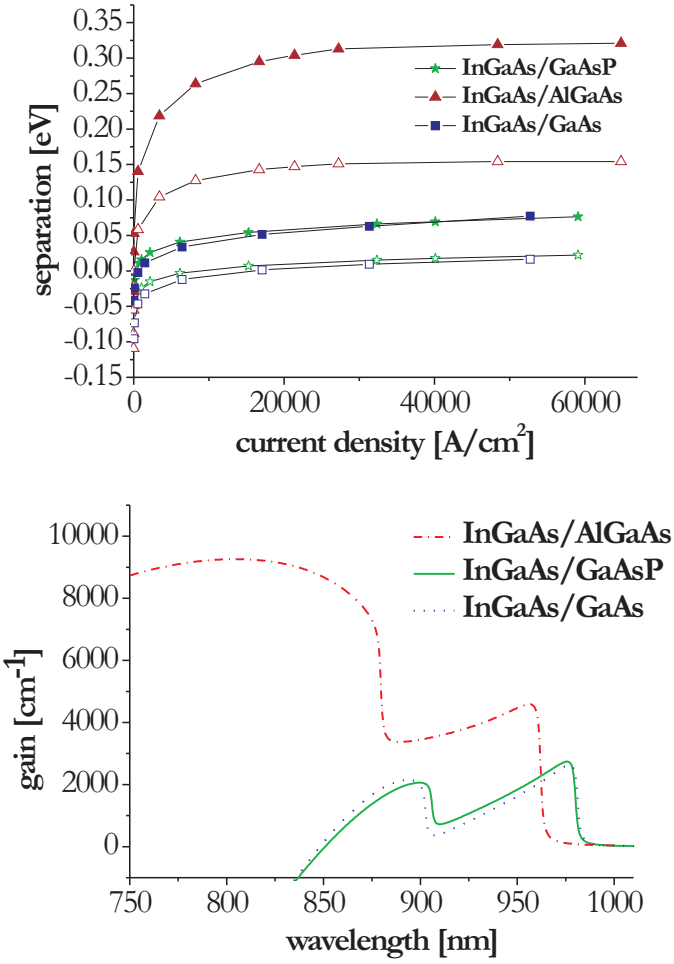

Figure 3.12: Top graph: The separations of the quasi-Fermi levels from the conduction band (ξ_c, filled symbols) and the valence band (ξ_v, empty symbols) inside the quantum wells in the three structures. ξ_c and ξ_v saturate at 0.32 eV and 0.15 eV in the $InGaAs/AlGaAs$ design and at 0.08 eV and 0.016 eV in the two other designs. Bottom graph: Gain coefficients in the three designs at the saturation values of the separations shown in the graph above. The maximum gain coefficients in the $InGaAs/AlGaAs$, $InGaAs/GaAs$ and $InGaAs/GaAsP$ structures in heavy-hole transition is 4650, 2619 and 2732 cm^{-1} respectively.

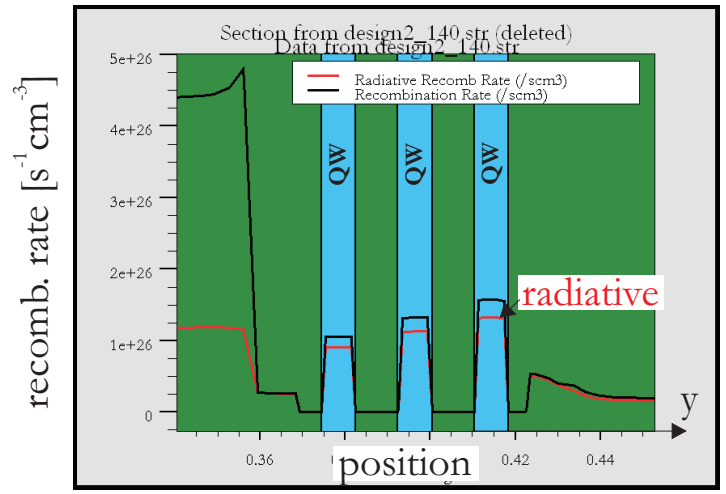

Figure 3.13: The radiative and non-radiative recombination rates around the quantum wells (blue) in the $InGaAs/GaAs$ design. The green areas are $GaAs$.

of nine 9-nm $InGaAs/AlGaAs$ quantum wells with a gain coefficient of 2732 cm^{-1} is equal to $e^{gd} = 1.022$, i.e. according to the simulations, the $InGaAs/GaAsP$ design can offer up to almost twice as much single pass gain than the $InGaAs/AlGaAs$ design.

3.4.1 Doping of barriers

The relatively deep confinement potential in the valence band may give rise to difficulty for the holes to distribute homogeneously over the quantum well section. This problem can be decreased by p-doping the barriers that embed the wells. A p-doping around the wells builds an electric field from the well and out, thus bending the potentials in the well downward and decreasing the depth of the well. This reduction of the effective valence band offset comes at the expense of a higher free-carrier absorption (treated in section 3.5).

The simulations above have been repeated for the $InGaAs/AlGaAs$ design with different doping levels of the barriers. The separation values and the radiative recombination rates inside and outside the quantum wells are presented in table 3.2.

The simulations show almost no difference in the valence band quasi-

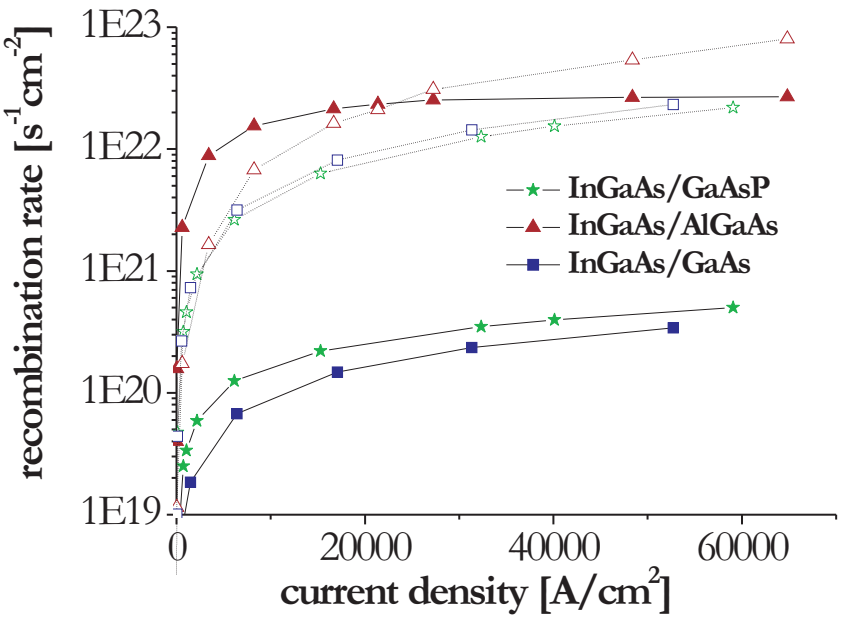

Figure 3.14: The radiative recombination rates in the QWs (filled symbols) and outside the QWs (empty symbols) of the three structures.

Fermi level at high currents. The difference is visible in the recombination-rates inside and outside the quantum wells, which seems to degrade at higher doping-levels.

doping level $[cm^{-3}]$	J $[kA/cm^2]$	ξ_c $[eV]$	ξ_v $[eV]$	R_{QW} $[10^{22}s^{-1}cm^{-2}]$	R_{out} $[10^{22}s^{-1}cm^{-2}]$
un-doped	65	0.32	0.15	2.69	8.01
$5 \cdot 10^{17}$	64	0.32	0.15	2.67	8.23
$1 \cdot 10^{18}$	64	0.32	0.15	2.43	8.57
$3 \cdot 10^{18}$	63	0.32	0.15	2.67	8.43
$5 \cdot 10^{18}$	62	0.32	0.15	2.67	8.53

Table 3.2: Quasi-Fermi levels and radiative recombination rates inside, R_{QW}, and outside, R_{out}, the quantum wells in the $InGaAs/AlGaAs$ design simulated in $SILVACO$ for different p-doping levels of the barriers.

3.5 Doping and free-carrier absorption

A high doping ensures a good electrically conductive eVCA and thus a low heat dissipation. However, doping of the structure means many free carriers. The rate of free-carrier absorption is a product of the photon capture cross section of the carriers, the number of carriers present *and* the overlap with the optical field. Due to free-carrier absorption, highly doped layers should thus be restricted to layers in the structure, where the optical field is low. The free-carrier absorption coefficient in $GaAs$ near the band gap energy is [87]

$$a = 3 \cdot 10^{-18} n + 7 \cdot 10^{-18} p \tag{3.5}$$

a is expressed in cm^{-1}, and n and p, the electron-, and hole-concentration, in units of cm^{-3}. The above absorption coefficient is assumed valid for all materials in the structures.

When the top contact on a bottom-emitting structure is positioned on top of the substrate as illustrated in figure 3.2, the doping of the substrate will mean that the emitted light will suffer from free-carrier absorption in the substrate. The free-carrier absorption in a substrate of thickness t gives rise to an absorption per round trip of the optical field intensity equal to

$$A = e^{-2ta} \tag{3.6}$$

which in a n-doped substrate with a doping level of $2 \cdot 10^{18}$ cm^{-3} and thickness of 50 μm gives an absorption of 5.9 %.

In order to minimise or remove completely the free-carrier loss in the substrate, the bottom-emitting eVCAs can either be designed with intra-cavity n-contacts [88,89] as illustrated to the left in figure 3.15. In this case, the substrate need not to be doped. The n-contact need, however, to be contacted to a highly n-doped layer in the structures which will induce some free-carrier absorption in the structure. If the n-contact is positioned on top of the substrate thinning of the substrate can minimise the free-carrier absorption in the substrate. Additionally, the substrate can be removed *entirely* by epitaxial lift-off or by selective etching, or *part* of the substrate can be etched away over the active eVCAs, illustrated to the right in figure 3.15. In both cases, free-carrier absorption of the emitted light is decreased.

3.6 Distributed Bragg-reflectors

Alternating quarter-wavelength thick layers of high and low refractive-index materials, e.g. $AlGaAs$ and $GaAs$, form distributed Bragg reflectors

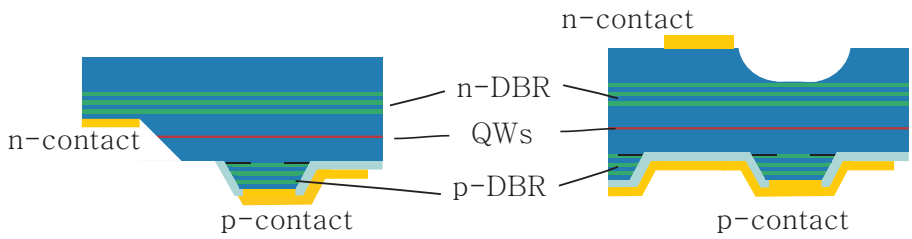

Figure 3.15: Two suggestions of how to minimise the free-carrier absorption in the bottom-emitting structures. To the left, intra-cavity contacting of the n-contact thus avoiding a doped substrate. To the right, etching away the substrate on top of the active eVCAs thus minimising the free-carrier absorbtion of the emitted light.

(DBRs). Such reflectors are based on successive internal reflections; incident light perpendicular to a single interface of two materials with refractive indices n_{high} and n_{low} undergoes an intensity reflection of $(\frac{n_{low}-n_{high}}{n_{low}+n_{high}})^2$. A single $GaAs/AlAs$ interface thus has an intensity reflection of $R \simeq 0.6$ %. Letting each layer of the DBR have an optical thickness of a quarter wavelength of the design wavelength, λ_B (or Bragg wavelength), gives reflections *in phase* with the original field, as the field experiences a π phase-shift at each reflection. An optical field with a wavelength away from the Bragg-wavelength will build up a phase mismatch with the incoming field thus resulting in a smaller net reflection. The reflection of the field will therefore fall off away from the Bragg wavelength, and the thicker a Bragg reflector the broader a bandwidth.

The intensity reflection of a stack of M pairs of layers with thickesses $\lambda_B/4n_{low}$ and $\lambda_B/4n_{high}$ is equal to [5]

$$R = tanh^2(\frac{M}{2}(\frac{n_{high}}{n_{low}} - \frac{n_{low}}{n_{high}})) \tag{3.7}$$

In order to ensure a reflectivity of ~ 100 %, a stack of around 30 periods of $AlAs/GaAs$ layers is required. The penetration depth of the optical field in such a stack is equal to $L_{eff,DBR} = \frac{\sqrt{R}\lambda_R}{4\Delta n}$, which is roughly $400nm$ for $AlAs/GaAs$- DBR with $\lambda_B = 960\ nm$ [5].

The mirror that includes the oxidation aperture (the p-DBR in case of figure 3.16) should have an Al-content *smaller* than the oxidation layer itself, which is made of $Al_xGa_{1-x}As$ where $x = 0.98 - 1.00$, in order to be able to selectively oxidise the aperture only (see section 3.7).

In a normal structure as illustrated in figure 3.16, the DBRs should

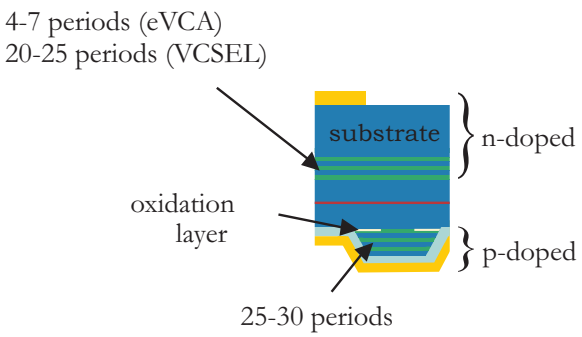

Figure 3.16: The distributed reflectors in a bottom-emitting eVCA or VCSEL. Here, the bottom-DBR is p-doped and the top-DBR n-doped.

show a sufficiently low series resistance. A high resistance gives rise to Joule heating that in turn lowers the efficiency of the device. The ohmic resistance in DBRs originates from the ohmic resistance in the bulk material and the hetero-junction barriers. The bulk resistivity can be lowered by doping the layers, which unfortunately gives rise to an optical loss in terms of free-carrier absorption. The resistivity caused by the hetero-junction barriers can be partially solved by grading the composition and the doping profiles at each interface.

The p-doped and n-doped DBR will be treated individually below.

3.6.1 P-doped DBR

Since holes have a higher mass and thus a lower mobility than electrons, p-DBRs need to be doped more *heavily* than n-DBRs. C and Be are most commonly used for p-type doping, however, Be is very diffusive in $AlAs$ and therefore tends to diffuse out of the $AlAs$ layer and accumulate on the $GaAs$-side of the $AlAs/GaAs$ interfaces [90]. The accumulations of Be modulates the valence band and results in high hole barriers at the interfaces. $GaAs/AlAs$ p-doped DBRs are therefore normally substituted with $GaAs/Al_xGa_{1-x}As$ DBRs (x around 0.7); besides from having smoother Be-doping profiles in such mirrors, lower hetero-junction barriers will lead to lower resistivity. In order to enhance the doping level in the $AlAs$ or $AlGaAs$ layer, delta doping can be used on the $AlGaAs/GaAs$ interfaces. In delta doping, all other sources than the doping source is closed, i.e. the wafer experiences a high doping level while no growth is performed.

Another option is to use C-doped DBRs as the $AlAs$ layers with no difficulty can be C-doped up to $2 \cdot 10^{19}$ cm^{-3} [90].

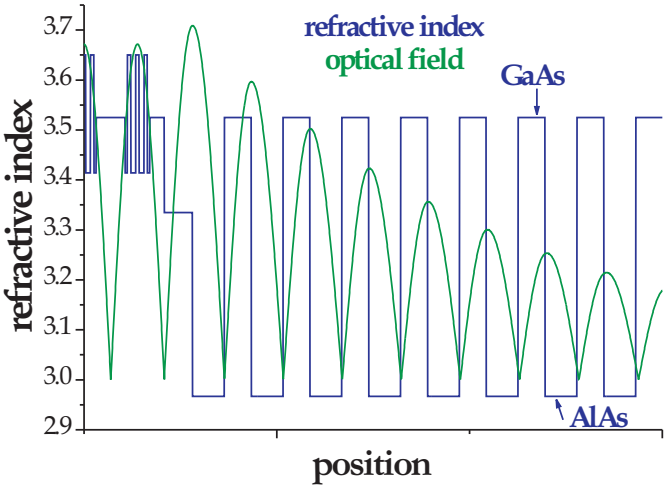

Figure 3.17: An example of an $AlAs/GaAs$-DBR; the refractive index in (blue line) and the standing optical wave in the structure (green line) calculated by a transfer matrix method in MATLAB.

In order to ease the transport of holes, flat-band engineering of the valence band in p-DBRs can be performed. Especially on the $GaAs/AlGaAs$ interface, where the holes travel from the small band gap material $GaAs$ to the large band gap material $AlGaAs$ is flat-band engineering necessary. The engineering consists of replacing the abrupt $GaAs/AlGaAs$ or $GaAs/AlAs$ interfaces by $18-20\ nm$ graded interfaces where the Al-composition is gradually changed from e.g. 0 to 1 *and* by grading the doping-profile in the interfaces [91]. The thickness of the gradings should roughly be equal to the depletion-width of the junction, which e.g. is $20-23\ nm$ for a $10^{18}\ cm^{-3}$ doped $Al_xGa_{1-x}As/GaAs$-interface, where $0.7 < x < 1.0$ [92]. The graded interfaces can consist of a single stair-case grading (SC) or a super-lattice grading (SL), both illustrated in figure 3.18. The SC-grading consists of a single step at the interface with an Al-content half of the content in the $AlGaAs$ layer, the SL-grading consists of alternating layers of $1nm\ GaAs$ and $1nm\ AlGaAs$.

Flat-band engineering with *uniformly doped* interfaces on $Al_{0.70}Ga_{0.30}$-$As/GaAs$-DBRs and $AlAs/GaAs$-DBRs has been shown to reduce the series resistance of the mirrors by two orders of magnitude [93,94]. The most simple way to perform a composition and doping graded interface in an

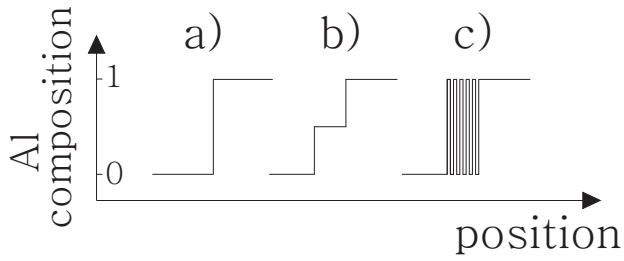

Figure 3.18: Interfaces of a $GaAs/AlAs$ DBR with composition gradings: a) no grading b) staircase (SC) grading and c) uniform superlattice (SL) grading.

$AlGaAs/GaAs$ DBR is by high-doping the part of the grading close to the $AlGaAs$ layer whereas the part close to the $GaAs$ layer is left un-doped. This type of grading has analytically and experimentally shown to have fairly flat valence bands [92, 95]. The un-doped region close to the $GaAs$ layer can with advantage be replaced by an *n-doped* layer [96].

3.6.2 N-doped DBR

As electrons have a much higher mobilities than holes, not much attention has been paid to fabrication of flat-band engineered n-doped DBRs. However, in growth machines where composition and doping graded interfaces can be introduced in the grown structure with no difficulty, SC or SL gradings in n-DBRs can be used with advantage [97].

Furthermore, as e.g. Si-doping is found to enter the $AlAs$ layers with no difficulties [90], there is no need to grow $AlGaAs/GaAs$-DBRs, as is the case with p-doped DBRs.

3.7 Oxide layer

An oxide layer that confines the lateral current around the active layers provides a smaller threshold current of the eVCA which leads to a smaller heat dissipation in the structure.

The oxide aperture is illustrated as yellow lines on figure 3.2. The layer consists of $Al_xGa_{1-x}As$, where $0.98 < x < 1.00$. The oxidation of the layer is usually done in a chamber heated to $300 - 400\ ^\circ C$ with an atmosphere of water-vapour. This means that oxidation of the $AlGaAs$ layers requires access to the side of the layer by etching mesas into the structures *through* the oxidation-layer. When $AlGaAs$ is oxidised, a porous mixture of Al_2O_3 and $Al_2O_3 \cdot mH_2O$ is formed ($0 < m < 3$) which is

electrically insulating [98]. Furthermore, since $Al_2O_3 \cdot mH_2O$ has a smaller refractive index than $AlGaAs$ ($\simeq 1.6$ versus $\simeq 3$), the oxide layer also works as a transversal confinement of the optical field [99].

The oxidation rate depends on the composition of the oxidation layer, the thickness of the layer and the composition of the surrounding layers [100, 101]. Also, exposing the $AlGaAs$ oxidation layer to air might *seal* the surface of the layer. It is thus important to minimise the time between the etch of the mesas and the oxidation process. The sealing of the layer leads to a delay in the oxidation process [102].

The oxide layer has a lattice constant smaller than $GaAs$. Thus, in order to spread strain effects caused by the oxidation, a layer of $AlGaAs$ can with advantage be deposited on both sides of the $AlAs$ oxidation layer [99].

A current confinement is especially needed in the p-side in the top-emitting structures and in the n-side of the bottom-emitting structures, as the contacts on these sides do not cover the active area

3.8 Current-spreading layers

Devices with large apertures need current-spreading layers in order to laterally spread the current from the top contact to the area of the active layers. No current spreading would lead to a crowding of the current around the oxide layer which in turn would lead to heating of the device and lower the performance of the device. Also, a non-uniform lateral current density in the quantum wells will not favour gain of the transversal fundamental mode of the laser.

Different approaches to lateral current-spreading layers in light-emitting diodes (LED) have been discussed in literature. The top-contact can e.g. be shaped in a web-like pattern *across* the aperture of the LED; this type of contact is shown to enhance the output power of a wide-area LED by a factor of 4 [103]. Another solution is to use transparent contact-layers; the highly conductive layers spread the current laterally [104], however, they also have a high free-carrier absorption coefficient that would absorb a considerable amount of the emitted photons. Alternatively, the lateral current spreading can be enhanced by growing an un-doped layer [105] or a doped low band-gap layer [106] adjacent to the quantum well sections of the LED. These layers will enhance the transport of electrons or holes in the lateral direction. In this section, we will investigate current-spreading layers based on high and low doped regions grown into the structure of the eVCA.

In case of the top-emitting structure, the current-spreading layers should

spread the holes from the ring-shaped top contact to the active area defined by the oxide aperture. The current-spreading layers in the bottom-emitting structure should be positioned above or below (or instead of) the n-DBR to spread the electrons from the n-contacts to the active area. This section analyses the current-spreading layers in a bottom-emitting device, wherefore only spreading of electrons are considered here.

The current density of electrons with effective mass m and charge $|e|$ is a combination of drift and diffusion, expressed by

$$\mathbf{J}_n = ne\mu_n\mathbf{E} + \mu_n kT \bigtriangledown n \tag{3.8}$$

where μ_n is the electron mobility and $\bigtriangledown n$ is the gradient in the density of electrons, n. The mobility equals $\langle\tau_m\rangle|e|/m$ where $\langle\tau_m\rangle$ is the momentum relaxation time. This relaxation time depends on the scattering processes in the material; i.e. *phonon scattering*, where carriers scatter on vibrations of the lattice, *impurity scattering*, where carriers scatter on impurities. In un-doped materials at room temperature, the phonon scattering dominates over impurity scattering due to enlarged lattice vibration [107]. In doped materials, however, the impurity scattering may dominate at room temperature; the electron mobility in $GaAs$ decreases from 8000 cm^2/Vs at an impurity concentration of 10^{14} cm^{-3} to around 2000 cm^2/Vs at an impurity concentration of 10^{18} cm^{-3}. The hole mobility decreases from 400 $\frac{cm^2}{Vs}$ to around 200 $\frac{cm^2}{Vs}$ at the same impurity concentrations [107]. The lower effective mass of the electron is the reason for the higher mobility of electrons relative to holes.

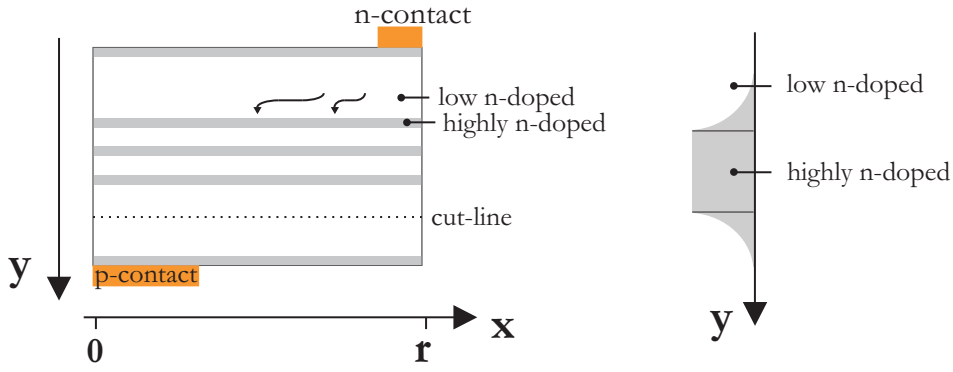

Figure 3.19: The bottom-emitting structure simulated in *SILVACO*. The grey area represents the highly doped layers.

A sketch of a bottom-emitting eVCA with its n and p contacts is shown

to the left in figure 3.19. The sketch is out of scale; the bottom contact of a bottom-emitting eVCA is typically $30 - 100\ \mu m$ in diameter whereas the thickness of the eVCA structure itself is $3 - 5\ \mu m$ (without substrate). The current-spreading layers are positioned underneath the n-contact and should ideally consist of low resistive material with high mobility, in order to spread the carriers in the x direction, and low doping concentration, to decrease free-carrier absorption. As these criteria are counteractive, current-spreading layers can consist of thin highly doped layers positioned in the nodes of the optical field. These layers are illustrated as grey layers to the left of figure 3.19. The current density of electrons in these layers is large which makes the electrons move along the layers in the x direction. Furthermore, electrons from these highly doped layers diffuse into the low doped regions with higher mobility, as illustrated to the right in same figure, thus further enhancing the lateral motion of the electrons on the interfaces of the low-doped and highly doped regions.

Hetero-junctions of e.g. $GaAs$ and $AlAs$ work the same way; when hetero-junctions are e.g. n-doped, spikes in the conduction band will occur on the interfaces of $GaAs$ and $AlAs$. This will lead to spikes in the electron densities and thus high drift velocity along the interfaces. This means that a DBR is a good current spreader.

A current-spreading section consisting of 5 highly doped layers has been simulated in $SILVACO$ (see details of the program in appendix C). The simulated structure is similar to the sketched structure shown in figure 3.19. The simulation is performed in cylinder coordinates where $x = 0$ is the axis of symmetry, the structure has a radius of 116 μm and the x-axis represents the lateral distance from the centre of the aperture. The width (and radius) of the bottom contact is 15 μm and it is positioned in the left corner from $x = 0$ to $x = 15\ \mu m$ whereas the top-contact has a width of 1 μm and is located on the top right corner of the eVCA.

The highly doped layers have a thickness of 30 nm and a doping level of $10^{19}\ cm^{-3}$ and the the surrounding low-doped layers have a thickness of 109 nm and a doping level of $10^{17}\ cm^{-3}$. The layers adjacent to the n- and p-contacts are highly doped ($10^{19}\ cm^{-3}$) in order to minimise the resistivity of the structure in the simulations.

The total lateral current density (in the x-direction), J_x, of the structure is shown in the contour plot (top graph) of figure 3.20. The red areas represents layers where the lateral current density is high and purple areas represents layers where the lateral current density is low. The highly doped layers including the layers adjacent to the contacts have a high lateral current density. Some of the carriers do not spread in the thin current-

spreading layers but in the highly doped layer adjacent to the contacts. The bottom graph shows the total current density in a plane in the structure defined by the dotted line in the top graph of figure 3.20. The bottom graph shows the enlarged lateral current density, J_x, in the highly doped layers *and especially* on the interfaces of the low-doped and highly doped regions.

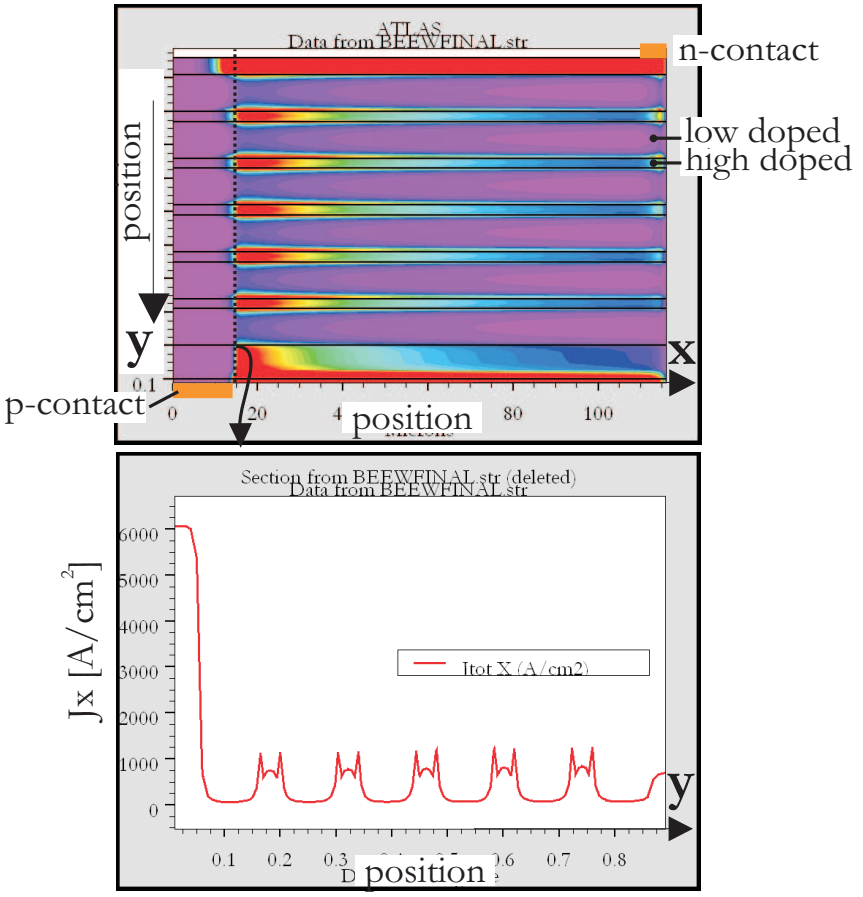

Figure 3.20: Top: A contour plot of the current density in the x-direction, J_x, in a structure with five current-spreading layers. Each layer is 30 nm thick and is doped by $1 \cdot 10^{19}$ cm^{-3}. The surrounding material is doped with $1 \cdot 10^{17}$ cm^{-3}. Bottom: The current density in the five layers shown in the cut-line illustrated in the top figure.

Figure 3.21 shows the total current density in the y direction, J_y, plotted in a cut-line represented as a dotted line in figure 3.19. The top graph is the

structure without any current-spreading layers, i.e. with uniformly doped layers (10^{17} cm^{-3}). The bottom graph is for a structure with 5 current-spreading layers. The arrows shows the $x = 0$ and the $x = 15$ μm position where the bottom contact is located.

Since a lot of the carriers spread laterally in the highly doped layer positioned *under* the cut-line, the magnitudes of the total current density of the two structures in figure 3.21 are not comparable. The current density on the two plots shows an enhancement of the current density profile in the x direction in the structure with 5 current-spreading layers. A similar simulation of a structure without current-spreading but with layers uniformly doped with 10^{19} cm^{-3} has been performed, and it had a current density profile very similar to the top graph of figure 3.21. However, according to the simulations, significant improvements of the current-spreading layers would have to be achieved in order to induce a uniform current density profile across the aperture of the device.

A similar simulation with 10 current-spreading layers has been simulated as well. The results is presented in appendix B at page 175; it shows a small enhancement of the carrier density profile when the number of current-spreading layers is increased from 5 to 10.

3.9 Contacts

As contact material we had the following metals available; Cr, Ge, Ni, Ti, Pt and Au. A number of alloys based on these metals can be used for contacting the eVCA. In the following, the metal mentioned first is the metal deposited first.

The most well-documented n-type contact for $GaAs$-based structures is the $Ni/Ge/Au$ contact; the presence of Ge makes the Ni_2GeAs-alloy n-type doped, and the first layer of Ni enhances the adhesion of the contact to the $InGaAs$ [108]. The contact should be annealed at $T > 300$ $^{\circ}C$, otherwise it will turn out with a high sheet resistance. However, complete intermixing of the layers was observed at annealing temperatures as high as ~ 450 $^{\circ}C$. The contact resistance of a $Ni/Ge/Au$ contact grown on $InGaAs$ with $5 \cdot 10^{18}$ cm^{-3} Si-doping is reported to be 10^{-6} and 10^{-8} Ωcm^{-2} for contacts annealed at 300 ^{o}C and 400 ^{o}C respectively. Wire bonding on a $Ni/Ge/Au$ contact is poor and even impossible if the semiconductor device has not been deoxidised in dissolved NH_4OH ($H_2O : NH_4OH = 20 : 1$) or HCl before deposition [109, 110].

$Ti/Pt/Au$ is an n-type contact, that has a ohmic behaviour even when un-annealed. The contact resistance for an un-annealed $Ti/Pt/Au$ contact

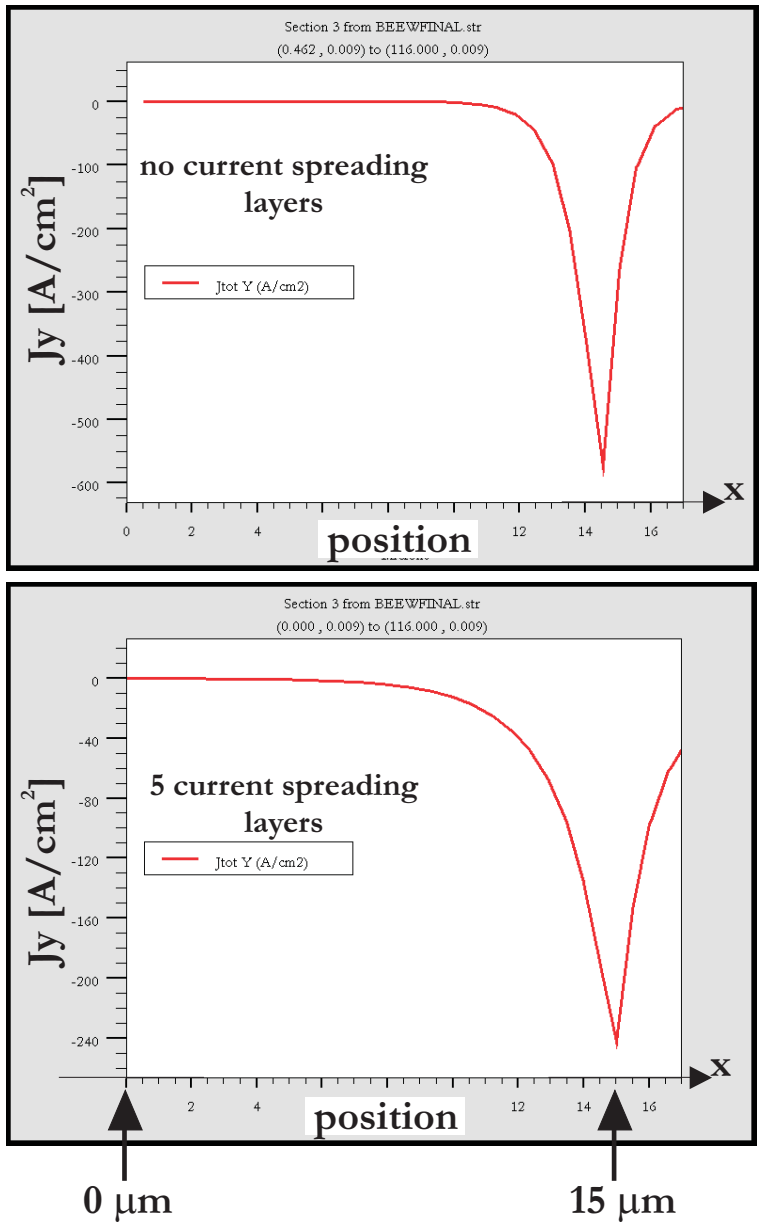

Figure 3.21: The total current density in the y direction, J_y, plotted in a cut-line positioned at the dotted line of figure 3.19. The top graph is the structure without any current-spreading layers, i.e. with a uniformly doped section (10^{17} cm^{-3}). The bottom graph is for a structure with 5 current-spreading layers.

grown on $GaAs$ with $2 \cdot 10^{18}$ cm^{-3} Si-doping of $5 \cdot 10^{-4}$ Ωcm^{-2} [111]. Also the morphology, adhesion and bonding ability of an un-annealed $Ti/Pt/Au$ (50/50/700 nm) contact on un-doped $GaAs$ is found to be good [109].

The most simple p-type contact is the Cr/Au contact. Cr is a good ohmic contact material to p-type $GaAs$ but do form a Schottky barrier (ϕ_b = 700-800 meV) when used on n-type $GaAs$. On $GaAs$ with $5 \cdot 10^{18}$ cm^{-3} Zn-doping, the Cr/Au contact has a relatively high contact resistance of $1 \cdot 10^{-4}$ Ωcm^{-2} un-annealed and $2 \cdot 10^{-5}$ Ωcm^{-2} when annealed at 430 $°C$ [112].

All used contacts are summarised in table 3.3.

substrate doping $[cm^{-3}]$	metal	annealing $[°C]$	resistance $[\Omega cm^{-2}]$	reference
n-$InGaAs$ $Si > 5 \cdot 10^{18}$	$NiGeAu$	300 400	$1E^{-6}$ $4 \cdot 10^{-8}$	[108]
n-$GaAs$ Si $2 \cdot 10^{18}$	$TiPtAu$	no ann.	$5 \cdot 10^{-4}$	[111]
p-$GaAs$ Zn $5 \cdot 10^{18}$	$CrAu$	no ann. 430	$1 \cdot 10^{-4}$ $2 \cdot 10^{-5}$	[112]

Table 3.3: Summary of used contacts.

The lateral resistivity of a highly doped material increases with a factor of $ln(r_{con}/r_{ox})$ where r_{con} and r_{ox} are the aperture radii of the contact and the oxide aperture, as illustrated in figure 3.22 [89]. This means that the top-contact should have the same size as the oxide aperture in order to avoid highly resistive lateral carrier transport.

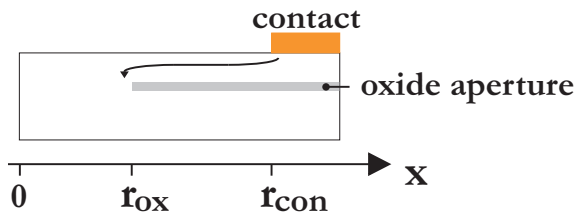

Figure 3.22: The current flow from a top-contact around the oxidation-layer.

3.10 Group delay dispersion and gain bandwidth

A top mirror on the eVCA will increase the gain of the structure. However, the top mirror influences the group delay dispersion. The group delay *dispersion* (GDD) is defined as the second derivative of the phase delay, ϕ, with respect to the angular optical frequency, ω, i.e.

$$GDD = \frac{\partial^2 \phi}{\partial \omega^2} \tag{3.9}$$

and is measured in units of fs^2.

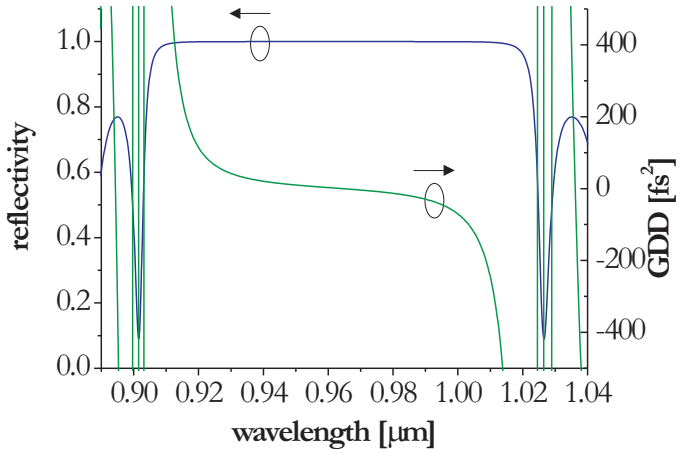

Figure 3.23: The reflectivity and group delay dispersion of a DBR with 30 pairs of $AlAs/GaAs$ designed for 960 nm.

The group delay dispersion and the reflectivity of a 30 layer $GaAs/AlAs$ DBR designed to 960 nm is calculated by use of a transfer matrix method and illustrated in figure 3.23. The reflectivity at the design wavelength is 0.9998, the GDD is around 20 fs^2 at 940 nm, and the slope of GDD around the design wavelength is ~ 1 fs^2/nm. The calculated reflectivity and dispersion is in accordance with a similar DBR designed at 1314 nm presented by Spühler et al. [69].

A top DBR grown on top of an eVCA will, assuming the entire structure is designed to be *resonant*, enhance the optical field around the quantum wells, as the field reflected by the top DBR back into the structure is in phase with the field reflected by the bottom DBR. In a resonant structure,

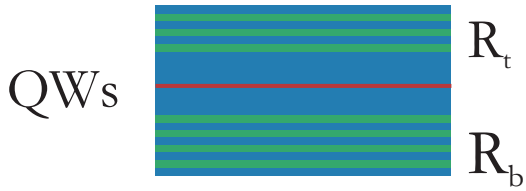

Figure 3.24: A sketch of the eVCA simulated in this section. The bottom DBR, R_b, has 30 pairs of $GaAs/AlAs$ with a reflectivity of ~ 0.9998. The active region consists of three 8-nm $In_{0.165}Ga_{0.825}As$ quantum wells with $Al_{0.15}Ga_{0.85}As$ barriers, and the wells are positioned in the antinode of the optical field intensity. The top DBR, R_t, consists of pairs of $GaAs/AlAs$.

the top and bottom DBRs form a cavity with a higher net reflectivity at the design wavelength. However, the top mirror will also induce a smaller bandwidth and a larger GDD and GDD-slope around the design wavelength.

A sketch of an eVCA with a top DBR with reflectivity R_t is illustrated in figure 3.24. The FWHM bandwidth, maximum reflectivity and the GDD and GDD-slope of a structure similar to this has been calculated using the transfer matrix model. The bottom DBR has 30 pairs of $GaAs/AlAs$ layers with a reflectivity of $R_b \simeq 0.9998$. The active region consists of three 8-nm $In_{0.165}Ga_{0.825}As$ quantum wells with 10-nm $Al_{0.15}Ga_{0.85}As$ barriers. The gain coefficient in the quantum wells is assumed to be 2500 cm^{-1}. The top DBR consist of 4.5 pairs of $GaAs/AlAs$ layers. Since the first and last layer in this DBR is $GaAs$, the top DBR consists of a half-integer number of DBR pairs. No substrate is included in this structure, and the top surface of the eVCA is not AR-coated, the total reflection of the top DBR is thus the reflection of the DBR *and* the reflection of the air/$GaAs$ interface. The layers of the structure are doped with typical doping levels, and the free-carrier absorption connected with the doping is included in the calculations. The structure is equal to the TAIWAN structure described in detail in section 4.1.2, except that the TAIWAN structure has an AR-coated substrate on top of the top DBR.

The refractive index and the optical field intensity of this structure is shown in top graph of figure 3.25. The bottom graph shows the reflectivity and the GDD of the structure. The maximum reflectivity of this eVCA is 1.36, i.e. a gain of 36 %, the FWHM bandwidth of the reflectivity is

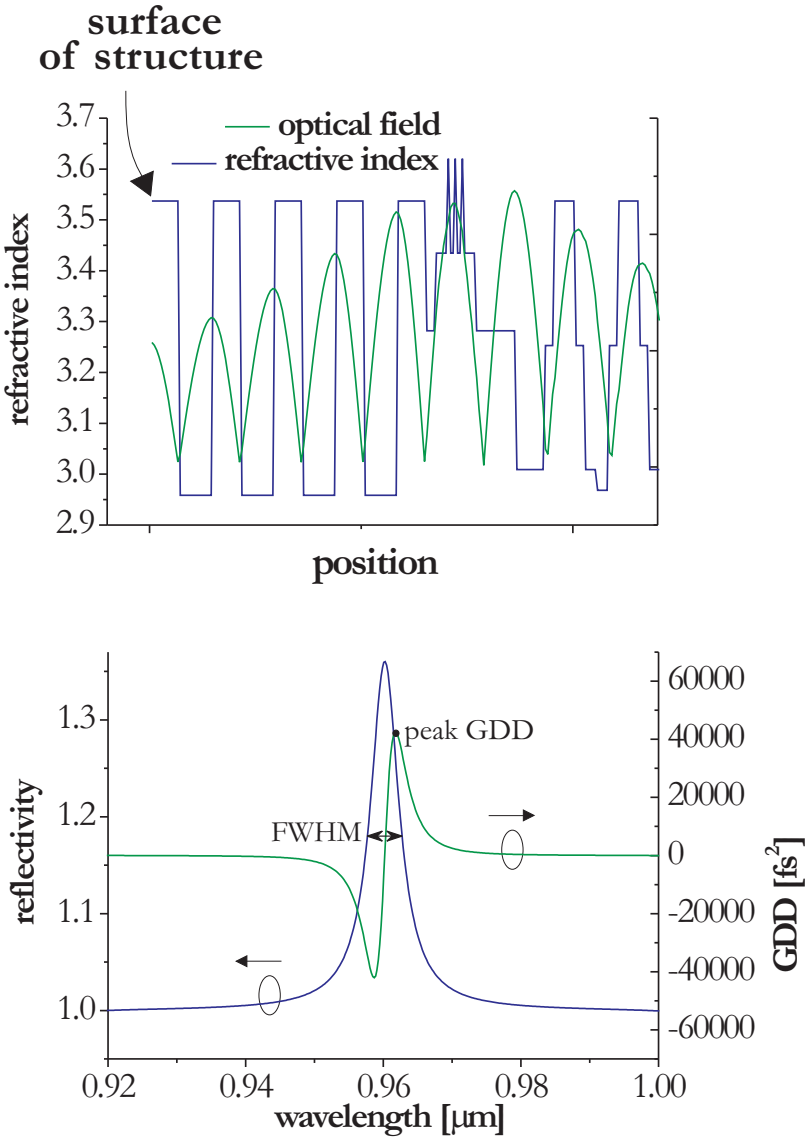

Figure 3.25: Top: The refractive index (blue line) and the optical field intensity (green line) of the above structure with 4.5 pairs of top DBR. Bottom: The reflectivity and group delay dispersion of the same eVCA. The gain coefficient in the three 8 nm quantum wells is set to 2500 cm^{-1} and the number of top DBR pair is 4.5.

4.4 nm (corresponding to 1.4 THz), the peak GDD is 42551 fs^2 (located at $\sim$ 962 nm) and the GDD slope is 28339 fs^2/nm.

In order to illustrate how the above parameters depend on the number of pairs in the top DBR $GaAs/AlAs$, similar calculations have been performed on the same structure with a varying number of top DBR pairs from 0.5 (corresponding to a single $\lambda_B/4$ layer of $GaAs$) to 6.5. The total reflectivity of the top DBR versus the number of $AlAs/GaAs$ pairs is shown in figure 3.26. The total reflectivity increases from 0.31 to 0.88.

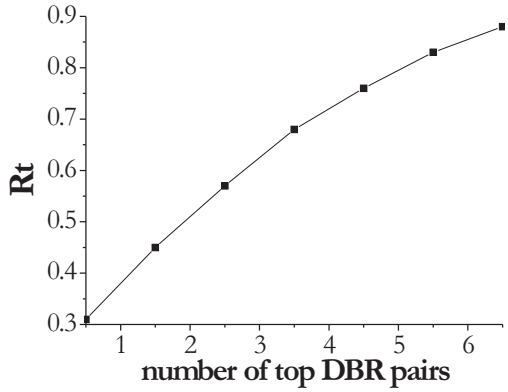

Figure 3.26: The total reflectevity of the un-coated top DBR, R_t, versus the number of $GaAs/AlAs$ pairs in the DBR.

The calculations have been performed with three different gain coefficients in the quantum wells; **a** $g = 2000\ cm^{-1}$, **b** $g = 2500\ cm^{-1}$, **c** $g = 3000\ cm^{-1}$. The results are shown in figure 3.27 which shows the FWHM bandwidth, the maximum reflectivity, the peak GDD and slope of GDD of the structure as the number of pairs in the top BDR is increased.

The calculations have similarly been performed on an AR-coated structure with a gain coefficient of $g = 2500\ cm^{-1}$ in the quantum wells. The results are shown in figure 3.28.

The variation of the FWHM bandwidth for a structure with 2.5 or more pairs of top DBR is very small as the gain coefficient is increased from 2000 cm^{-1} to 3000 cm^{-1}. For less than 2.5 pairs of top DBR, the difference of the bandwidth becomes more significant when the gain coefficient changes. The variation of GDD and GDD slope as the gain coefficient is increased is very small. The gain coefficient or the number of quantum wells can thus with advantage be increased without introducing larger GDD

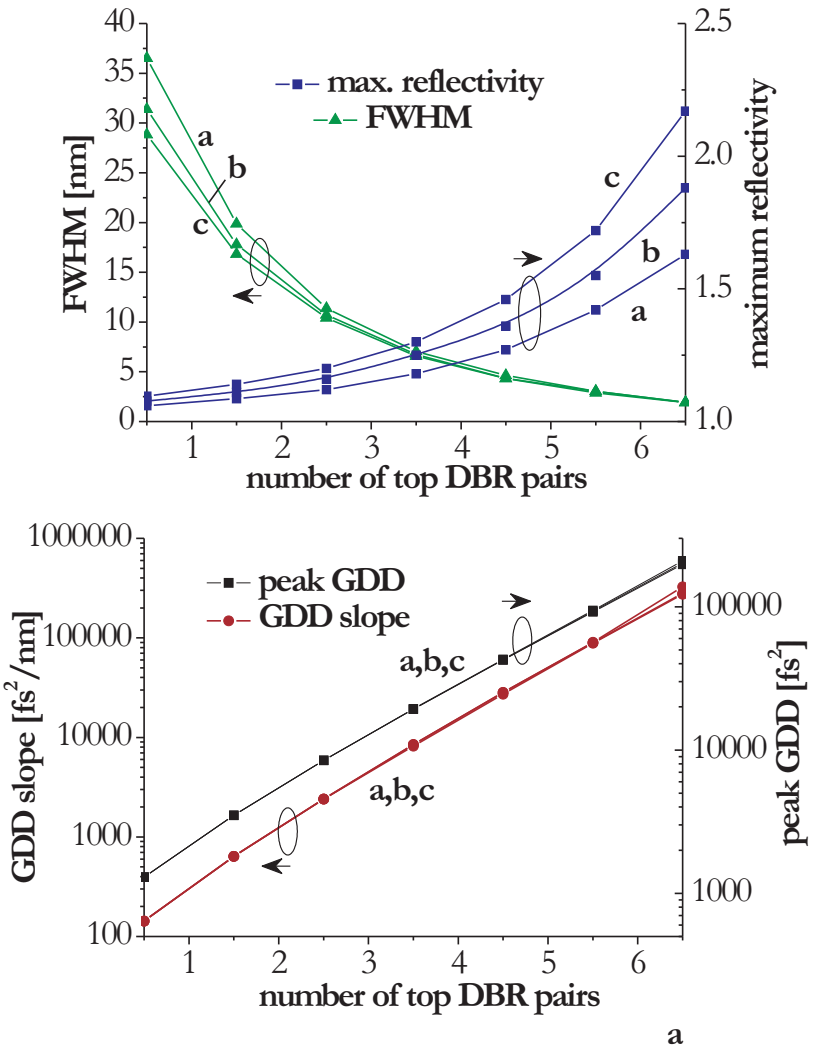

Figure 3.27: Top graph: The maximum reflectivity and the FWHM of a structure of figure 3.24 with 0.5 to 6.5 number of pairs in the $GaAs/AlAs$ top DBR. The gain coefficient in the quantum wells has been varied from 2000 cm^{-1} (**a**) to 2500 cm^{-1} (**b**) and 3000 cm^{-1} (**c**). Bottom graph: The group delay dispersion (GDD) and GDD slope of the same structure.

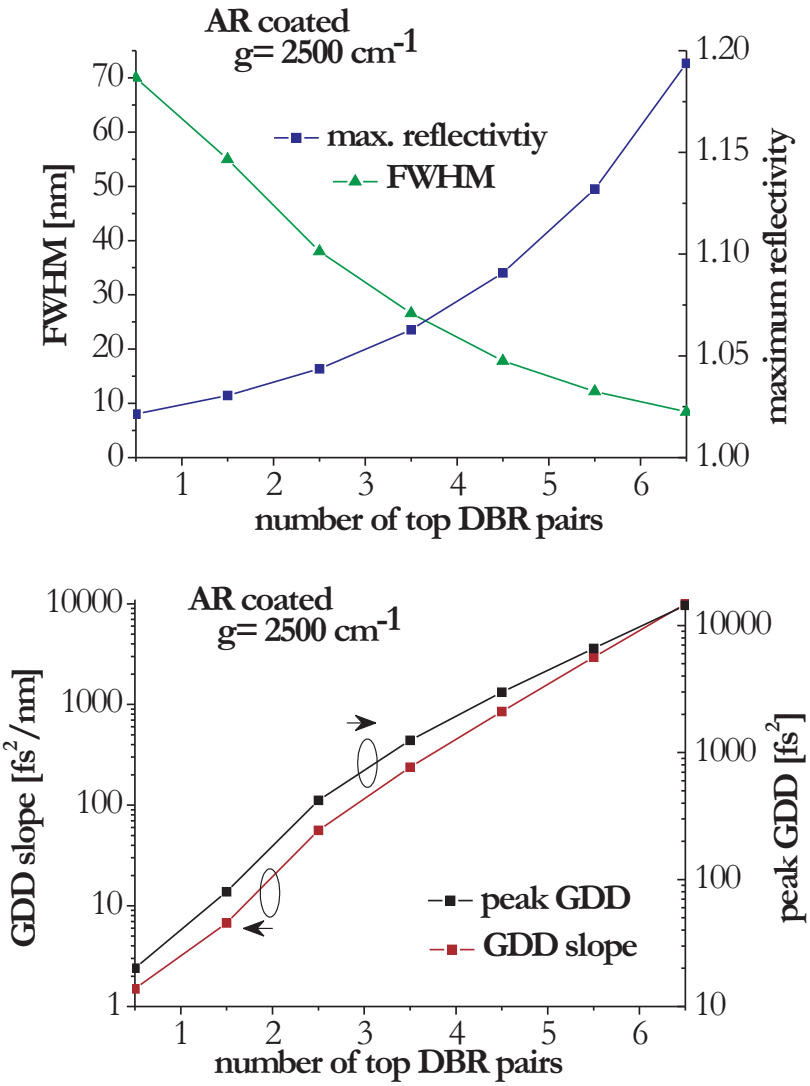

Figure 3.28: Top graph: The maximum reflectivity and the FWHM of an AR-coated structure of figure 3.24 with 0.5 to 6.5 number of pairs in the $GaAs/AlAs$ top DBR. The gain coefficient in the quantum wells is set to 2500 cm^{-1}. Bottom graph: The group delay dispersion (GDD) and GDD slope of the same structure.

or GDD slope.

As the top DBR reflectivity is increased from 0.31 to 0.88, the peak GDD increases from $\sim 1300\ fs^2$ to $\sim 210000\ fs^2$ and the GDD slope increases from $\sim 143\ fs^2/nm$ to $\sim 325000\ fs^2/nm$. The FWHM bandwidth decreases from $\sim 30\ nm$ to $\sim 2\ nm$. The net gain increases from 7.7 % to 88 % in the structure with a gain coefficient of $2500\ cm^{-1}$.

When the structure is AR-coated (figure 3.28), the FWHM slightly increases and the GDD and GDD slope slightly decreases, due to the effectively weaker top DBR reflectivity.

One way to avoid the high dispersion slope is to design the eVCA *anti*-resonant. An anti-resonant eVCA will have a lower net gain as the transmittance of the optical field at the design wavelength is smaller than in the resonant type. For the same reason, the anti-resonant eVCA has a very small GDD and GDD slope at the design wavelength.

The top graph of figure 3.29 shows the refractive index and optical field of an anti-resonant eVCA with 4 pairs of top DBR; the quantum well region, barriers and spacer layer materials are the same as in the resonant structure above. However, the top DBR has an integer number of $GaAs/AlAs$ pairs, as the first layer is $AlAs$ and the last layer (on the surface of the structure) is $GaAs$. This means that there is no cavity in the structure as is the case of the resonant eVCA. The bottom graph of figure 3.29 shows the reflectivity and the GDD for the AR-coated (dashed line) and un-coated (solid line) anti-resonant eVCA with a gain coefficient of $2500\ cm^{-1}$. The table 3.4 lists the reflectivities, GDD and GDD slope at the design wavelength.

The reflectivity at the design wavelength is 1.0014 for the un-coated and 1.0051 for the AR-coated anti-resonant eVCA with 4 pairs op top DBR, compared to the reflectivity of the resonant structure with same gain coefficient of ~ 1.36. The reflectivity of the anti-resonant structure slightly increases when an AR-coating is added, due to the smaller effective reflectivity of an AR-coated top DBR compared to an un-coated top DBR. The gain bandwidth in the anti-resonant structure is limited by the bandwidth of the DBRs. By calculating the optical field in the structure at a wavelength of $925\ nm$ it becomes clear that this anti-resonant structure is resonant at around $925\ nm$. This is also why the reflectivity is largest at $925\ nm$. There would thus be a fairly good chance that this eVCA would lase at $925\ nm$ in an VECSEL, depending on the gain coefficient at $925\ nm$, unless the lasing wavelength of the VECSEL is controlled elsewhere in the cavity. The GDD and GDD slope of this device at $925\ nm$ is comparable with the GDD and GDD slope of the resonant device at the design wavelength.

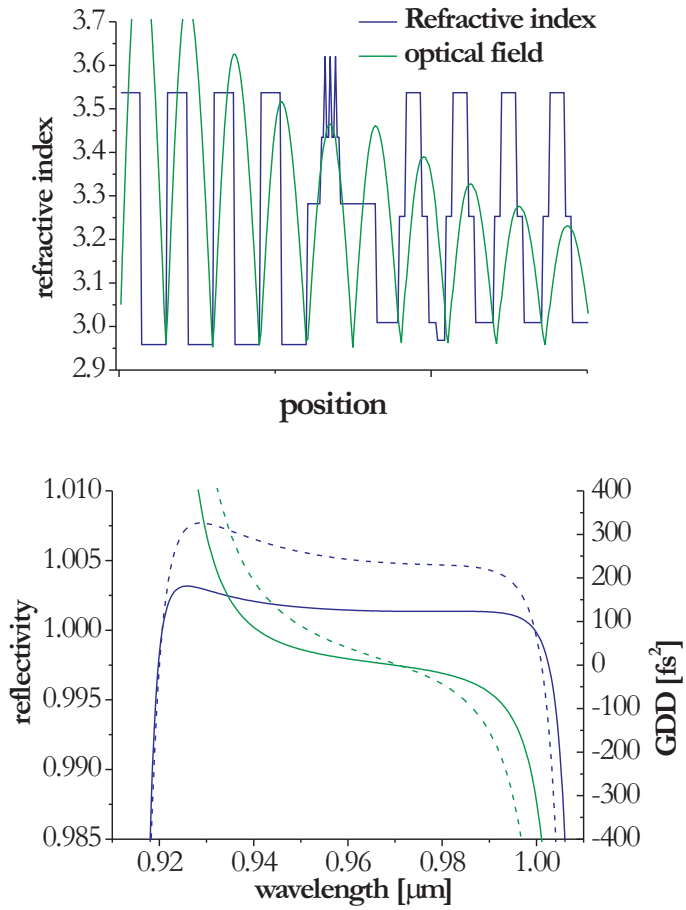

Figure 3.29: Top graph: The refractive index (blue curve) and optical field (green curve) in an anti-resonant eVCA structure. Bottom graph: The reflectivity and the GDD for the AR-coated (dashed line) and un-coated (solid line) anti-resonant eVCA with a gain coefficient of 2500 cm^{-1}.

3.11 Gain saturation

Another design-issue is the gain saturation of the eVCA; as mentioned earlier, a saturation of the gain section of a mode-locked laser closes the window of net gain after passage of the pulse. The saturation of the gain section is thus important for the pulse shaping. We have estimated the

anti-resonant eVCA	reflectivity ($\lambda = 960\ nm$)	GDD $[fs^2]$	GDD slope $[fs^2/nm]$
un-coated	1.0014	87	1.75
AR-coated	1.0051	193	4.5

Table 3.4: Reflectivity, GDD and GDD slope around the design wavelength of the anti-resonant eVCA with a gain coefficient of 2500 cm^{-1} in the quantum wells.

gain saturation of an eVCA in two limits; the CW limit and in the pulse limit. If the eVCA is operated in either a CW laser cavity or a mode-locked laser cavity where the pulse duration is long or the round trip time is short compared to the gain recovery time, the saturation of the eVCA can be calculated using a CW approach. If the eVCA is operated in a mode-locked laser with short pulse durations or large round trip time compared with the gain recovery time, the saturation of the gain should be estimated using the pulse approach.

In the CW approach, the change of the total gain of a structure is calculated versus an external CW signal power. In the pulse approach, the pulse energy that reduces the total gain of a structure by 10 % is calculated.

The calculations of the gain saturation does not take into account lateral current density inhomogeneities or the lateral dependency of the mode-beam intensity. The effect on the gain saturation energy due to these factors requires a more thorough analysis.

3.11.1 CW approach

An increase of the top DBR reflectivity of a resonant structure leads to a decrease in the power needed to saturate the structure due to the enhancement of the optical field around the quantum wells.

The gain saturation of the structure has been calculated by a set of modified rate equations that are valid for Fabry-Perot optical amplifiers below threshold [113–115]. The rate equations include a mirror loss, α_m, which makes the model valid for devices with highly reflective mirrors such as vertical-cavity semiconductor optical amplifiers (VCSOAs); in these devices, the carrier density is reduced due to an enhancement of stimulated emission close to threshold or at high external input powers. The model is also described in detail in appendix B.

The rate equations express the change of the carrier density, dN/dt, in the active region and the photon density, dS/dt, in the structure, both in units of $s^{-1}cm^{-3}$:

$$\begin{aligned} \frac{dN}{dt} &= G_{gen} - R_{st} - R_{nr} \\ &= \frac{\eta_i I}{qV_a} - \Gamma v_g g S - (AN + BN^2 + CN^3) \end{aligned} \tag{3.10}$$

$$\begin{aligned} \frac{dS}{dt} &= \frac{\delta S_{ext}}{\delta t} + R_{sp} + R_{st} - R_{loss} \\ &= \frac{P_{ext}}{h\nu_{ext} V_{eff}} + \beta\Gamma_{QW} B N^2 + \Gamma\Gamma_{QW} g v_g S - (\alpha_i + \alpha_m) v_g S \end{aligned} \tag{3.11}$$

G_{gen} is equal to the generated carriers per second per volume via the current-injection, I, and injection efficiency, η_i, in the active volume V_a. The second term in equation 3.10 expresses the stimulated recombination and is proportional to the product of the photon density, S, the gain coefficient per unit length, g, the group velocity, v_g, and the confinement factor, Γ. The third term is a sum of recombinations that do not contribute to the gain in the device expressed by the A, B and C coefficients (defect recombination coefficient, bimolecular recombination coefficient and Auger recombination coefficient).

$\delta S_{ext}/\delta t$ is the density of photons with energy $h\nu_{ext}$ added per second to the effective volume of the structure, V_{eff}, by the external input signal with a power of P_{ext}. The second and third terms in equation 3.11 express the spontaneous and stimulated recombinations where the confinement factor Γ_{QW} has been added which is equal to the length of the active material divided by the total effective length of the structure, L_a/L_{eff}. The effective length of the structure, L_{eff}, is the length of the cavity *plus* the penetration depth into the BDRs, which for a DBR with reflectivity R at the design wavelength λ_B and refractive index difference of Δn is equal to $\sqrt{R}\lambda_B/4\Delta n$ [5]. Furthermore, the spontaneous recombination is proportional to the spontaneous emission factor, β.

The fourth term in equation 3.11 is the sum of mirror loss and internal loss, denoted by the absorption coefficients α_m and α_i respectively. The internal loss is the average free carrier loss in the effective structure length and can be estimated on the basis of equation 3.5 on page 46.

The above-mentioned mirror loss is a cavity-related loss and equal to [113]

$$\alpha_m = \frac{1}{L_{eff}} \frac{G}{G-1} ln[G_s] \tag{3.12}$$

where G is the total gain of the structure and equal to

$$G = 1 + \frac{(1 - R_t)(1 + R_b G_s)(G_s - 1)}{(1 - \sqrt{R_t R_b} G_s)^2 + 4\sqrt{R_t R_b} G_s sin^2(\varphi)} \tag{3.13}$$

R_t and R_b are the top and bottom DBR reflectivities, φ is the detuning of the optical wavelength and equal to 0 at the Bragg wavelength, and the single pass gain, G_s of the structure is equal to

$$G_s = e^{(\Gamma g L_a - \alpha_i L_{eff})} \tag{3.14}$$

g is the gain coefficient of the quantum well and it expressed by a first-order approximation [60]:

$$g = g_0 ln(\frac{N}{N_{tr}}) \tag{3.15}$$

where N_{tr} is the carrier density at transparency and g_0 is a fitting parameter.

The rate equations are solved with respect to the carrier density, N, in a steady state condition, i.e. $dS/dt = dN/dt = 0$, for different external signal powers, P_{ext}. The single pass gain of the structure is then calculated by equation 3.14, and finally, the total reflection of the structure with a single-pass gain of G_s is expressed by [113]

$$R_G = \frac{(\sqrt{R_t} - \sqrt{R_b} G_s)^2 + 4\sqrt{R_t R_b} G_s sin^2(\varphi)}{(1 - \sqrt{R_t R_b} G_s)^2 + 4\sqrt{R_t R_b} G_s sin^2(\varphi)} \tag{3.16}$$

The total reflection of the structure is calculated at different external signal powers, P_{ext}, and the gain saturation is defined as the external signal power where the gain of the structure, i.e. $R_G - 1$, is decreased to half its original value.

The gain saturation power has been calculated for the eVCA illustrated in figure 3.24 with 30 pairs of $GaAs/AlAs$ bottom DBR, three 8-nm $InGaAs$ quantum wells with $AlGaAs$ barriers and with a varying top mirror reflectivity, R_t, from 0 to 1. Again, as the structure is very similar to the TAIWAN structure, which is presented in detail in section 4.1.2, the parameters for the TAIWAN structures (table B.1 on page 158) has been used in these calculations except the gain coefficient of the quantum wells which is assumed to be $\sim 2500\ cm^{-1}$ (with a $g_0 = 1100\ cm^{-1}$) and the aperture diameter of the structure is 150 μm.

The result is shown in figure 3.30; as the top mirror reflectivity is increased from 0 to 1, the gain saturation power decreases from $\sim 1.8\ W$ to $\sim 7\ mW$. The maximum reflectivity increases from ~ 1 to ~ 1.8.

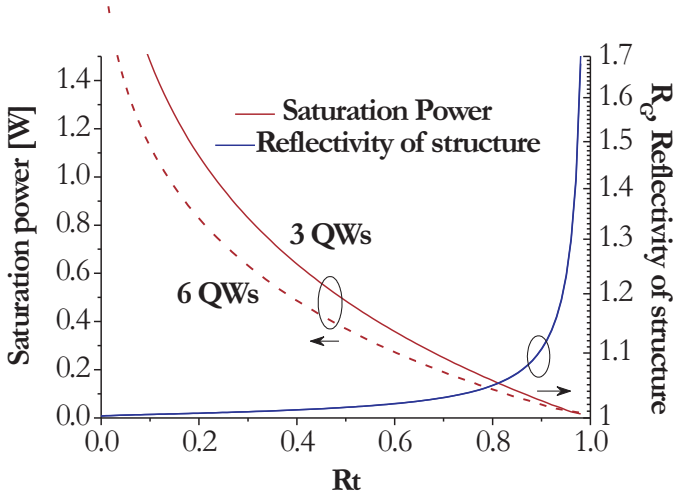

Figure 3.30: The reflectivity and saturation power of a structure with three quantum wells and six quantum wells. The bottom-mirror reflection is $\simeq 1$ and a top mirror reflection, R_t, varies from 0 to 1. The aperture diameter of the device is 150 μm.

The gain saturation power for a 6 quantum well device is also shown in this graph; the total thickness of the quantum wells is in this simulation doubled from 24 to 48 nm, and the injected current is changed so the reflectivity of the structure at small external signal powers is similar to the device with the 3 quantum wells. At a fixed reflectivity, R_G, the 6 quantum well device has a lower carrier density in the quantum wells compared with the 3 quantum well device, and as the differential gain is larger at lower carrier densities, the gain saturation power decreases.

However, the 6 quantum well device has a larger reflectivity than the 3 quantum well device at a constant carrier density. Therefore, a 6 quantum well device requires a weaker top mirror reflectivity in order to obtain same reflectivity as the 3 quantum well device, and this would decrease the gain saturation power of the device.

The top graph of figure 3.31 shows the gain saturation power and reflectivity versus the injected current in the 3-quantum well eVCA. The eVCA reaches a reflectivity of 1 at ~ 65 mA, and increases to 1.048 as the current is increased to ~ 118 mA. The gain saturation power increases from ~ 9.4 mW to ~ 0.52 W in the same range.

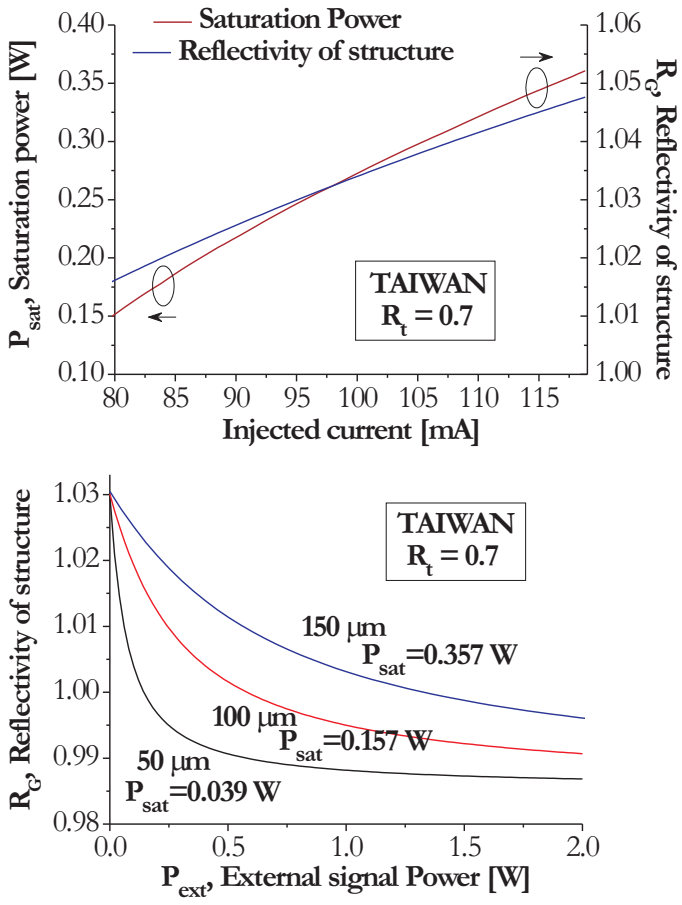

Figure 3.31: Top graph: The reflectivity and saturation power versus the injected current, I, for the structure described in the text with three quantum wells. The aperture diameter is 150 μm. Bottom graph: The reflectivity of the same structure with a top DBR reflectivity of 0.7 versus the external signal power calculated at three different aperture diameters, 50 μm (black curve), 100 μm (red curve) and 150 μm (blue curve).

The bottom graph of figure 3.31 shows the reflectivity of the same 3-quantum well eVCA versus the external signal power with three different aperture diameters, 50 μm (black curve), 100 μm (red curve) and 150 μm (blue curve). The injected current has been adjusted in order to reach

the same reflectivity at small external signal powers. The gain saturation power is noted to each graph. The gain saturation power decreases as the the aperture diameter decreases, due the the larger fluence (in units of W/cm^2) of the external signal power on eVCAs with small apertures. The gain saturation fluence of this 3 quantum well device is $\sim 2\ kW/cm^2$. For convenience, the gain saturation *fluence* of the same 3-quantum well structure with varying top mirror reflectivity, R_t, is shown in figure 3.32.

The calculations above show how the reflectivity of the top DBR and the external mirror influences the gain saturation of the eVCA. The top DBR reflectivity of an eVCA should be strong enough to ensure net gain of the structure and can furthermore be adjusted so as the eVCA has a gain saturation power that fit with the absorber saturation power in the mode-locked laser.

For a certain eVCA structure, the gain saturation power of the eVCA can be adjusted by the reflectivity of the external cavity mirror. A highly reflecting external mirror requires a low injection current in the eVCA in order to reach lasing of the cavity. The low injection current leads to a low saturation power of the eVCA. In addition, a highly reflecting external mirror ensures a high intra-cavity power which again enhances the saturation the eVCA. A weak reflecting external mirror requires a higher injection current in the eVCA which leads to a higher saturation power of the eVCA. A weak reflecting external mirror also gives a lower intra-cavity power which decreases the chances of saturating the eVCA. The external mirror loss plays in this manner an important role in the dynamics of the gain medium in the mode-locked laser cavity.

3.11.2 Pulse approach

In the previous sub-section, the CW saturation of the eVCAs based on steady state rate equations was calculated. This section treats the saturation of the gain in an eVCA during the passage of an intense pulse, as illustrated in figure 3.33. The gain of the structure the moment before the pulse arrives is g_i and after passage of the pulse the gain of the structure has decreased by δg.

The change of gain coefficient, $\delta g/\delta t$ in the active area of a travelling wave amplifier can be expressed by [116]

$$\frac{\delta g}{\delta t} = \frac{g_i - g}{\tau_g} - \frac{gI}{E_{sat}} \tag{3.17}$$

where g_i is the small signal gain coefficient, τ_g is the gain recovery time and I the intensity of the pulse. E_{sat} is the pulse energy where the gain is

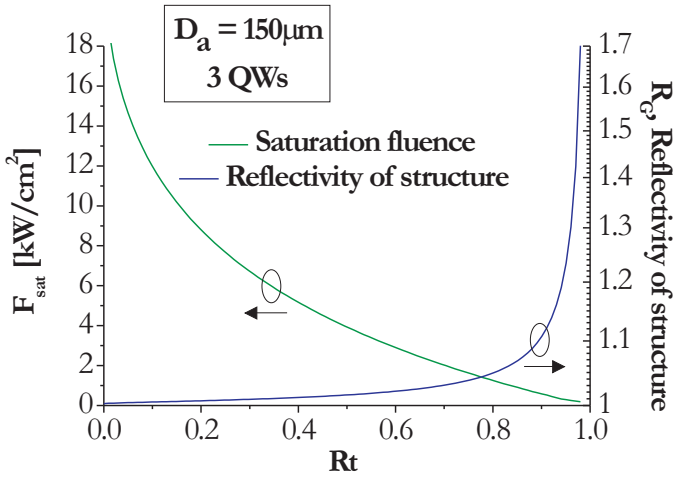

Figure 3.32: The gain saturation fluence in units of kW/cm^2 for a three quantum well structure with an aperture diameter of 150 μm and with varying top DBR reflectivity, R_t.

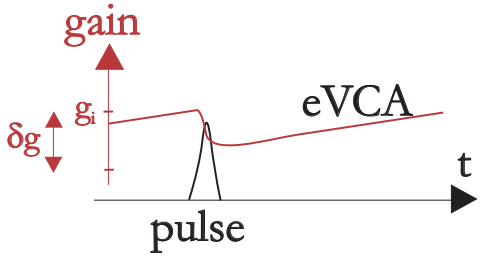

Figure 3.33: The saturation of the gain in the eVCA.

heavily saturated and is equal to

$$E_{sat} = \frac{\hbar\omega\sigma}{a_g} \tag{3.18}$$

σ is the cross-section of the optical mode onto the gain medium and $\hbar\omega$ the photon energy of the pulse. In the above equation, the gain coefficient is assumed to increase linearly with the carrier density, N, i.e. $g \propto a_g(N - N_{tr})$ where a_g is the differential gain.

Since an eVCA is not a single pass travelling-wave amplifier and the quantum wells are incorporated into a larger structure we will estimate the saturation of the total gain of the structure and not the saturation of the gain coefficient of the quantum wells. The total reflection, R_G, of a resonant eVCA with top mirror reflectivity R_t and bottom mirror reflectivity R_b and a single pass gain of G_s is expressed by equation 3.16 from the previous section. The single-pass gain is equal to $G_s(g) = e^{(\Gamma g(N) L_a - \alpha_i L_{eff})}$ where L_{eff} is the effective length of the eVCA, L_a is the total thickness of the quantum wells and α_i is the internal absorption coefficient in the eVCA and $g(N)$ the gain coefficient of the quantum wells and Γ the confinement factor.

The change in carrier density caused by a pulse of energy E_{sat} with photon energy of $\hbar\omega$ in the active volume is equal to

$$\delta N = \frac{E_{sat}}{\hbar\omega A_a L_a}(R_G - 1) \tag{3.19}$$

where A_a is the aperture area of the eVCA. The change in the gain coefficient, δg, due to this change in carrier density caused by the pulse depends on the amount of carriers in the quantum wells, which is clear from equation 3.15. At a starting carrier density of N_0, we can write the condition where the eVCA is saturated by 10 % as

$$R_G(G_s(g(N_0 - \delta N))) = 0.9 R_G(G_s(g(N_0))) \tag{3.20}$$

The above equation is solved numerically and we denote $E_{sat,0.9}$ the pulse energy where the above equation is fulfilled. $E_{sat,0.9}$ is presented in the top graph of figure 3.34 for three eVCAs with top DBR reflectivities of $R_t = 0.6$, 0.7 and 0.8. All three eVCAs have an aperture diameter D_a of 150 μm.

When N_0 is increased, the differential total reflectivity of the structure, $|\delta R_G/\delta N|_{N=N_0}$, decreases. Although δN also increases through the increase of R_G (equation 3.19) the change of the differential total reflectivity is the dominating effect, and $E_{sat,0.9}$ is found to increase with N_0 and thus R_G.

At high carrier densities, the differential reflectivity $\delta R_G/\delta N$ goes to zero and $E_{sat,0.9}$ will thus go to infinity. Close to transparency, the simulations will break down due to the fact that R_G becomes smaller than 1 and δN according to equation 3.19 also smaller than one. The presented curves are thus calculated gain saturation pulse energies for carrier densities N_0 well above transparency.

The three points on the three curves mark the situation where the gain coefficient, determined by $g = g_0 ln(N_0/N_{tr})$, is equal to **a** 2000 cm^{-1}, **b** 2500 cm^{-1}, and **c** 3000 cm^{-1}.

For the structure with a top mirror reflectivity of 0.7, the gain saturation pulse energy increases from ~ 1.5 nJ to ~ 10 nJ as the total reflectivity of the structure increases from 1.1 to 1.65. As with the CW saturation power, the gain saturation energy of the eVCA can in this manner be adjusted by the external mirror loss. A gain saturation pulse energy of ~ 1.5 nJ means that the intra-cavity power of a mode-locked laser with a repetition rate of 1 GHz can be as high as 1.5 W.

The bottom graph of figure 3.34 shows the pulse energy *fluence* calculated for an eVCA with a gain coefficient of 2500 cm^{-1} and with varying top DBR reflectivity.

The required saturation of the gain depends on the saturation of the absorber. If the pulse fluence on the absorber is small or if the modulation depth, ΔR, is small, the gain saturation should also be small. Assuming that R_G is linear with the carrier density, N, $E_{sat,x}$ can be approximated by

$$E_{sat,x} \simeq E_{sat,0.9} \frac{1-x}{1-0.9} \tag{3.21}$$

The pulse energy it takes to saturate an eVCA structure with a gain coefficient of 2500 cm^{-1} and a top DBR reflectivity of 0.7 and with an aperture of 150 μm 1 %, i.e. $E_{sat,0.99}$, is equal to ~ 0.2 nJ.

3.12 Summary

eVCAs can either be designed as top-emitting structures, where light is emitted through the last-grown surface, or as bottom-emitting structures, where light is emitted through the substrate on which the structure has been grown. The bottom-emitting structures has advantages over the top-emitting structure in a better removal of the heat generated in the structure and a better lateral current spreading allowing for larger apertures in the bottom-emitting eVCAs.

The structure can either be designed resonant or anti-resonant; a resonant design has a much better enhancement of the gain in the quantum wells but also a smaller gain bandwidth and a larger group delay dispersion than the anti-resonant structure.

The eVCA should be designed with as low resistivity as possible to minimise the heating of the structure. A low resistivity is ensured by n-

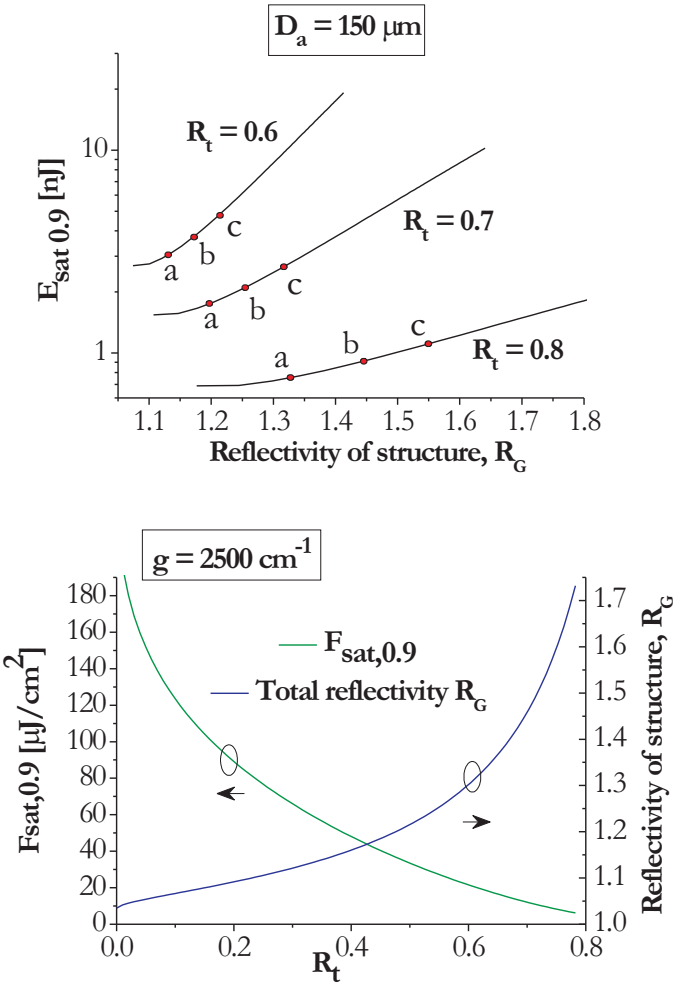

Figure 3.34: Top graph: The pulse saturation energy where the total gain of an eVCA has decreased by 10 % versus the total reflectivity of three eVCAs with top DBR reflectivities $R_t = 0.6$, 0.7 and 0.8. All three eVCAs have an aperture diameter of 150 μm. The three points on the three curves mark the situation where the gain coefficient in the quantum wells is $g = 2000$ (**a**), 2500 (**b**) and 3000 cm^{-1} (**c**). Bottom graph: The pulse energy fluence calculated for an eVCA with a gain coefficient of 2500 cm^{-1}.

and p-doping of the structure. The doping should, however, be restricted to areas with a low optical field intensity in the structure in order to reduce free-carrier absorption.

DBRs with low resistivity can be obtained with simple composition and doping gradings at the interfaces of the DBR. The p-doped DBR should preferably consist of pairs of $GaAs/AlGaAs$ in order to minimise the resistivity of the p-doped DBR. An $GaAs/AlGaAs$ p-doped DBR also enhances the doping of the DBR when Be is used as p-dopant. Since electrons have a much higher mobility than holes, the n-doped DBR can consist of $GaAs/AlAs$.

Simulations show that the carrier density and thus the gain coefficient in $InGaAs$ quantum wells with $AlGaAs$ barriers is larger than in $InGaAs$ quantum wells with $GaAs$ or $GaAsP$ barriers. However, due to the strain in the $InGaAs/AlGaAs$ design, only 3 quantum wells can be grown using these materials, whereas up to 9 quantum wells can be grown in the strain-compensated $InGaAs/GaAsP$ design. In growth facilities where $GaAsP$ is available, a design based on up to 9 $InGaAs$ quantum wells, $AlGaAs$ barriers *and* $GaAsP$ spacer layers would be preferable. In growth facilities where $GaAsP$ is not available, 3 quantum wells of $InGaAs$ with $AlGaAs$ barriers is preferable.

The wavelength of the optical transition of the quantum wells should be designed slightly lower than the desired wavelength due to significant band gap shrinkage and band filling of the quantum wells.

A top DBR on the eVCA will increase the gain of the structure. The reflectivity of the top DBR of a resonant structure influences the group delay dispersion and the gain saturation of the eVCA, wherefore the number of top DBR pairs should be optimised with regards to the other elements in the external-cavity mode-locked laser.

The gain saturation of an eVCA has been estimated in two limits; the CW limit and in the pulse limit. If the eVCA is operated in either a CW laser cavity or a mode-locked laser cavity where the pulse duration is long or the round trip time is short compared to the gain recovery time, the saturation of the eVCA can be calculated using a CW approach. If the eVCA is operated in a mode-locked laser with short pulse durations or large round trip time compared with the gain recovery time, the saturation of the gain should be estimated using the pulse approach.

The power or energy required to saturate the eVCA decreases with increased reflectivity of the top DBR. This means that an eVCA with a weak top DBR reflectivity that is operating in an external cavity allows higher intra-cavity powers than an eVCA with a strong top DBR reflectivity.

Chapter 4

Fabrication and processing of eVCA

4.1 Type of eVCAs in this report

This thesis deals with four different eVCA designs, one top-emitting and three bottom-emitting. The four types of eVCAs have been grown at four different places. The IQE eVCA was grown at IQE, Cardiff, Wales, it was a first shot eVCA structure. In designing the IQE eVCA, we decided to stick to a conventional VCSEL structure, with as few changes as possible.

The ORC eVCA was grown by the Optoelectronic Research Center, Tampere University of Technology, Finland. It was grown with a view to start up a cooperation, unfortunately the wafer turned out not to work. The ORC eVCA was the first bottom-emitting structure designed and processed at COM · DTU.

The TAIWAN eVCA was bought from LandMark Optoelectronics Corporation, Taiwan. This structure is also a bottom-emitting structure and very similar to the ORC wafer, except for the quantum well region.

The NBI eVCA was grown by Claus. B. Sørensen from the Nanophysics group at the Niels Bohr Institute, University of Copenhagen. This eVCA design is the first bottom-emitting structure designed at COM · DTU with etch-stop layers with a view to etch away the substrate.

Table 4.1, 4.2 and 4.3 list the designs of the four different structures. R_0 and R are the calculated reflectivities of the structures with a gain coefficient of $g = 0$ and $g = 2000\ cm^{-1}$ respectively.

The next sections give a short introduction to each of the four types of eVCAs and section 4.2 presents the clean room processing of the eVCAs.

eVCA name	R_0 at design-λ	R at design-λ at $g = 2000cm^{-1}$	FWHM $[nm]$	peak GDD $[fs^2]$	GDD slope $[fs^2/nm]$
IQE*	0.9979	1.065	71	118	5.9
ORC*	0.7873	1.828	2.4	120004	92310
TAIWAN*	0.9372	1.005	3.9	4620	1144
NBI*	0.9928	1.020	86	125	4.3
NBI	0.9979	1.070	20.6	2929	741

Table 4.1: Designs of the four different eVCAs. R_0 and R are the reflectivities at the design wavelength with a gain coefficient of $g = 0$ and $g = 2000cm^{-1}$ respectively. Due to wrong growth of the TAIWAN design, it has a reflectivity of 0.9609 at 960 nm, the values listed for this eVCA in the table are all at 975 nm, at which wavelength the reflectivity is at maximum. The group delay dispersion is calculated by equation 3.9. In the bottom-emitting ORC and TAIWAN structures, substrate thicknesses of 80 μm and 50 μm respectively are assumed, both substrates with an absorption coefficient of 6 cm^{-1}. * = antireflection coated.

	name	IQE	ORC
	type	top-emitting	bottom-emitting
	no. of QWs	9	9
	design λ $[nm]$	980	980
well	t, material	9 nm, $In_{0.17}Ga_{0.83}As$	8 nm, $In_{0.17}Ga_{0.83}As$
barrier	t, material	12.39 nm, $GaAs_{0.75}P_{0.25}$	10 nm, $GaAs$
bottom DBR	material	$AlAs/GaAs$	$Al_{0.70}Ga_{0.30}As/GaAs$
	R [%]	99.9	98
top DBR	material	none	$AlAs/GaAs$
	R [%]	-	90

Table 4.2: The IQE and ORC eVCAs. t is the thickness of the quantum wells.

	name	TAIWAN	NBI
	type	bottom-emitting	bottom-emitting
	no. of QWs	3	3
	design λ [nm]	960	960
well	t, material	8 nm, $In_{0.165}Ga_{0.835}As$	8 nm, $In_{0.175}Ga_{0.825}As$
barrier	t, material	10 nm, $Al_{0.15}Ga_{0.85}As$	10 nm, $Al_{0.15}Ga_{0.85}As$
bottom DBR	material	$AlAs/GaAs$	$AlAs/GaAs$
	R [%]	99.99	99.9
top DBR	material	$AlAs/GaAs$	none
	R [%]	70	-

Table 4.3: The TAIWAN and NBI eVCAs. t is the thickness of the quantum wells.

4.1.1 Top-emitting structure, the IQE wafer

An outline of the IQE eVCA is shown in top of figure 3.2. The light is emitted upward through the last-grown layer. The top graph of figure 4.1 shows the refractive index (blue line) and the calculated optical field intensity (red line) in the IQE eVCA. The bottom graph shows the reflectivity (blue line) and group delay dispersion (green line) of the design.

This device is quite similar to a half VCSEL, *i.e.* a VCSEL without a top mirror. The epitaxial layer is grown on n-type substrate meaning that the bottom DBR is n-type.

The nine 9-nm $In_{0.17}Ga_{0.83}As$ quantum wells are positioned in groups of three in every antinode in the intrinsic region, which ensures a confinement

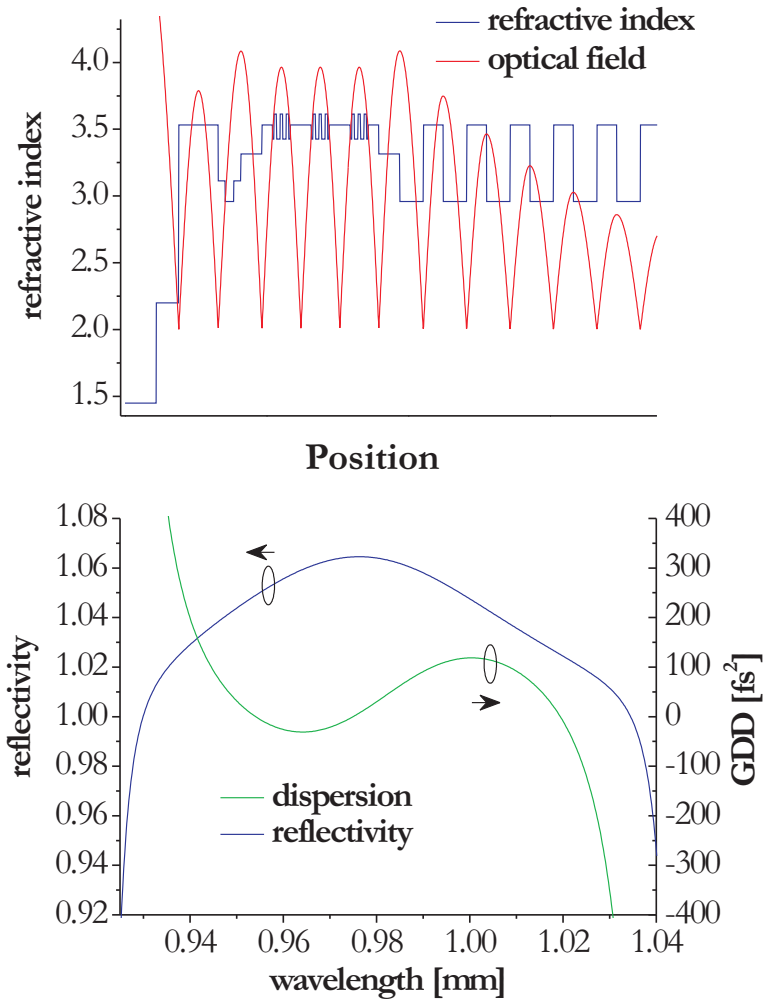

Figure 4.1: Top: The refractive index (blue line) and optical field (red line) of IQE structure, Bottom: reflectivity (blue) and dispersion (green) of the structure. The curves are calculated with a gain coefficient of 2000 cm^{-1} in the nine quantum wells, and the structure is AR-coated.

factor of $\Gamma \simeq 1.7$ (see appendix B). It is designed with 12 nm $GaAs_{0.75}P_{0.25}$ barriers in order to compensate the strain. The quantum wells are designed to have a photoluminescence at around 980 nm. The eVCA is equipped with an oxidation layer on the p-side of the structure close to the quantum

wells, which provides a high current density around the gain section. This aperture consists of a thin (30 nm) layer of $AlAs$ that has been oxidised to form an insulating ring shaped layer. On top of the oxide aperture, a highly doped $GaAs$ cap layer of $\simeq 200$ nm ensures good contacting to the p-type contact. The p-contact is a un-annealed Cr/Au contact and the n-contact is an annealed $NiGeAu$ alloy.

There are no current spreading layers on the p-side of the structure. An AR-coating can be deposited on the top surface in order to avoid reflection from the first $GaAs$-air interface.

A growth recipe of this structure is found at page 178 in appendix D.

4.1.2 Bottom-emitting structure

ORC wafer

This wafer is MBE-grown and is designed very similarly to the structure to the right in figure 3.2. It has 20 pairs of p-doped $Al_{0.7}Ga_{0.30}As/GaAs$ DBR with a reflectivity of ~ 98 %. The idea was that a p-contact of pure Au on the back of the p-doped DBR should increase the reflectivity to around 100 %. The mirror has $1 \cdot 10^{19}$ cm^{-3} Be delta doping on the $Al_{0.70}Ga_{0.30}As/GaAs$ interfaces and composition superlattice gradings consisting of 20 nm ($10 \times [1$ nm GaAs + 1 nm $Al_{0.7}Ga_{0.30}As]$). The structure is equipped with a 30-nm $AlAs$ oxidation layer. The 9 $In_{0.17}Ga_{0.83}As$ quantum wells with $GaAs$ barriers are positioned in groups of 3 in the antinodes of the optical field intensity, and are designed to have a photoluminescence at around 980 nm. The top DBR consists of 7.5 pairs of n-doped (Si) $AlAs/GaAs$ corresponding to a reflectivity of ~ 90 %. The whole structure is grown on an n-doped ($2 \cdot 10^{18}$ cm^{-3} Si) $GaAs$ substrate.

As a pure Au p-contact was difficult to adhere on $GaAs$ (and especially on SiO_2), we needed to deposit 10 nm of Cr as a first layer, which unfortunately absorbs light at 980 nm. This means that the total reflectivity of the p-DBR is only ~ 97.5 %. The p-contact was left un-annealed and the n-contact is an un-annealed $NiGeAu$ alloy.

The refractive index (blue line) and the calculated optical field (red line) in the ORC eVCA are shown in the top graph of figure 4.2. The bottom graph shows the reflectivity (blue line) and group delay dispersion (green line) of the design.

A growth recipe of this structure is found on page 179 in appendix D.

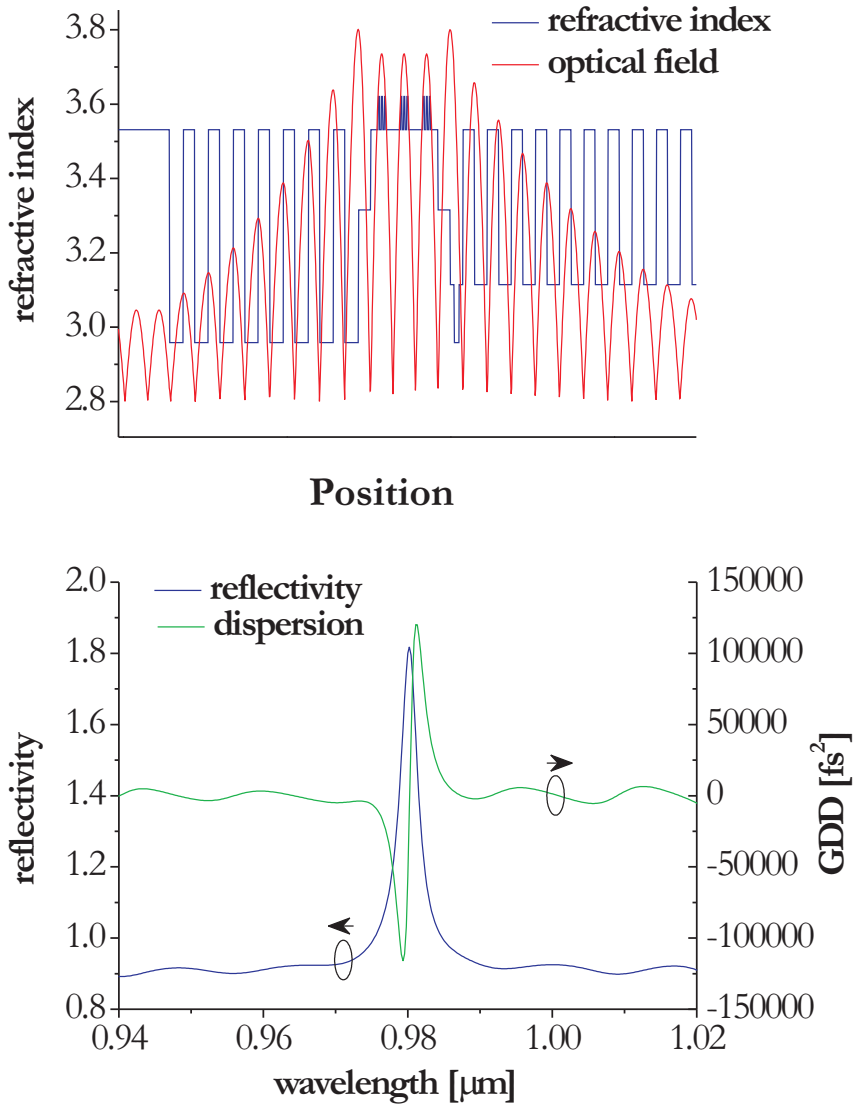

Figure 4.2: Left: refractive index (blue) and optical field (red) in the ORC design. Right: The reflectivity (blue) and dispersion (green) in units of fs^2 of the ORC design. The curves are calculated with a gain coefficient of 2000 cm^{-1} and the structure is AR-coated.

TAIWAN wafer

The TAIWAN wafer was designed somewhat similarly to the ORC wafer except that it has 30 layers of $Al_{0.9}Ga_{0.10}As/GaAs$ p-doped DBR (C doping) with a reflectivity of ~ 99.99 %. The $Al_{0.90}Ga_{0.10}As/GaAs$ interfaces are doped more heavily than the $GaAs/Al_{0.90}Ga_{0.10}As$ interfaces. The p-DBR has 20 nm composition graded interfaces but no doping gradings. As the ORC wafer, the TAIWAN wafer is equipped with a 30 nm $AlAs$ oxidation layer on the p-side.

The quantum well and barrier design of the TAIWAN eVCA is based on the $SILVACO$ simulations of the distribution of carriers in the quantum wells presented in section 3.4. It has three 8-nm $In_{0.165}Ga_{0.835}As$ quantum wells positioned in the antinode of the optical field and 10 nm $Al_{0.15}Ga_{0.85}As$ barriers. The quantum wells are designed to have a photoluminescence at 960 nm.

On top of the active region, 4.5 pairs of $AlAs/GaAs$ n-doped (Si) DBR has been grown. The whole structure is grown on a $2 \cdot 10^{18}$ cm^{-3} Si-doped $GaAs$ substrate.

From experience with lapping of the ORC wafer, we knew that it was fairly easy to lap and polish the substrate to a total thickness of ~ 50 μm, which is one of the reasons the number of n-DBR pairs in this design was only 4.5 compared to 7.5 in the ORC design.

Both the n and p-contact are un-annealed $TiPtAu$ contacts.

Figure 4.3 shows the refractive index (blue line) and the calculated optical field (red line) in the TAIWAN eVCA in the top graph. The bottom graph shows the reflectivity (blue line) and group delay dispersion (green line) of the design.

A growth recipe of this structure is found on page 180 in appendix D.

NBI wafer

The NBI wafer has been grown by Claus B. Sørensen on an MBE machine described in detail elsewhere [85]. The machine controls the rate (or the *flux*) of each III/V element by adjusting the temperature of each source. Since the growth rate is not reproducible after a temperature change of the source, the temperature has to be fixed during the growth of the wafer. As the MBE machine only has one Al source, complicated structures with $Al_xGa_{1-x}As$ layers of different x-composition, such as an eVCA, can therefore only be realised by making superlattices of $Al_xGa_{1-x}As$, $AlAs$ or $GaAs$ by turning the shutter in front of the Al source on and off. If the Al and Ga sources are calibrated to $Al_{0.15}Ga_{0.85}As$, $Al_{0.80}Ga_{0.20}As$ can be realised by

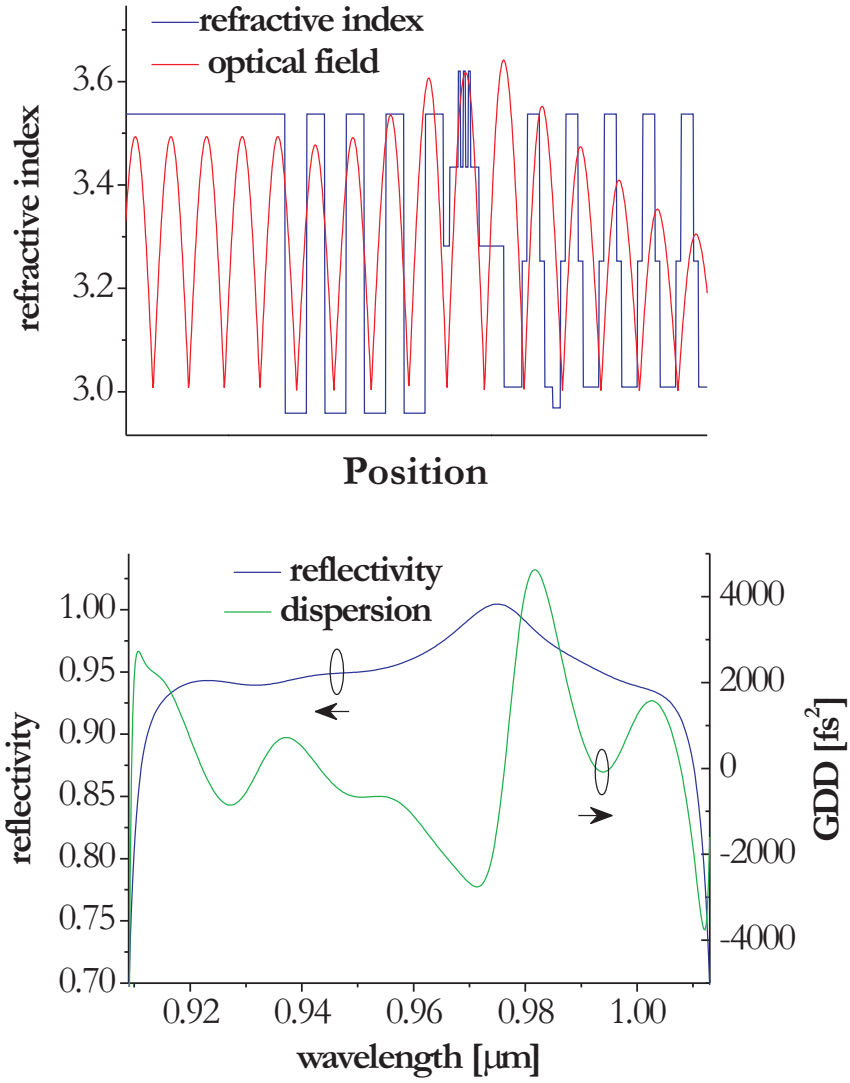

Figure 4.3: Top: refractive index (blue curve) and optical field (red curve) in the TAIWAN design. Bottom: The reflectivity (blue curve) and dispersion (green curve) in units of fs^2 of the TAIWAN design. Note that the cavity resonance is located at $\sim 975\ nm$ instead of $\sim 960\ nm$. The curves are calculated with a gain coefficient of 2000 cm^{-1} and the structure is AR-coated.

making 3.3 nm of $AlAs$ and 1 nm of $Al_{0.15}Ga_{0.85}As$. Each layer of the superlattice is therefore very small compared to the wavelength of the optical field (960 nm).

The three 8-nm $In_{0.175}Ga_{0.825}As$ quantum wells are grown with barriers of $Al_{0.15}Ga_{0.85}As$. The quantum wells are designed to give a photoluminescence at 960 nm. The growth temperature was initially set to 680 ^oC but decreased to 594 ^oC after introduction of In.

On top of the structure, 5 current-spreading layers of 30 nm highly doped ($4 \cdot 10^{18}$ cm^{-3}) $GaAs$ has been grown. The 5 layers are positioned in the node of the optical field. The $SILVACO$ simulations of section 3.8 showed that 5 or 10 highly doped current-spreading layers gave a very small enhancement of the carrier density across a bottom-emitting eVCA with an aperture diameter of 30 μm. However, as the growth of this structure already is complicated by superlattice alloys and ramping of the doping source temperature (the growth of the structure has $\sim$ 460 steps), we chose to limit the number of current-spreading layers to 5.

Two p-type test DBRs consisting of $AlAs/GaAs$ were grown, one with 20 nm $AlAs/GaAs$ uniform superlattice alloys and one without alloys on the $AlAs/GaAs$ interfaces. The center wavelength of the reflectivity of the mirrors was found to shift from 860 nm to around 900 nm even though both mirrors were designed to have center wavelengths of 960 nm. The Ga source was found to have large transients up to 10 % when the shutter was opened and closed rapidly. Superlattice alloys were therefore avoided in the DBRs of the structure, wherefore we chose to grow $AlAs/GaAs$ DBRs and with no composition gradings at the interfaces. A fitting of the reflectivity of the test DBRs with calculated reflectivities furthermore gave us correction factors on the thicknesses of $GaAs$ and $AlAs$ to 1.034 and 1.044 respectively.

The p-DBR consists of 28 pairs of $AlAs/GaAs$ (Be-doped) with delta doping layers on each interface.

The doping sources installed in the MBE are Be (P) and Si (N). The temperature of the sources determines the doping rates. The doping rates of the sources are calibrated per μm deposited material, i.e. the doping rate depends on the material deposited and its growth rate. As $GaAs$ is calibrated to have a growth rate fifteen times larger than $AlAs$ (in order to reach $Al_{0.15}Ga_{0.85}As$), the doping rate at a certain source temperature is fifteen times larger in $AlAs$ than in $GaAs$. This means that a uniform doping profile only can be reached by ramping the source temperature up and down during growth.

The difference of the doping rates in $AlAs$ and $GaAs$ has been used to

make doping gradings on the $GaAs/AlAs$ interfaces of the p-DBR. This doping grading is illustrated in figure 4.4. The $GaAs$ layer is grown at a temperature of the doping source of 890 °C which corresponds to a doping level of $\sim 2{\cdot}10^{18}\ cm^{-3}$ in $GaAs$ (and $\sim 1{\cdot}10^{19}\ cm^{-3}$ in $AlAs$). At the start of the growth of the $AlAs$ layer, the temperature was set to 830 °C which corresponds to a doping level of $\sim 2 \cdot 10^{18}\ cm^{-3}$ in $AlAs$. However, as the doping source has a transient time of $\sim 2\ min$, the doping level in $AlAs$ will slowly fall off from $\sim 1 \cdot 10^{19}\ cm^{-3}$ to $\sim 2 \cdot 10^{18}\ cm^{-3}$ as illustrated in figure 4.4.

The delta doping on the $AlAs/GaAs$ interface, marked with an arrow on figure 4.4, is also made with a doping source temperature of 890 °C. However, in case of this delta doping, the growth was stopped until the temperature of the doping source was constant in order to avoid a doping profile as on the $GaAs/AlAs$ interface.

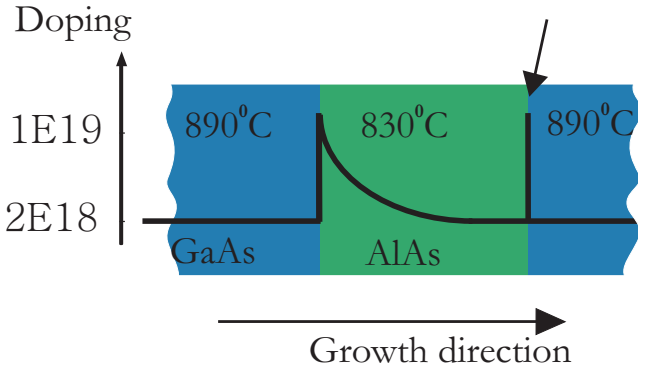

Figure 4.4: Doping profile on the $GaAs/AlAs$-interfaces and the delta doping on the $AlAs/GaAs$ interface of the bottom-DBR in the NBI structure.

The NBI wafer differs from the other two bottom emitting structures by being provided with etch-stop layers (313 nm $Al_{0.80}Ga_{0.20}As$, 67.8 nm $GaAs$ and 81 nm $AlAs$). These layers are designed by the Swiss Federal Institute of Technology, Zürich, because the selective etch was to take place there. However, the thicknesses of each layer in the etch-stop layers are slightly modified in the NBI design to match the wavelength of 960 nm in order to work as an extra pair of n-DBR if they are not etched away.

The quantum well region was grown on test structures with 3, 6 and 9 $In_{0.175}Ga_{0.825}As$ quantum wells with widths of 8 nm with $GaAs$ barriers of widths of 10 nm in order to ensure no strain defects in the final structure. Only the 3-quantum well test structure shows no signs of defects, so we decided to stick to a 3 quantum well structure. Furthermore, a three 8-nm

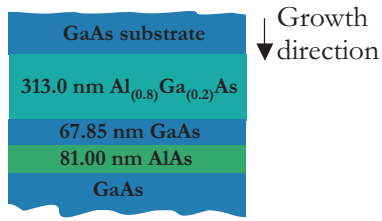

Figure 4.5: Etch-stop layers; the first layers grown on the substrate is an $AlGaAs/GaAs/AlAs$ stack that allows to selectively etch

$In_{0.175}Ga_{0.825}As$ quantum well section with $Al_{0.15}Ga_{0.85}As$ barriers was grown also with no signs of defects.

The p-contact is an un-annealed $TiPtAu$ contact.

The top graph of figure 4.6 shows the refractive index (blue line) and the calculated optical field (red line) of an un-coated NBI eVCA. The bottom graph shows the calculated reflectivity (blue line) and group delay dispersion (green line) of the design. The same curves are calculated for an AR-coated NBI eVCA and shown in figure 4.7.

Appendix D presents the growth recipe of the NBI eVCA.

4.2 Processing of eVCAs

The IQE wafer has been processed at the III/V laboratory at Niels Bohr Institute, except the deposition of the insulating SiO_2 layer which was grown with an E-beam chamber at DANCHIP. The remaining three wafers were processed at DANCHIP.

An overview of the processing of the top-emitting eVCAs and the bottom-emitting eVCAs are shown in figure 4.8 and figure 4.9 respectively.

4.2.1 Processing, step by step

Cleaving

Before processing, the wafers are cleaved to samples of size $\sim 6\ mm \times 8\ mm$. All masks used in the processing are designed to this specific sample size. Each sample can contain around 400 mesas each $25 - 200\ \mu m$ in diameter. Each mesa on the top-emitting sample is processed to one eVCA. The top-emitting samples thus contains around 400 eVCAs per $6\ mm \times 8\ mm$ sample. On the bottom-emitting devices, only 56 of the 400 mesas are

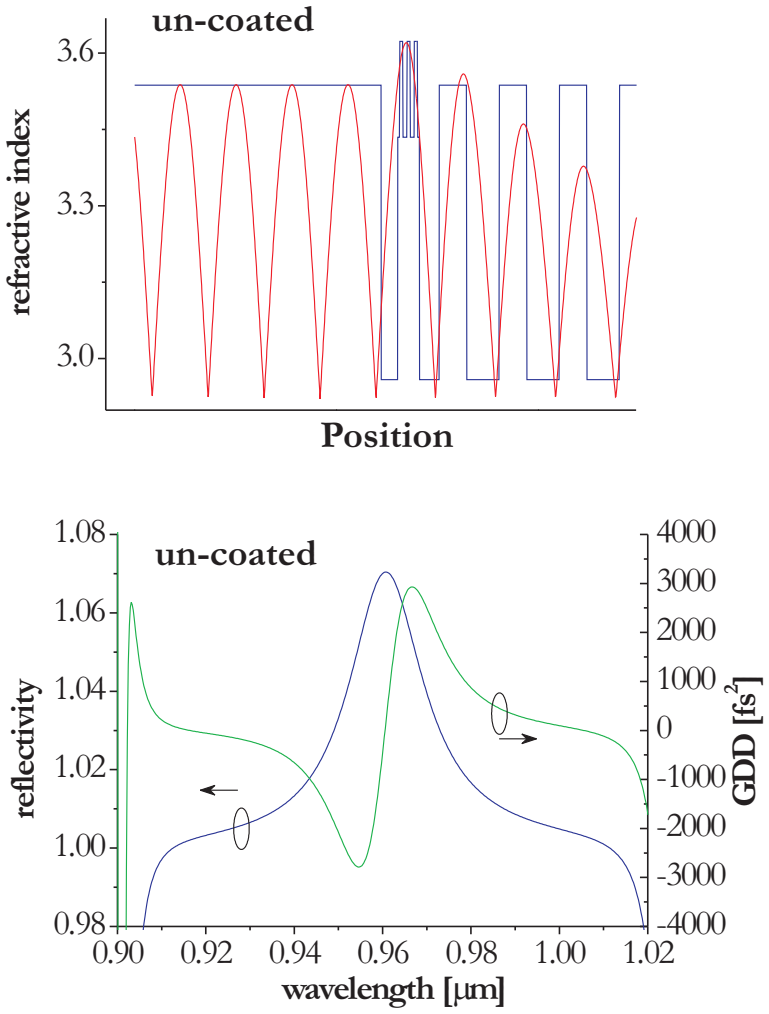

Figure 4.6: Top: refractive index (blue) and optical field (red) in the NBI design. Bottom: The reflectivity (blue) and dispersion (green) in units of fs^2 of the NBI design.

processed to active eVCAs, since the rest are covered with SiO_2. These devices thus contain 56 eVCAs per 6 $mm \times 8$ mm sample.

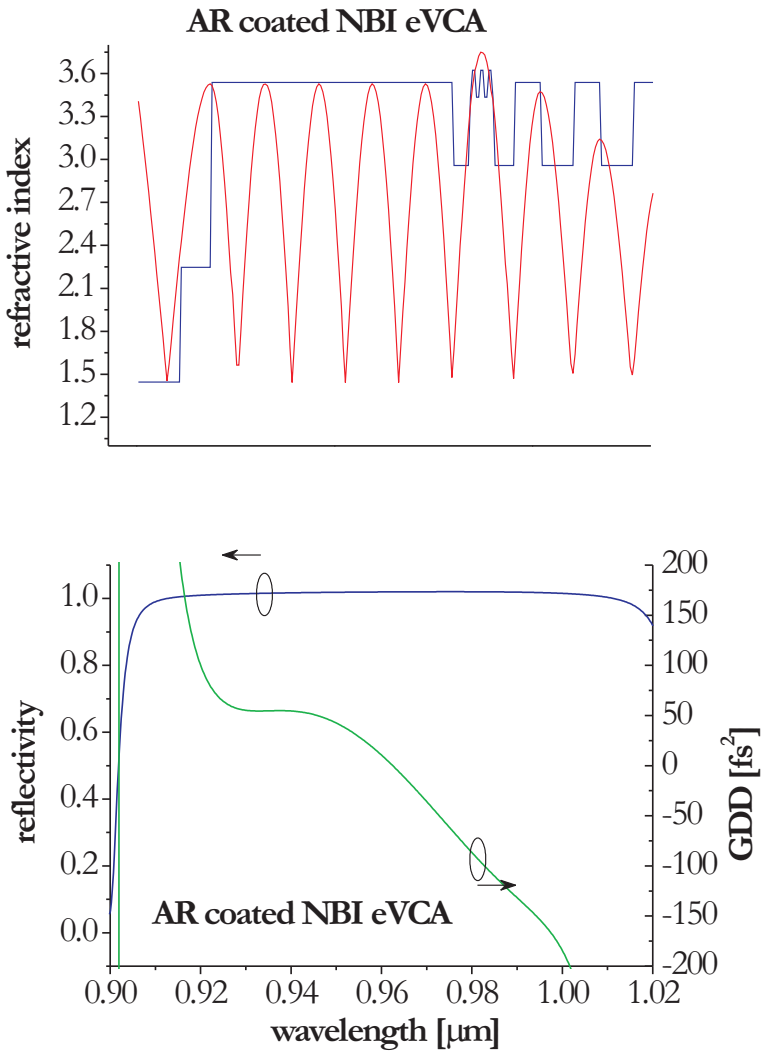

Figure 4.7: Top: refractive index (blue) and optical field (red) of an AR-coated NBI design. Bottom: The reflectivity (blue) and dispersion (green) in units of fs^2 of the AR-coated NBI design.

Cleaning of samples

All cleaning of samples is performed with acetone, methanol or ethanol followed by isopropanol. All samples are furthermore dehydrated in an

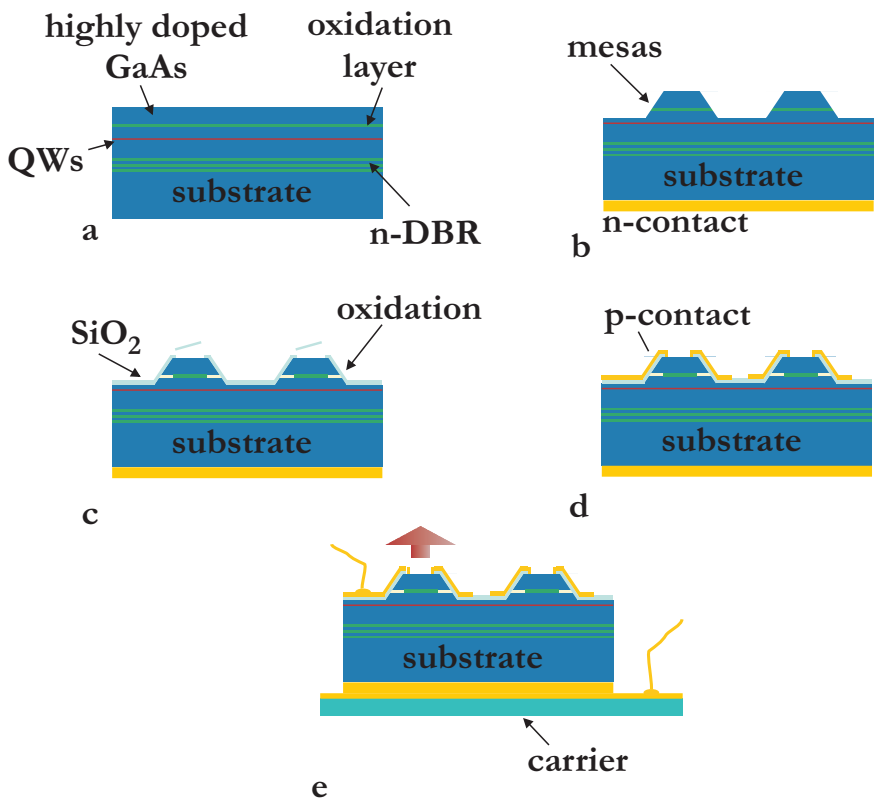

Figure 4.8: Processing steps of a top-emitting eVCA. **a**: the structure with labelled layers. **b**: etching of mesas in the n cap layers and oxidation layer, deposition of n-contact. **c**: oxidation of the oxidation layer, deposition of SiO_2 and removing of SiO_2 on mesas. **d**: deposition of p-contact. **e**: sample mounted on carrier and wire bonded. Light is emitted as indicated with red arrow.

oven or on a hot-plate at 150 $°C$ for $\sim$ 30 min in order to out-gas all water and solvents on the surfaces.

Photolithography

At the Niels Bohr Iinstitute, we used the photoresists from *Clariant Chemicals* named $AZ4511$, $AZ4521$ and $AZ4533$ which have thicknesses of approximately 1.1, 2.1 and 3.3 μm respectively when spinning 40 s at 4000 rotations per minute. The photoresist was soft baked at 110 °C, exposed 10 seconds at an intensity of 5 mW/cm^2, developed in the developer $AZ351B$ (a *Clariant Chemicals* product) diluted $1:4$ in H_2O in around 45 seconds.

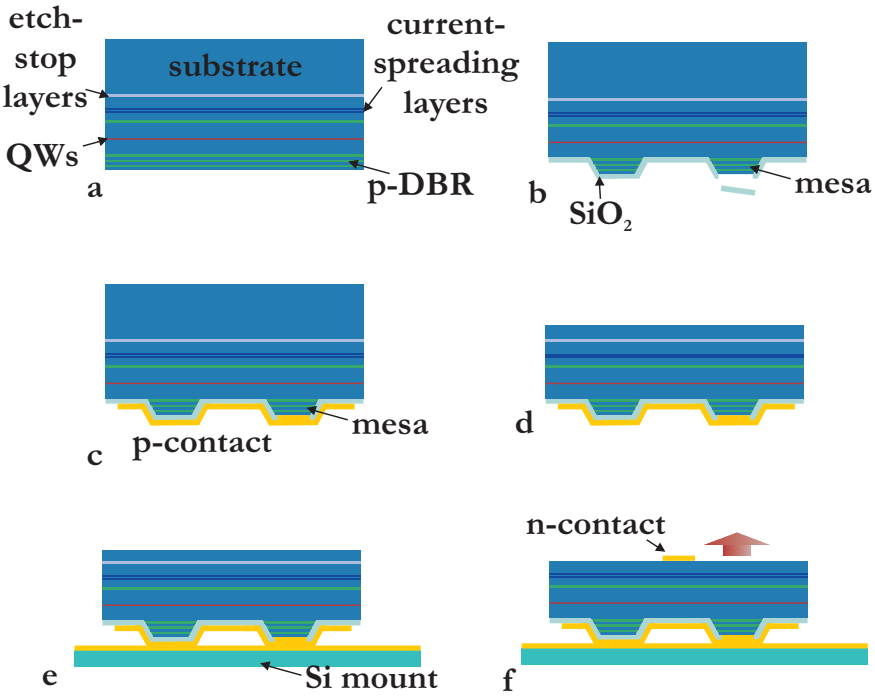

Figure 4.9: Processing steps of a bottom-emitting eVCA. **a**: the structure with labelled layers. **b**: etching of mesas in the p-DBR, deposition of SiO_2 and removing of SiO_2 on selected mesas (the right mesa). **c**: deposition of p-contact covering the "active" mesas. **d**: substrate of sample lapped and polished to a thickness of $50 - 80\ \mu m$. **e**: sample soldered onto gold-patterned Si carrier. **f**: depositing of n-contacts. Light is emitted as indicated with red arrow. There are 56 active mesas on each 6 mm $\times 8$ mm sample.

At DANCHIP we use the photoresist $AZ5214$ which has a thickness of around 2 μm after spinning 40 s at 2500 rotations per minute. $AZ5214$ is soft baked 1 minute at 95 °C, exposed 10 seconds at a intensity of around 10 mW/cm^2 (at 365 nm and 405 nm), developed in $AZ351B$ diluted $1:4$ in H_2O in around 1 minute and finally hard baked at $100 - 115$ °C for $2-4$ minutes.

In photolithography steps performed on SiO_2-surfaces, the samples are enclosed in a container with hexamethyldisilasane ($HMDS$) for around 15 minutes in order to enhance the adhesion of the photoresist on the SiO_2 surface. $HMDS$ forms a thin film strongly bonded to the oxidised surface of the SiO_2 and has free bonds itself that enhances the bonding of the photoresist.

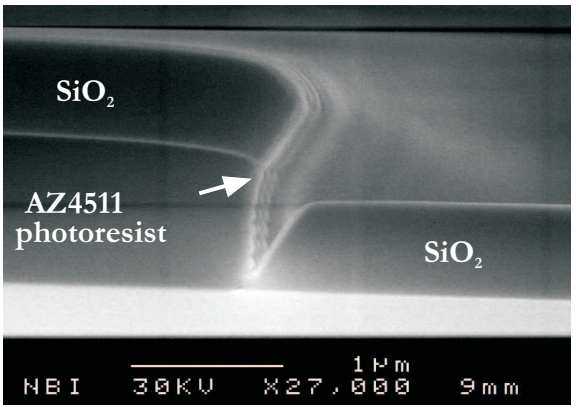

Figure 4.10: $\sim 500nm\ SiO_2$ deposited on $\sim 1.1\mu\ AZ4511$ resist. Lift-off should be possible even though the overhang (marked with white arrow) is very small.

Photoresist is oxygen plasma ashed in around 1 minute at a rate of $\simeq 20\ nm/min$ to get rid of excess resist on developed areas of the sample. No ashing has been done on photoresist used for lift-off since the ashing etches away the desired overhang of the resist (see next section and figure 4.10).

Lift-off

Lift-off is carried out with the use of acetone. It is found crucial to leave the samples in acetone for a couple of minutes and thereafter sprinkle the acetone onto the sample with high pressure. This is especially necessary if small areas are lifted off. In some cases where lift-off for some reason did not work the samples were ultrasonically cleaned (lowest power possible) in acetone for around 30 seconds. Long time or high power ultrasonic cleaning often led to breaking of the samples.

None of the used photoresists are designed to lift-off processes, i.e. their profiles do not have an overhang (see figure 4.10) which enhances the access to the resist from the edges after depositing SiO_2 or contacts. The lift-off step is often a tricky and time consuming step, especially for structures smaller than 40 μm. Even though access to the edges of the resist appears in the Scanning-Electron Microscope (SEM) picture figure 4.10, this structure is very hard to lift-off, and an enhancement of the overhang of the resist is desired.

It is possible to enhance the overhang of the resist by immersing the sample in chlorobenzene before exposure and development [117]. After

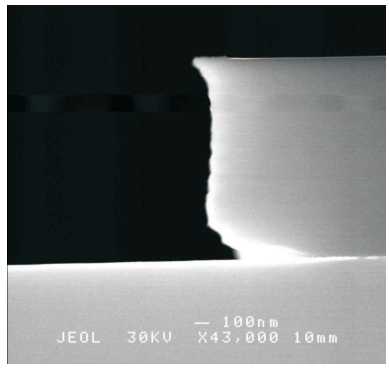

Figure 4.11: Overhang in developed photoresist by immersing in developer ($AZ351B : H_2O$ diluted 1 : 4) 90 s before exposure (30 s immersion gave same effect on some edges).

discussing the matter with *Clariant Chemicals*, I have found it possible to obtain a similar overhang by using the $AZ310B$ developer instead of chlorobenzene. The overhang of a resist immersed in chlorobenzene is shown in figure 4.11. The developer technique gives better results as the resists tended to crack off when using the chlorobenzene technique, probably because the surface of the photoresist becomes too rigid and therefore cannot expand during exposure.

Another way of enhancing the overhang of the resist is by cooling the developer to around 5 °C and developing for twice the usual time. This enhances the development at the surface of the 'warm' sample and should thus leave a profile somewhat similar to the profiles in figure 4.11. I have nevertheless not experienced any improvement in the lift-off process using this technique.

If the resolution of the photolithography is not crucial one can simply develop the resist $3-4$ times longer than usual, resulting in a better lift-off, probably due to an over-exposure of the bottom part of the resist. However, this has not been studied in detail in the SEM.

Photoresist used for metal or SiO_2 lift-off was not hard baked at all, making the lift-off process a lot easier.

Etching of mesas

Mesas are etched in order to reach the oxidation layer in the top-emitting eVCAs and for confining the current in the bottom-emitting eVCAs (as the oxidation layers of the bottom-emitting eVCAs are not used). The etching

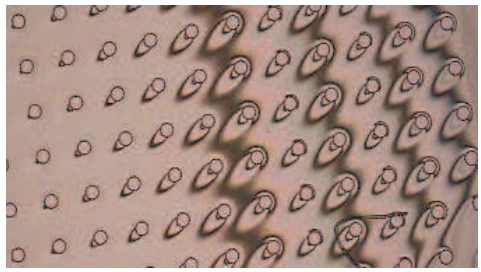

Figure 4.12: An inhomogeneous etching of mesas in the DBR of a bottom-emitting structure results in areas of $AlAs$ (dark areas) on the surface of the sample, which makes further processing difficult, as SiO_2 does not adhere very well on $AlAs$.

of shallow mesas, i.e. for top-emitting eVCAs, is carried out with a $1:1:38$ solution of $H_3PO_4(85\%) : H_2O_2(31\%) : H_2O$ which has an etching rate of $\sim 100\ nm$ per minute. On the bottom-emitting eVCAs, where the mesas are etched through the p-DBR, a solution of $10:2:60$ $H_3PO_4(85\%) : H_2O_2(31\%) : H_2O$ with an etch rate of $\sim 200\ nm$ per minute or a solution of $10:2:30$ $H_3PO_4(85\%) : H_2O_2(31\%) : H_2O$ with an etch rate of $\sim 600\ nm$ per minute is used. The fast etch gives the most homogeneous etching, thus making it easier to stop on a $GaAs$ layer on the whole area of the sample. The etching is attempted stopped on a $GaAs$ layer because an $AlAs$ surface oxidises very easily making further processing difficult, as SiO_2 does not adhere very well on oxidised $AlAs$, illustrated in figure 4.13. A rough etch is shown in figure 4.12, the dark areas are oxidised $AlAs$. These $AlAs$ areas are etched away by immersing the samples in hydrofluoric acid $(38-40\ \%)$ around $10-15$ seconds after a quick $(\sim 2\ s)$ rinse with demineralised water immediately after mesa etch.

The mixing of the etches is carried out with refrigerator-cold demineralised water in order to avoid heating of the etch. The etching takes place in a small bowl and is continuously stirred with a magnetic stirrer with $200-300$ rotations per minute. A too violent stirring will cause an uneven etch around the mesas, as in figures 4.12 and 4.13. The bowl is kept in a cold $(15-17\ ^\circ\mathrm{C},)$ bath during the whole process.

Oxidation

The IQE, ORC and TAIWAN structures are equipped with oxidation layers, consisting of $Al(Ga)As$. The oxidation layer is oxidised in a sealed chamber through which nitrogen saturated with vapourised demineralised

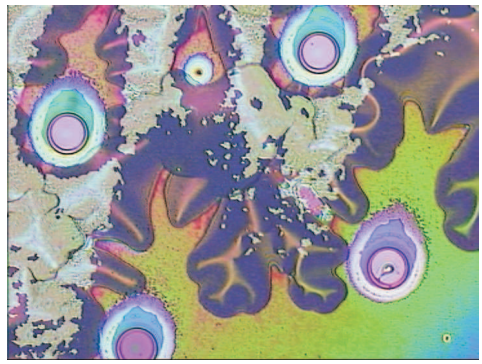

Figure 4.13: SiO_2 is deposited on an inhomogeneously etched sample which has areas of $AlAs$ on the surface. Note the un-even halo-like etching around the mesas due to too heavy agitation during etching.

water flows. During the oxidation, the chamber is heated to $\sim 385\ ^{\circ}C$ depending on the thickness and composition of the oxidation layer. An oxidation of around 20 minutes will oxidise around 10 μm on the IQE samples on mesas sizes from $30 - 50\ \mu m$. The oxidised aperture can be measured with an optical microscope, shown in figure 4.14. A detailed presentation of the oxidation set-up and procedure of the oxidation is described in [118].

The rate of oxidation seems to depend greatly on the origin of the samples; the IQE samples are relatively easy to oxidise, i.e. the $AlAs$ layer does not seal easily (see section 3.7), and the process shows acceptable reproducibility. The ORC samples appear quite impossible to oxidise; even though the samples are put into the oxidation chamber less than ten minutes after etching (as fast as possible when the oxidation chamber is outside the clean room), no oxidation is detected, probably due to sealing of the $AlAs$ layer.

No oxidation is performed on the TAIWAN eVCAs, as it is a time consuming process step. Furthermore, the p-contact and the mesa itself make a fairly good aperture as long as the contact covers as large an area of the mesa as possible.

Passivation with SiO_2

The deposition of SiO_2 on the IQE samples is carried out with an $e - beam$ chamber with SiO_2 granulate as source. The deposition rate is very difficult to control, and the quality of the SiO_2 very poor. A layer of up to $400 - 500\ nm$ is deposited in order to ensure passivation.

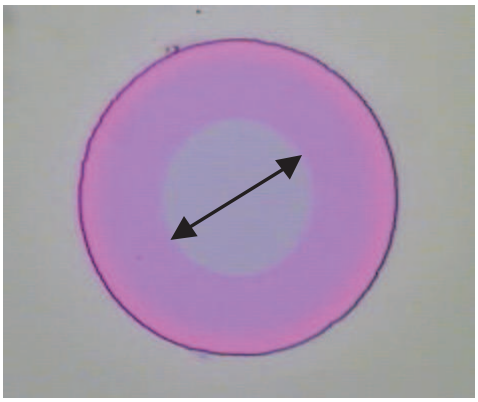

Figure 4.14: An aperture of $\sim 30\ \mu m$ oxidised into a mesa of $\sim 70\ \mu m$ in diameter.

The passivation of the bottom-emitting structures is performed with a plasma-enhanced chemical-vapour-deposition ($PECVD$) chamber which provides a high-quality layer of SiO_2. Unfortunately, no photoresist is allowed in this chamber, which is why the SiO_2 on the active mesas (e.g. the mesa to the right in figure 4.9) is etched away with hydrofluoric acid. Only $\sim 80\ nm\ SiO_2$ deposited with this chamber is needed to provide passivation of the surface.

Lapping and polishing of substrate

Lapping and polishing of substrates are performed on a *Logitech PM5* Lapping & Polishing Machine. The machine is constructed with a heavy, flat glass plate that rotates with a user-defined speed. A cylinder filled with a solution of H_2O and a slurry containing 3 μm grains of Al_2O_3 is positioned onto the machine. The cylinder is supplied with a tap that provides approximately $1-3$ drops of the solution per second onto the rotating glass plate. The samples are waxed to a glass mount that is mounted on a jig, which is positioned on top of the rotating glass plate, samples facing downward. The jig is constructed in a way that makes it easy to control the pressure of the samples onto the glass plate with the Al_2O_3 slurry. The rotation of the glass plate is typically set to 20 rpm when lapping. The lapping rate varies from $2-4\ \mu m$ per minute, depending on the pressure of the samples onto the glass plate.

When the samples are lapped, the cylinder containing the Al_2O_3-slurry is replaced with a cylinder containing a sodium-hypochlorite solution called

Chemlox ©, which etches *GaAs*. The glass plate is replaced by a plate covered with a soft cloth, and the procedure is repeated. The rotation of the plate is increased to around 70 *rpm*. In order to ensure an optically smooth surface, at least 30 μm of the substrate should be polished away. The polishing rate is $4 - 9$ $\mu m/min$.

As the *Logitech PM*5 is constructed to large-wafer lapping and polishing, many samples corresponding to an area of around a quarter 2-inch wafer should be lapped and polished in each run.

As the samples are very fragile after lapping and polishing of the substrate, the samples are handled and carried with clean room tissues instead of tweezers after this process step. The wax on the samples is removed by immersing the samples in *Ecoclear* © at ~ 60 °C in around 15 *min* and thereafter immersed and sprinkled gently with acetone, methanol and isopropanol.

Removal of substrate

The complete removal of the substrate of the NBI sample is performed at the Swiss Federal Institute of Technology, Zürich. The etch-stop layers consist of 313 *nm* $Al_{0.8}Ga_{0.2}As$, 67.85 *nm* *GaAs* and 81 *nm* *AlAs*.

The procedure is as follows: The *GaAs* substrate is first lapped and polished to around 40 μm. The rest of the substrate is then jet-etched with a solution of $NH_4OH : H_2O_2 : H_2O$. This etch oxidises *AlAs*, wherefore the first etch-stop layer is made of $Al_{0.8}Ga_{0.2}As$ instead of pure *AlAs* [119]. This layer of $Al_{0.8}Ga_{0.2}As$ is removed by Hydrofluoric acid, HF. Concentrated HF (48 %) is found to have an selectivity of $> 10^7$ in *AlAs* over *GaAs* [120]. For etching of this layer, an HF concentration of ~ 1 % is used, which has an etch rate of > 600 nm/min. Thereafter the GaAs is etched by a citric acid [121]; monohydrate citric acid is mixed 1 : 1 with H_2O by weight. Thereafter this solution is mixed 4 : 1 with 30 % H_2O_2 which gives an etch rate of ~ 5 nm/s and a selectivity of ~ 1400 over *AlAs*. The last layer of *AlAs* is etched with HF.

The design of the etch-stop layers on the NBI wafer is a modification of the usual etch-stop layers used at *ETH Zürich* (see page 86), and the selective etches of these modificated layers are tested on test-wafers at *ETH Zürich* in collaboration with Benjamin Rudin, Aude-Reine Bellancourt and Deran Maas. The etch of the *real* NBI samples are accomplished also at *ETH Zürich* by Benjamin Rudin.

An NBI sample after substrate removal is shown in figure 4.15.

After removal of the substrate, the samples easily break (or rather *crumble*) during transportation, cleaning or even when blow drying with N_2.

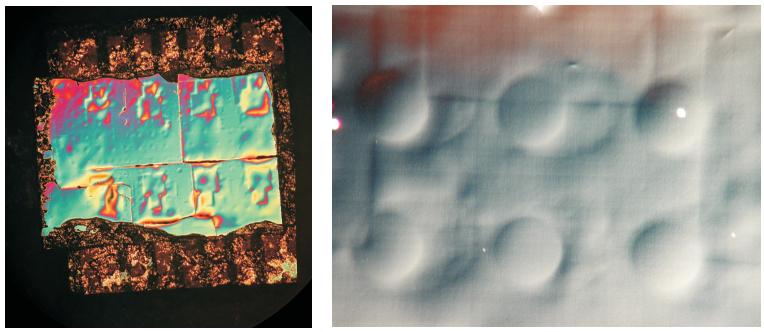

Figure 4.15: NBI eVCA with removed substrate Au/Sn soldered to a carrier (left). The mesas and p-contacts on the backside (p-side) of the sample are visible on the surface of the sample (right).

Because of this, no top-contacts are deposited. Instead, the samples and mounts are glued onto chipcarriers and wire-bonds are carefully silver-glued to the n-side of the samples.

Contacts

The n-contacts on the IQE samples are 40/60/27/200 nm $Ge/Au/Ni/Au$ contacts. The n-contacts are deposited right before the etch of mesas and annealed in the oxidation process. The p-contacts of the IQE samples are 10/150 nm Cr/Au contacts, which is the only p-alloy available at the clean room facilities at the Niels Bohr Institute. As discussed in section 3.9, this contact should be annealed. However, annealing of these contacts seems to destroy the samples; at ~ 240 °C, small bubbles appear on the surface of the samples. The origin of the bubbles has not yet been determined. These p-contacts are therefore not annealed.

The contacts on the ORC samples are the same as on the IQE samples.

Both n-, and p-contacts on the TAIWAN samples are of 50/100/200 nm $Ti/Pt/Au$ and none of the contacts were annealed. The p-contacts on the NBI samples are 50/100/200 nm $Ti/Pt/Au$ contacts and the n-contacts are made of silver glue.

4.2.2 Sample mounting and bonding

A fully processed top-emitting eVCA is shown in figure 4.16. The diameter of the top-contact is around 20 μm and the diameter of the mesa is around 40 μm.

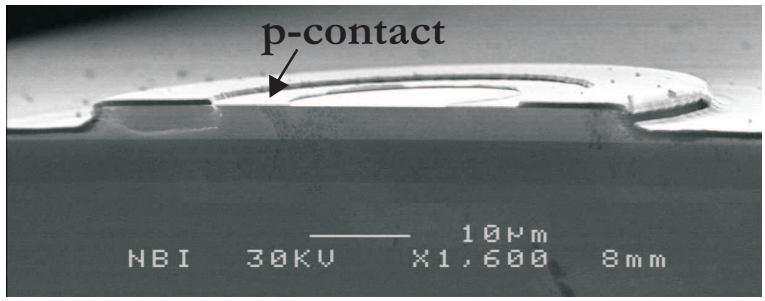

Figure 4.16: A SEM picture of a processed IQE top-emitting eVCA. The diameter of the top-contact is around 20 μm and the diameter of the mesa is around 40 μm.

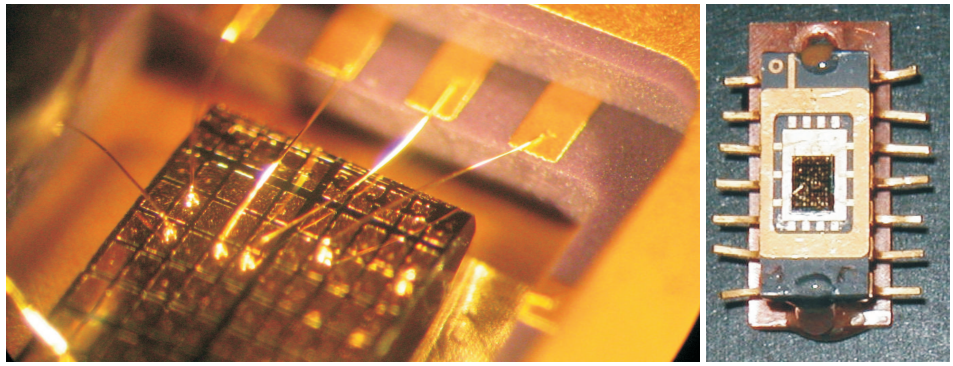

Figure 4.17: An IQE top-eVCA glued and bonded to a $CuMo$ carrier.

All 6 $mm \times 8$ mm samples are cleaved into four 3 $mm \times 4$ mm samples before mounting.

The top-emitting samples are silver-glued to a gold-coated surface of a $CuMo$ chip carrier (to the right in figure 4.17) which has 14 bonding pads each connected to a leg. $\sim$ 10 eVCAs are wire bonded to bonding pads (to the left in figure 4.17). The n-contact of the sample rest on the gold coating on the chip-carrier. This gold coating is connected to a couple of bonding pads with wire bonds, as illustrated in figure 4.8 **e**.

The bottom-emitting samples are soldered using Au/Sn (80/20 $w\%$) or silver-glued to contact-patterned carriers, as illustrated in figure 4.18 (right). The carriers are made of undoped Si-wafers onto which 14 arms of 50 nm/100 nm/250 nm $Ti/Pt/Au$ of 200 μm width have been deposited.

The soldering includes a heating of the samples to $\sim$ 380 °C. The soldering of the bottom-emitting structures is not very strong, and cannot

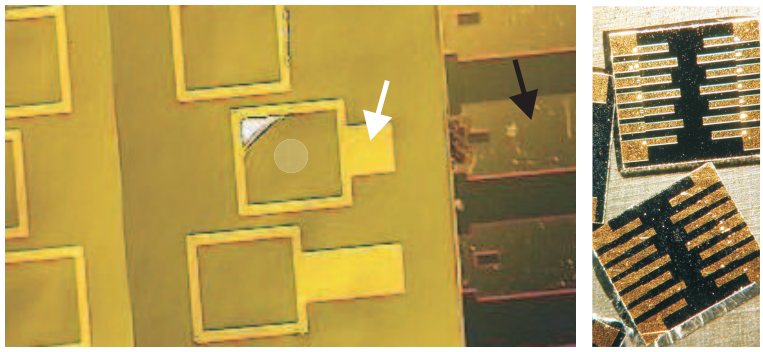

Figure 4.18: Left: a bottom-emitting eVCA Au/Sn soldered to a chip carrier. The black arrow shows the p-contact, that is connected to an eVCA underneath the sample (indicated by grey circle). The white arrow shows the n-contact, which encircles the eVCA on the other side of the substrate. The p-contact is used for aligning the n-contacts. Notice how the sample is broken in a straight line to the left. This tend to happen to 'large' samples ($3\ mm \times 4\ mm$) during the n-contact lift-off process. Right: two gold-patterned Si-carriers.

hold the stress involved with the lapping and polishing of the substrates. The soldering of the samples is performed after substrate lapping and polishing. However, some of the bottom-emitting samples even break off their carrier during processing of the n-contacts.

The lack of strength of the soldered samples was first attributed to the different thermal expansion coefficients of $GaAs$ and Si ($\sim$ 5.7 and $\sim$ 2.6 $ppm/°$C respectively). Some samples were soldered to gold-patterned AlN carriers, as AlN has a thermal expansion coefficient close to $GaAs$ ($\sim$ 5.3 $ppm/°$C). However, this did not solve the problem.

A closer examination of samples that fell off the carriers during n-contact processing shows that also the SiO_2 is ripped off, suggesting that it is the adhesion of SiO_2 to $GaAs$ that cannot tolerate a heating of the samples to $\sim$ 380 °C.

No similar problems are experienced with the silver-glued samples. However, as the active mesas on the sample are only separated by $\sim 400\ \mu m$, one has to be very careful and use very small blobs of glue in order not to connect all the eVCAs on the sample.

Most samples are AR-coated with a two-layer TiO_x/SiO_2 coating before characterisation. This coating ensures a reflectivity below 10^{-5} [122].

Chapter 5

Characterisation of eVCA

5.1 Introduction

This chapter presents the characterisations of the four eVCAs. Basic diode characterisations, i.e. nearfields of the emitted light and output power and voltage versus the injected current, are presented in section 5.2. Measurements of the reflectivity of the structures (gain in the quantum wells) versus the injected current are presented in section 5.3. Furthermore, the IQE eVCA was set to lase in an external cavity, the characterisation of which is presented in 5.4.

5.2 Diode characterisation of eVCA

5.2.1 IQE eVCA

The IQE samples are all silver-glued to $CuMo$ carriers as illustrated in figure 4.17 and ~ 10 eVCAs on each sample are wire bonded to the carrier.

Figure 5.1 shows the output power (top graph) and the voltage (bottom graph) versus the injected current of eight IQE eVCAs from four different samples, M, Y, BJ and P. Two curves from two different eVCAs on the same sample are plotted, and the aperture diameter is noted to each pair of curves. The maximum output power is 207 μW found in an eVCA with an aperture diameter of 23 μm (sample M). The processing procedure of the two samples with 23-μm aperture diameter (sample M and Y) are similar, except for the fact that sample M has a contact aperture diameter of 25 μm and sample Y has a contact aperture diameter of 20 μm.

Nearfields of the IQE eVCAs show that this top-emitting structure has serious current-spreading problems at aperture diameters larger than

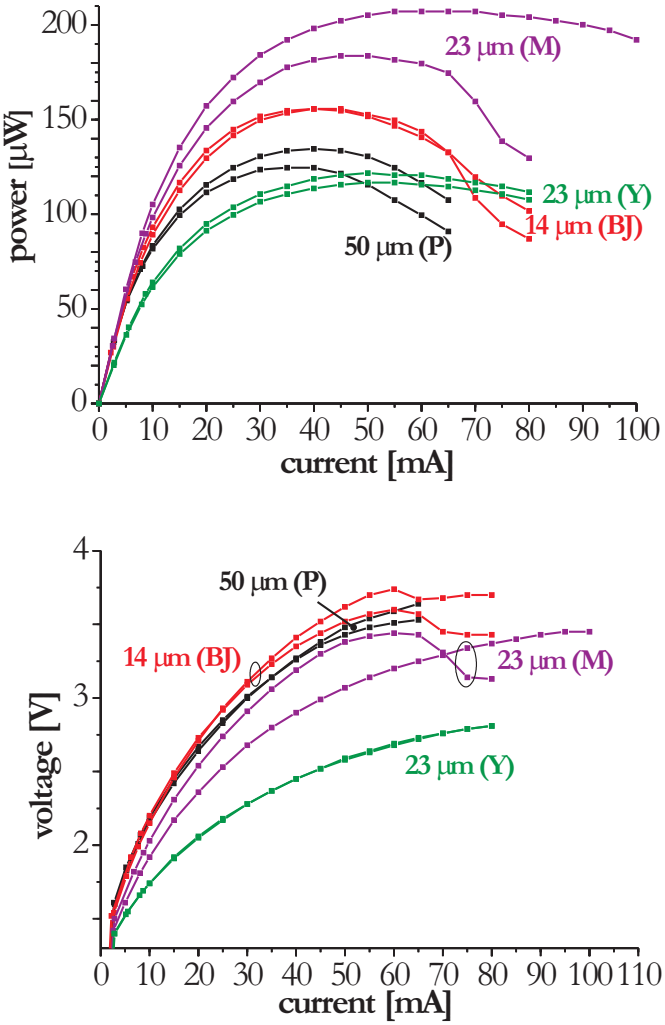

Figure 5.1: Top graph shows PI curves and bottom graph IV curves of eight IQE eVCAs. The numbers refers to the oxide aperture diameters and the number in parenthesis is the sample name.

around 25 μm. Figure 5.2 shows the nearfield intensity for three different aperture diameters. It is clear that the highly doped layers underneath the ring-shaped p-contact do not support enough lateral current-spreading for large apertures.

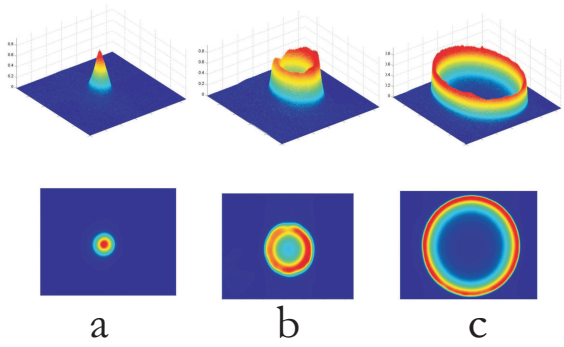

Figure 5.2: Nearfields of three IQE eVCAs with apertures diameters of 8 μm (**a**), 50 μm (**b**) and 100 μm (**c**).

Even the eVCA with the 23 μm aperture on sample M shows some irregularities in the current profile across the aperture as illustrated to the left in figure 5.3. To the right in the same figure is shown the nearfield of a neighbouring eVCA that on the surface seemed fine but the nearfield indicates some sort of leakage current on the edge of the mesa, which could be due to a bad passivation layer (SiO_2). Even though the thickness of this layer is $500nm$, it is grown in an $e-beam$ chamber, which gave thin films with poor electrical insulating behaviour.

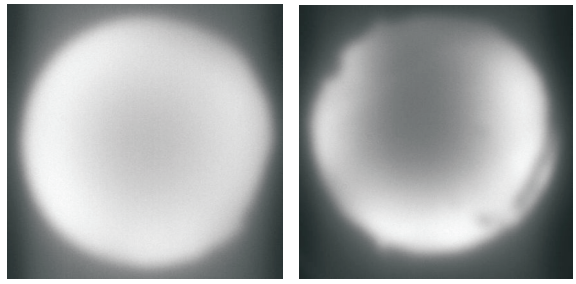

Figure 5.3: Nearfields of two eVCAs on sample IQE M with aperture diameter of 23 μm.

The differential resistance at current injections 10 times the transparency current, $10 \cdot I_{tr}$, where the transparency current density J_{tr} is assumed to be 500 A/cm^2 (see section 5.3), is plotted versus the oxide aperture diameter in figure 5.4. The oxide aperture diameter and the contact aperture diameter are specified in parenthesis to each point. The differential resistance falls off at large oxide apertures. The relatively high

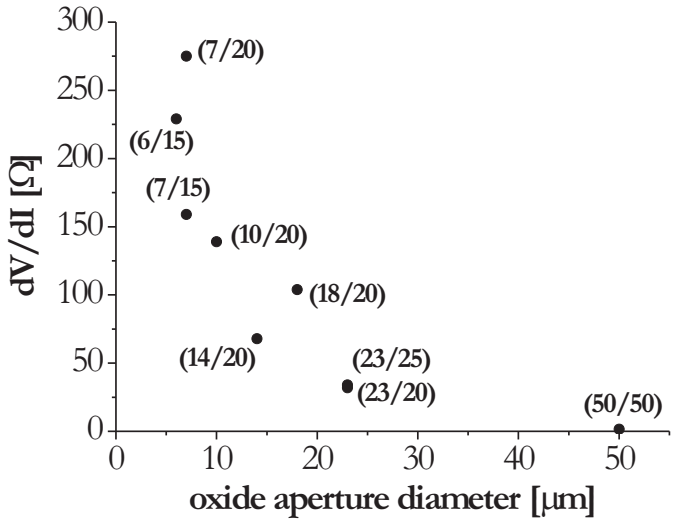

Figure 5.4: Differential resistance at $10 \cdot I_{tr}$ (J_{tr} assumed to be 500 A/cm^2) versus the oxide and contact aperture diameters, which are specified in parenthesis to each point ($d_{ox}/d_{contact}$).

differential resistance of the eVCA with the 7 μm oxide aperture diameter and 20 μm contact diameter could be due to the high lateral resistivity in the highly doped layers, as discussed on page 57.

5.2.2 ORC eVCA

The *ORC* eVCAs are the first bottom-emitting structures to be processed at COM · DTU. Attempts of oxidising the 30 nm $AlAs$ failed, the characterised samples presented here are thus not oxidised. The aperture on these samples is defined by the opening in the SiO_2-passivation layer as illustrated in figure 4.9 **b**. After substrate thinning, the samples are silver-glued onto carriers as illustrated in figure 4.18, and n-type contacts are deposited on top of the thinned substrate using standard photolithography. The samples with their carriers are hereafter glued on $CuMo$ carriers and ~ 6 eVCAs wire bonded to the carrier.

One eVCA is tested without lapping of the 350 μm substrate. The aperture diameter of this eVCA is 55 μm and the maximum output power is 95 μW at 120 mA which is not very promising compared to the IQE

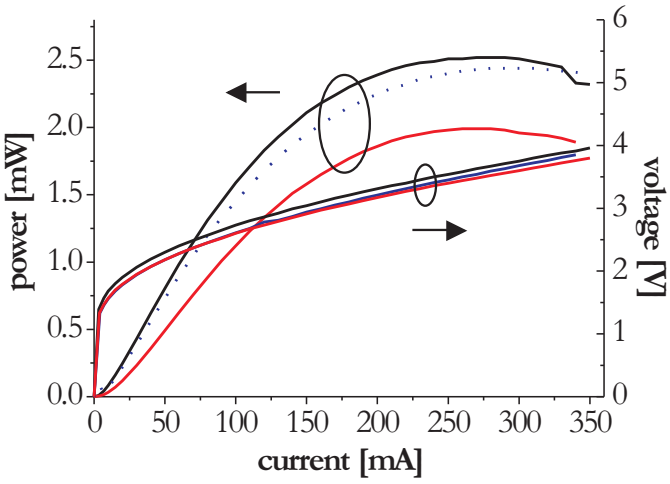

Figure 5.5: PI and current-voltage curves of three ORC eVCAs, all with oxide aperture diameters of 80 μm.

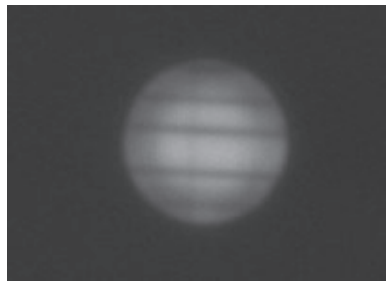

Figure 5.6: The nearfield of on of the ORC eVCA. The ORC wafer has 9 quantum wells of 8-nm $In_{0.17}Ga_{0.83}As$ and $GaAs$ barriers.

structure, even when the absorption in the substrate is taken into account.

The first substrate-thinned ORC sample is lapped and polished to a thickness of 80 μm. All eVCAs on this sample have an aperture diameter of 80 μm. Figure 5.5 shows the output power and IV-curve of three eVCAs on this sample after AR-coating. The maximum output power is 2.52 mW, and the differential resistance above 200 mA is around 5 Ω.

The sample has not been mounted on a temperature controller while recording the PI, and IV curves. Immediately after each series of mea-

surements, the output power is found to drop around 0.1 mW at 100 mA injection current due to heating of the sample.

The PI-curves are not linear at small injected currents due to the top DBR which causes the output power to be *laser*-like.

Figure 5.6 shows the nearfield of one of the eVCAs after AR-coating. The nearfield is patterned by a web of dark lines across the aperture, all lines aligned with the the edges of the sample. These dark lines are most likely due to defects in or around the quantum wells. After this discovery, further processing of the ORC wafer was abandoned.

5.2.3 TAIWAN eVCA

None of the TAIWAN eVCAs are oxidised to form oxide apertures, the aperture diameters of these samples are thus the opening diameter in the SiO_2 as on the ORC eVCAs. The substrates are lapped to $47 - 56$ μm and either silver-glued or Au/Sn soldered onto gold-patterned Si carriers as illustrated in figure 4.18. N-type contacts are deposited on top of the thinned substrate using standard photolithography. The samples are hereafter AR-coated with TiO_x and SiO_2.

Wire bonding is not possible on these structures. The 3 mm $\times$4 mm TAIWAN samples break easily even when gluing them to the carriers or by spinning or lifting off photo-resist for the n-contact processing. The samples are therefore probed in the diode characterisation.

Figure 5.7 shows the amplified spontaneous emission (ASE, red curve) and the reflectivity (blue curve) of the structure seen from the top DBR. It clearly shows that the cavity dip of the structure is located at around 975 nm instead of 960 nm as designed.

It turns out that the TAIWAN structure was, due to a serious misunderstanding between the grower at LandMark Optoelectronics Corporation and us, grown with an etalon-thickness of 975 nm. As it is impossible to learn exactly *how* they changed the structure (the final growth recipe is confidential), we assume they adjusted the $Al_{0.15}Ga_{0.85}As$ layers to make the un-doped $\lambda/2$ quantum well section fit to 975 nm. In practice, this means that layer number 8 and 16 in recipe in appendix D (page 180) has been adjusted from 10 nm to 17.5 nm. Calculations of the reflectivity of such a (corrected) structure is presented in figure 4.3 on page 84, and shows that the misunderstanding means that there is no net gain in the entire structure at 960 nm at all.

The PI, and IV curves of six TAIWAN eVCAs are shown in figure 5.8. The aperture diameter and sample number (in parenthesis) of the eVCA is noted at every curve on the graphs. The maximum output power is found

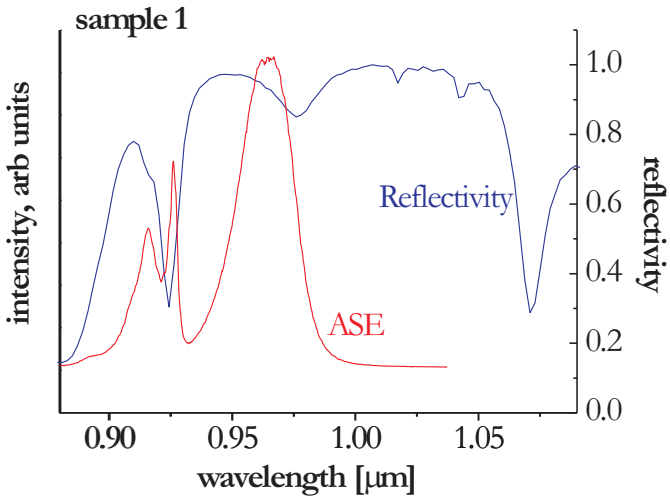

Figure 5.7: Amplified spontaneous emission (ASE, red curve) and the reflectivity (blue curve) of the TAIWAN structure.

in the eVCA with the largest processed aperture diameter of 150 μm.

The turn-on voltage of the TAIWAN eVCAs are slightly higher than in the ORC eVCAs. This can either be due to a Schottky barrier between the eVCA and the deposited contacts or due to the fact that the TAIWAN eVCAs are probed during the characterisations.

A typical value of the differential resistance of a TAIWAN eVCA with an aperture diameter of 80 μm at 200 mA is close to 1 Ω, i.e. much smaller than the differential resistance of an ORC eVCA with same aperture diameter, which was around 5 Ω.

5.2.4 NBI eVCA

After substrate lapping and polishing, the samples are soldered or silver-glued to gold-patterned Si carriers. The removal of the substrates on all NBI samples is performed by Benjamin Rudin at the Swiss Federal Institute of Technology, Zürich. Since n-contact processing on these samples is not possible after substrate removal, the samples and their Si carrier are silver-glued to a $CuMo$ carrier similar to that of figure 4.17, and bonding wires are connected to the n-side of the samples by blobs of silver glue. A test of this technique has been performed on a TAIWAN sample and it had a

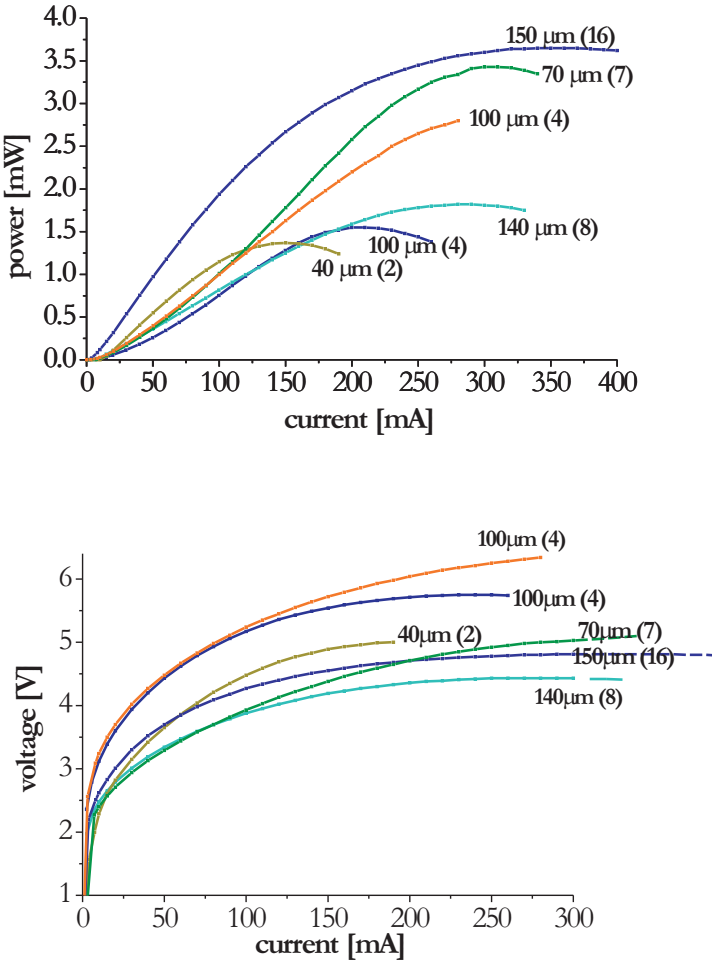

Figure 5.8: PI and IV curves of TAIWAN samples. Aperture diameters and sample number in parenthesis.

slightly larger serial resistance compared to a probed device.

The substrate removal step has a very bad yield. The samples crumble and break easily during the process of substrate removal, or when silver-gluing bonding wires to the n-side of the samples, as shown in the photograph in figure 5.9. Unfortunately, all fully processed NBI eVCAs show sign of open circuitry. Probing of the NBI eVCAs has also been tested. However, the samples broke under the pressure of the probe.

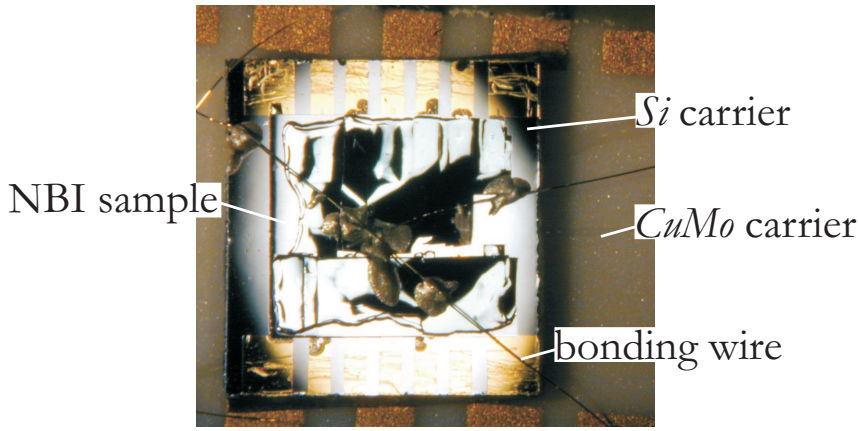

Figure 5.9: A NBI sample and its *Si* carrier glued onto a *CuMo* carrier. The sample crumbled when gluing the bonding wires to the n-side of the sample.

5.2.5 Discussion

Figure 5.10 shows the maximum emitted output power density versus the aperture of the three eVCA structures, IQE, ORC and TAIWAN. It clearly shows a fall-off in the power density at large apertures for all three structures, suggesting lack of current spreading at large apertures. The bottom-emitting eVCAs (ORC and TAIWAN) have an enhanced power density at aperture diameters larger than 40 μm compared to the top-emitting IQE eVCAs. However, the output power density of the bottom-emitting structures falls off rapidly at aperture diameters larger than ~ 80 μm.

The diode characterisations show the advantage of bottom-emitting structures over the top-emitting structures in an increased maximum output power. Also, the characterisations show the limitations in the bottom-emitting structures with regard to their apertures sizes.

Table 5.1 shows the maximum output power of the three types of eVCAs and and their aperture diameter *and* the differential resistivity of three types of eVCAs with aperture diameters of 50 and 80 μm at current densities, J.

The differential resistivity of the ORC eVCA is quite large compared to the TAIWAN eVCAs. This can be due to the defects in the ORC structure which could induce a high differential resistivity. The high differential resistance could also be due to the thicker n-DBR (7.5 pairs in the ORC structure versus 4.5 pairs in the TAIWAN structure).

The NBI design seems to be a too ambitious design. The samples

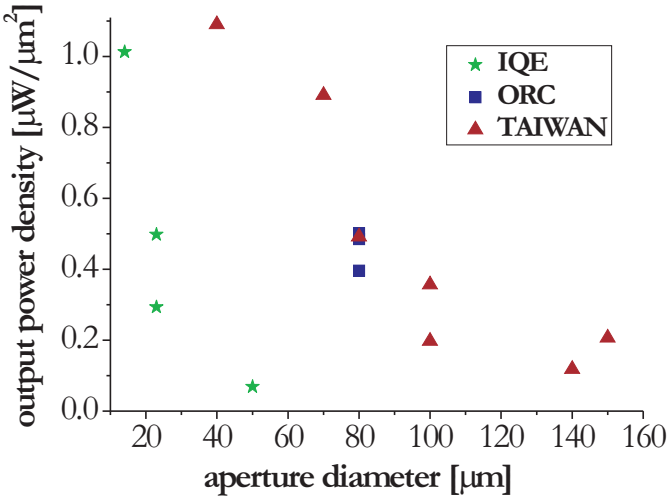

Figure 5.10: Power emitted per aperture area for the three different types of eVCAs.

eVCA name	aperture diam. $[\mu m]$	max power $[mW]$	aperture diam. $[\mu m]$	J $[kA/cm^2]$	dV/dI $[\Omega]$
IQE	23	0.207	50	~ 5	~ 1.5
ORC	80	2.52	80	~ 10	~ 5
TAIWAN	150	3.65	80	~ 10	~ 1

Table 5.1: Measured maximum output powers of the three types of eVCAs; IQE, ORC and TAIWAN. To the right, the aperture diameters and the differential resistivities of the three types of eVCAs with aperture diameters of 50 and 80 μm at current densities J.

crumble and break after substrate removal even though they are glued onto carriers. One solution is to avoid the etched mesas on the p-side of the structures and to cleave the samples into smaller devices, that e.g. only have $1-2$ eVCAs per sample. In this way, the samples might be glued or soldered more tightly to the carriers.

Furthermore, the NBI samples with removed substrate are too fragile to process n-contacts. Other processing procedures should be investigated if such a design is pursued, e.g. partial removal or etch of the substrate as

illustrated in figure 3.15 on page 47.

5.3 Measurements of reflectivity versus injected current

The reflectivity versus the injected current has been measured on a single IQE eVCA and two TAIWAN eVCAs. The setup is as illustrated in figure 5.11.

The $MIRA\ 900-F$ titanium-sapphire ($Ti{:}Al_2O_3$) laser system is pumped by a $5W\ Verdi$ laser. The $MIRA$ laser is tunable in the range from 700 to 980 nm. In these experiments, the laser is tuned to 980 and 960 nm for the IQE and TAIWAN structures respectively. The cavity of the $MIRA$ laser is continuously purged with N_2 in order to reduce the cavity humidity. The output power of the laser system is found to fluctuate $2-3$ % on a timescale of around $30-50$ seconds, even when operated in CW mode.

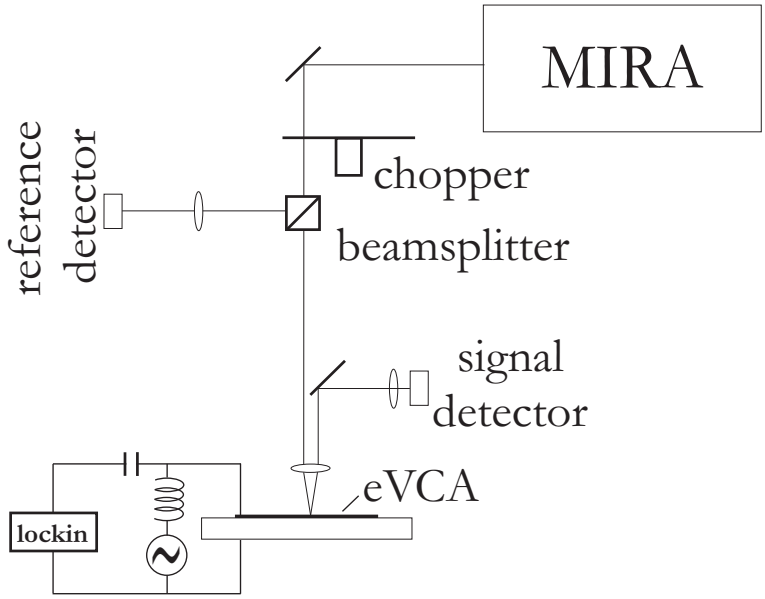

Figure 5.11: The gain measurement setup. The transparency has been measured with a bias-Tee in parallel with the eVCA as illustrated in the figure. The $MIRA$ laser system is operated in CW mode.

The MIRA laser beam is chopped with a frequency of $\sim 1413\ Hz$ and is focused onto the sample under test with a lens with a focal length of

30 mm. The diffraction limit of the spot size diameter with this lens at $960 - 980$ nm with a laser beam of 5 mm is around 14 μm. This means that only eVCAs with aperture diameters larger than this can be tested. In practise, however, some of the laser light will diffract on the surface (e.g. contacts) or on the mesas on the backside of the eVCAs and cause unprecise measurements. The gain was therefore measured on eVCAs with largest available apertures.

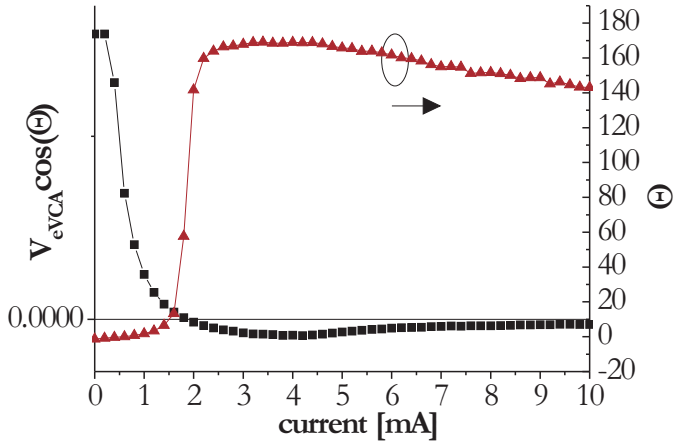

Figure 5.12: The voltage across the eVCA and the phase difference Θ versus the current applied to an IQE eVCA with an aperture diameter of 14 μm.

The reflectivity of an eVCA is equal to

$$R_{eVCA} = R_0 G_{QW} = R_0 e^{gd} \tag{5.1}$$

where R_0 is the reflectivity at transparency of the quantum wells, which is slightly less than 1 due to loss induced in the doped substrate and mirrors. G_{QW} is the gain in the quantum wells and equal to e^{gd}, where g is the gain coefficient in the quantum wells and d the total thickness of the quantum wells. At transparency, the gain G_{QW} is equal to one ($g = 0$), i.e. the reflectivity of the whole structure at transparency is equal to R_0, which is calculated for each structure and listed in table 4.1.

The current density at transparency has been measured by coupling a bias-Tee in parallel with the eVCA, as illustrated in figure 5.11. The chopped input power of the $MIRA$ beam is set to its maximum ($\simeq 20$ mW)

and the voltage across the eVCA is measured versus the current applied to the eVCA via a lock-in amplifier.

When the eVCA is in an absorbing state (i.e. when the injected current is lower than the transparency current, I_{tr}), the MIRA light will generate carriers in the quantum wells, thus increasing the quasi-Fermi levels and increasing the voltage across the eVCA. The voltage across the eVCA will thus increase in phase with the chopped MIRA light. When the current injected in the eVCA is increased above I_{tr}, the eVCA changes from absorbing to amplifying. Above I_{tr}, the voltage across the eVCA decreases in phase with the chopped MIRA light because carriers are removed as the MIRA light is amplified. Around I_{tr}, one will thus expect a phase shift of 180^o in the voltage across the eVCA.

Figure 5.12 shows the phase difference $\Theta = \Theta_{eVCA} - \Theta_{chopper}$ and the voltage across the eVCA (times $cos(\Theta)$), $V_{eVCA} \cdot cos(\Theta)$, versus the injected current in an IQE eVCA with an aperture of 14 μm. The phase difference is set to zero a very low injection currents. At transparency ($\simeq 1.85\ mA$), the phase difference changes sign from 0 to around 180^o according to a change in the state of the eVCA from absorbing to amplifying.

At high injection currents, the modulation of the voltage across the eVCA due to the chopped MIRA light becomes negligible compared to the voltage induced by the current injected in to the eVCA, and the $V_{eVCA}cos(\Theta)$ goes to zero.

The transparency measurements of different IQE and TAIWAN samples are shown in figure 5.13. Most eVCAs have a current density of $\simeq 1000\ A/cm^2$ (for small apertures) to $\simeq 100\ A/cm^2$ (large apertures) at transparency.

Two of the TAIWAN samples (sample 2 (40 μm) and sample 10 (50 μm)) have suspiciously high current densities at transparency which might be an indication of a high leak of current in the devices. We do not know where-from this leak current origins. Sample 10 has a very high transparency current of $42 - 48\ mA$. Sample 10 has no etched mesas on the p-side, so its aperture is effectively larger than 50 μm due to diffusion of holes in the p-DBR, however, not enough to account for this high transparency current density. Sample number 2 was ultrasonically cleaned in 15 s in order to enhance the lift-off of the n-contact and it might have led to damage of the device. However, sample number 13 (30 μm) was also ultrasonically cleaned but still has a very low transparency current density ($200\ A/cm^2$).

The transparency current is also measured in one ORC eVCA, even though it has defects in the crystal. The transparency current of an ORC eVCA with an aperture diameter of 80 μm is $\sim 100\ mA$, i.e. a current

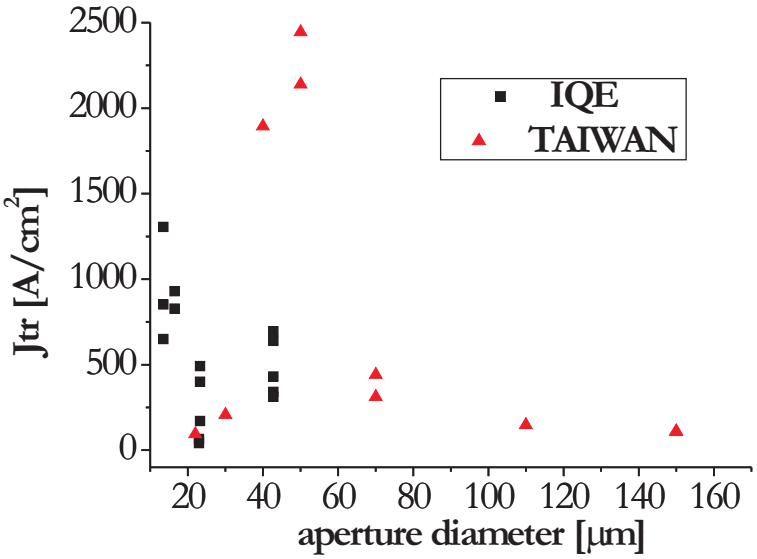

Figure 5.13: Current densities at transparency for 5 different IQE samples (apertures from 13 to 42 μm) and 7 different TAIWAN samples. (apertures from 22 to 150 μm)

density of $\sim 2000\ A/cm^2$. The high transparency current is probably due to the defects in the structure which are known to disseminate vertically in the structure and consume many carriers.

5.3.1 Reflectivity of IQE and TAIWAN structures

Since it was clear very early in the testing of the IQE structures that the current spreading cannot support aperture diameters larger than $\sim 25\ \mu m$, only very few samples with aperture diameters larger than $15 - 20\ \mu m$ have been processed. The reflectivity of an IQE eVCA with an aperture diameter of 43 μm and a transparency current of $\sim 5\ mA$ has been measured, and the results are shown in figure 5.14. The graph contains curves recorded from two successive days. A maximum reflectivity of 1.087, i.e. a net gain of ~ 8.7 % is recorded at three different MIRA signal powers, and this corresponds to a gain coefficient in the quantum wells of $\sim 2650\ cm^{-1}$. A maximum gain of ~ 9 % is also measured on an eVCA with an aperture diameter of 23 μm, however, the maximum gain fluctuated a lot as the signal

power is increased, so we speculate that the measurements are influenced by reflections of the signal on e.g. the top-contacts of the device.

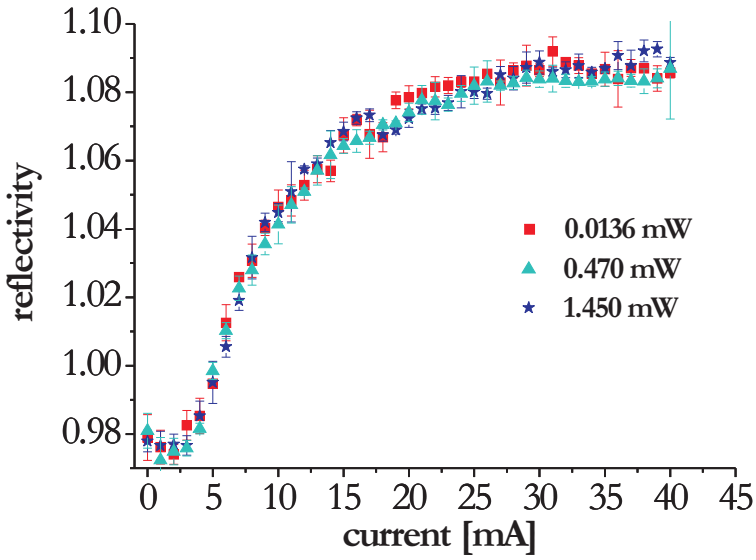

Figure 5.14: Reflectivity of an IQE eVCA with an aperture diameter of 43 μm. A gain of ~ 8.7 % is recorded at three different MIRA signal powers, 0.0136, 0.470 and 1.450 mW.

The gain has similarly been measured on two different eVCAs on the TAIWAN sample number 16, both with an aperture diameter of 150 μm. The eVCAs have transparency currents of 17 mA and 21 mA, and the reflectivities are shown in figure 5.15. The curves on the bottom graph have been measured on two different days.

Since the cavity dip of this device is located at around 970 nm, one of the curves in the bottom graph is measured with a $MIRA$ wavelength of 970 nm and with the eVCA heated to 35 ^oC. There is, however, no significant difference in the measured reflectivity under these circumstances compared with the measurements performed at 960 nm and 20 ^oC.

The measurements show no net gain in the structure. A net reflectivity at 960 nm of 95 % corresponds to a gain coefficient in the quantum wells of ~ 1900 cm^{-1} assuming a correction of layer 8 and 16 in the recipe of the TAIWAN structure as discussed in section 5.2.3.

The results are summarised in table 5.2. The two TAIWAN sam-

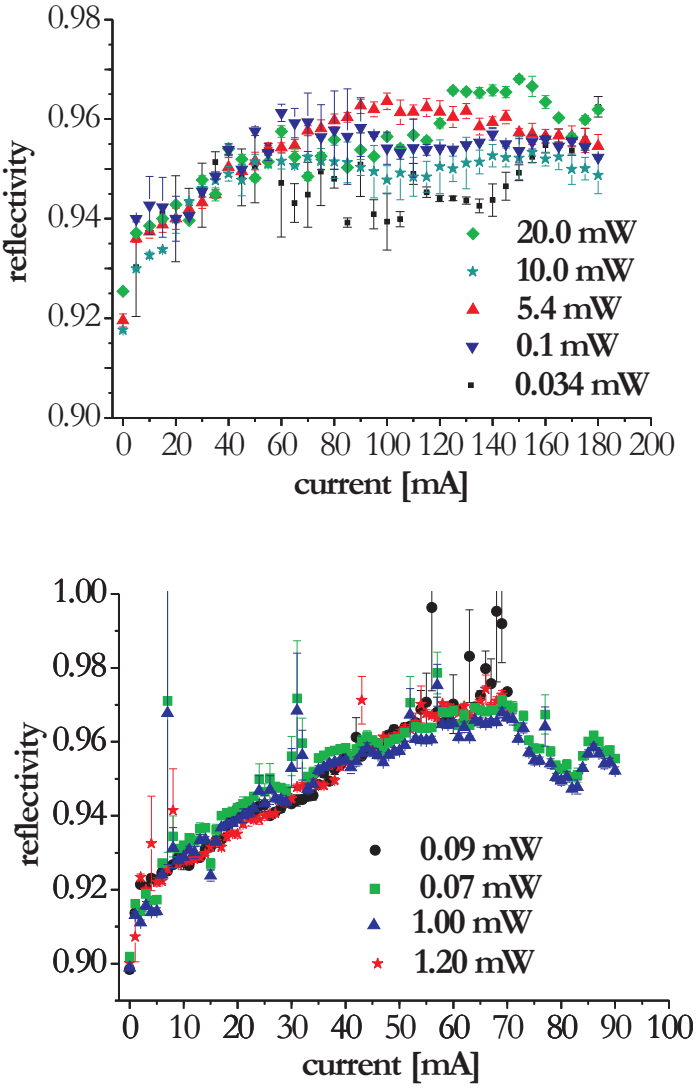

Figure 5.15: Reflectivity of two different TAIWAN eVCAs with aperture diameters of 150 μm. The top graph is measured on an eVCA with a transparency current of 17 mA, whereas the bottom graph is measured on an eVCA with a transparency current 21 mA. One of the curves (red $\triangle$) on the bottom graph is measured at a sample temperature of 35^oC at a MIRA wavelength of $970nm$.

ples with suspiciously high current densities at transparency have been neglected.

sample name	J_{tr} $[A/cm^2]$	maximum $R_{structure}$	g in QWs $[cm^{-1}]$	theory $[cm^{-1}]$
IQE	4-1300	1.087	2650	2700
TAIWAN	100-500	0.96	1900	4600

Table 5.2: Threshold current densities at transparency, the maximum reflectivity of the structures and corresponding gain coefficient in the quantum wells versus the theoretical values from the *SILVACO* simulations from chapter 3.

5.3.2 Discussion

The gain in the TAIWAN quantum wells is very small compared to the gain in the IQE quantum wells, and the results disagree with the simulations of the gain coefficient presented in section 3.4 which predicted a gain of $\sim 4600\ cm^{-1}$ in $InGaAs$ quantum wells with $AlGaAs$ barriers. The simulations also predicted a gain of $\sim 2700\ cm^{-1}$ in the $InGaAs$ quantum wells with $GaAsP$ barriers (similar to the IQE structure) which is in good agreement with the measured value.

The small gain coefficient in the TAIWAN structures can be explained by less perfect interfaces in the structure which can induce smaller reflectivity at 960 nm. Another possibility is that the eVCAs have been destroyed during processing, even though I find it difficult to identify exactly which steps might have caused the destruction. Finally, the calculations of the gain coefficient in the quantum wells are based on *assumptions* of a change in the structure design in layer 8 and 16 as discussed in section 5.2.3, because the final structure growth is confidential. In addition, LandMark might have changed the doping level of the substrate from $2 \cdot 10^{18}\ cm^{-3}$ to $3 \cdot 10^{18}\ cm^{-3}$; such a change would mean that the gain in the quantum wells is as high as $\sim 4500\ cm^{-1}$. Unfortunately, we currently have no equipment to measure the exact doping level of the substrate.

The gain in the TAIWAN eVCA is the same at 970 nm, even when the structure is heated to 35 ^oC. According to MATLAB calculations based on the Vaarshni relation [81] and parameters given by [82], a temperature increase of 15 ^oC should increase the optical transition in the quantum wells $\sim 5\ nm$, i.e. enough to detect an increase in the gain as the optical transition is thus closer to the cavity dip of 975 nm. However, this heating will also influence the gain in negative manners, such as a broadening of the

Fermi distribution, that again lowers the efficiency of the quantum wells. This might explain why no difference is observed in the measurements of the gain as the temperature is increased.

As the TAIWAN eVCAs with aperture diameters of 40 μm and 70 μm according to figure 5.10 have much higher maximum output power densities, one could speculate that also the gain is higher in these devices compared to the 150 μm aperture device. The emitted power density of TAIWAN eVCAs with small aperture diameters is around a factor of 5 larger than the emitted power density of TAIWAN eVCAs with large aperture diameters. The gain coefficient in the TAIWAN eVCAs with small apertures might therefore be closer to the estimated gain coefficient calculated by the $SILVACO$ simulations. Assuming a spontaneous emission rate linear with the carrier density [123], N, the average (over the aperture area) carrier density in the TAIWAN eVCAs with small apertures are thus 5 times larger than the average carrier density in the TAIWAN eVCAs with large apertures. A rough estimate on the gain coefficient due to a five times larger carrier density using equation 3.15 gives 3228 cm^{-1} assuming a g_0 of the TAIWAN quantum wells of 825 cm^{-1} and a transparency carrier density of 10^{18} cm^{-3}.

No gain saturation has been observed in any of the structures. The gain saturation powers of the IQE and TAIWAN structures have been calculated by the model presented in section 3.10 and appendix B.

For the bottom-emitting TAIWAN eVCA, the gain saturation power is calculated for a device without substrate. The reflectivity of the TAIWAN structure without substrate and with a gain coefficient of 1900 cm^{-1} is calculated to 1.020. The reflectivity of the IQE eVCA was measured to 1.087.

The gain saturation power depends on the current injected to the eVCAs, I. The injected current, I, is set so that the reflectivities of the structures at small external signal powers are equal to the measured reflectivity (IQE) and calculated reflectivity (TAIWAN).

The resulting gain saturation powers of the two structures are presented in table 5.3. The most right coloumn list the gain saturation fluence.

Since the loss in the substrate is not included in these calculations, the listed gain saturation power of the TAIWAN eVCA in table 5.3 should be multiplied with a factor of e^{-at}, where a is the absorption coefficient of the substrate (6 cm^{-1} in a substrate n-doped with $2 \cdot 10^{18}$ cm^{-3}) and t the thickness of the substrate.

The reflectivity of a correctly grown TAIWAN eVCA without substrate and with a gain-coefficient of 1900 cm^{-1} is calculated to 1.065. Such a

name	reflectivity	aperture diameter $[\mu m]$	P_{sat} $[W]$	F_{sat} $[kW/cm^2]$
IQE	1.087	43	3.77	260
TAIWAN	1.020	150	0.391	2.21

Table 5.3: Measured (IQE) and calculated (TAIWAN) small-signal reflectivities and gain saturation powers of the IQE and TAIWAN structures. The aperture diameter of the IQE and TAIWAN eVCAs are 43 μm^2 and 150 μm^2, which gives the gain saturation fluences (in units of W/cm^2) as listed to the right.

structure with an aperture diameter of 150 μm would have a gain saturation fluence of 7.30 kW/cm^2.

The pulse energy, $E_{sat,0.9}$, where the total reflectivity, R_G, has decreased by 10 % has been calculated for the IQE and the TAIWAN eVCAs at a current density of 10^{19} cm^{-3} where the gain coefficient of the eVCAs are 2650 cm^{-1} and 1900 cm^{-1} respectively. The results are listed in table 5.4.

name	aperture diameter $[\mu m]$	$E_{sat,0.9}$ $[nJ]$	$F_{sat,0.9}$ $[\mu J/cm^2]$
IQE	43	2.15	148
TAIWAN	150	3.50	19.8

Table 5.4: Calculated pulse energies where the total gain of the IQE and TAIWAN eVCAs have saturated by 10 % and corresponding fluences.

Assuming a reflectivity saturation of 10 %, the intra-cavity power in a VECSEL with the IQE eVCA is thus limited to 2.15 W at 1 GHz and 3.50 W at 1 GHz for a VECSEL with a TAIWAN eVCA.

The rise of the reflectivity versus the injected current is very different in the three curves presented. This rise is equal to the differential reflectivity in the structures, and is estimated around transparency to $\frac{dR}{dI} \simeq 14 \cdot 10^{-3}$ mA^{-1} in the IQE eVCA and only $\simeq 0.3 - 0.8 \cdot 10^{-3}$ mA^{-1} in the TAIWAN eVCAs, i.e. more than ten times higher in the IQE eVCAs. This difference is attributed the difference in the aperture diameter of the two eVCAs.

The decrease in the reflectivity of the IQE eVCA from $0 - 1$ mA can be due to a larger free carrier loss in the structure at 1 mA than at 0 mA.

5.4 VECSEL with IQE eVCA

Some of the IQE eVCAs have been set up in an external cavity. The IQE eVCAs with small apertures are very easy to set to lase in an external cavity, especially in the collimated and the concave mirror cavities, figure 5.16, where the lens or the external mirror are close to the eVCA.

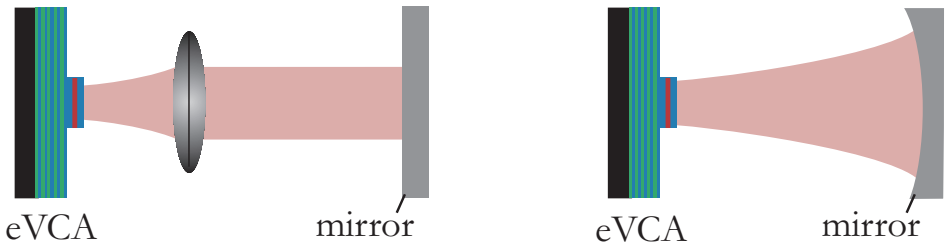

Figure 5.16: Two types of linear VECSELs; collimated cavity (left) and concave mirror cavity (right).

5.4.1 Concave mirror cavities

Figure 5.17 shows the output power from three laser cavities with curved mirrors. The output power is measured in laser cavities of three different lengths, ~ 10, ~ 20 and $\sim 10\ mm$, determined by the radius of curvature of the curved mirror. The curved mirrors have a reflectivity of 97 %. Two IQE eVCAs with aperture diameters of 12 and 23 μm have been tested, and the devices have been cooled to $\sim 20\ ^oC$ during characterisation.

The maximum output power of 1.6 mW is obtained with an eVCA with an aperture diameter of 12 μm in the cavities of lengths ~ 10 and $\sim 50\ mm$. The eVCA with an aperture diameter of 23 μm gave a slightly smaller maximum output power of $\sim 1.4\ mW$. A similar laser cavity with an eVCA with an aperture diameter of 50 μm gave a maximum output power of 0.32 mW in a $\sim 10\ mm$ cavity.

The output modes for all above-mentioned laser cavities are transversal multi mode. The maximum single mode output power of the eVCA with an aperture of 12 μm is recorded to $\sim 0.55\ mW$ in a short cavity (and less in larger cavities). The results are summarised in table 5.5 together with the intra-cavity powers, P_{intra}, of the external lasers and the differential output power, dP/dI, of the VECSELs.

The dP/dI falls off for a VECSEL with an eVCA with a large aperture, again indicating a lack of current spreading in large apertures of the IQE

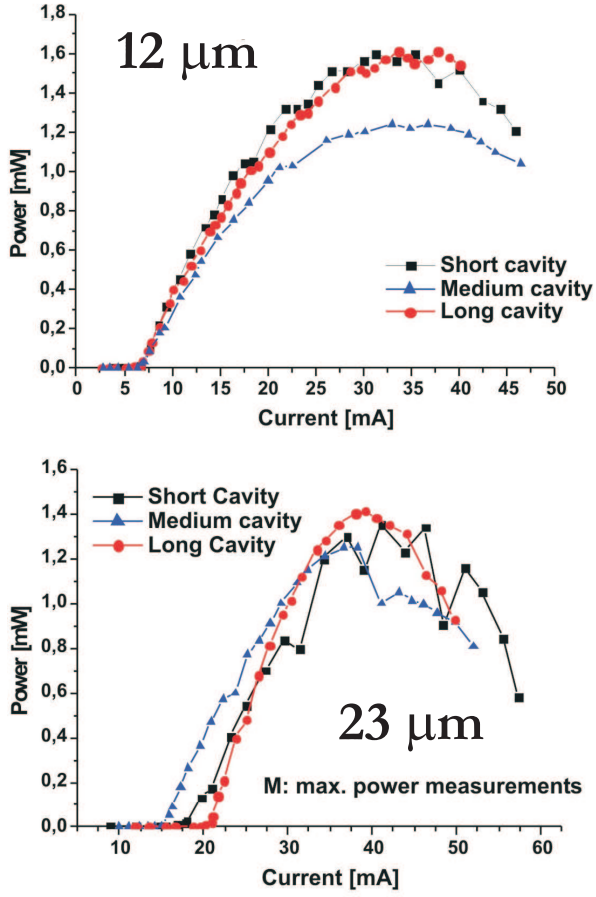

Figure 5.17: *PI*-curves of three different cavities; short ($\sim 10\ mm$), medium ($\sim 20\ mm$) and long ($\sim 50\ mm$) for two IQE eVCAs with aperture diameters of 12 μm (IQE C, top) and 23 μm (IQE M, bottom). Measurements performed by Kirsten E. Moselund [124]

eVCA. The values of the multi mode VECSELs with eVCAs with aperture diameters of 12 and 23 μm are extracted from figure 5.17. The remaining values are extracted from other graphs not included in this thesis but presented in [124].

5.4.2 Discussions

The intra-cavity power of the single-mode VECSEL is up to 18 mW with an IQE eVCA with an aperture diameter of 12 μm. Based on this intra-

aperture diameters $[\mu m]$	P_{max} $[mW]$	P_{intra} $[mW]$	J_{thr} $[A/cm^2]$	dP/dI $[W/A]$
$12\mu m$, multi mode	1.2-1.6	40.0-53.3	~ 6000	0.084
$12\mu m$, single mode	0.55	18	~ 6000	0.025
$23\mu m$, multi mode	1.2-1.4	40.0-46.7	3600-5200	0.080
$50\mu m$, multi mode	0.20-0.32	6.7-10.6	1900-2800	0.016

Table 5.5: The maximum output powers, the maximum intra-cavity powers, the threshold current densities, dP/dI, of external cavities with IQE eVCAs with aperture diameters of 12, 23 and 50 μm.

cavity power, the ability of this IQE eVCA in a mode-locked laser cavity can be estimated. The electrically pumped linear cavity mode-locked laser presented by Zhang *et al.* [24] consists of a gain section with an aperture diameter of 150 μm optically connected to an absorber with a saturation fluence of $F_{sat} \sim 76\ \mu J/cm^2$ via a lens of 2.5 mm in diameter and 1.6 mm in focal length. The laser cavity is illustrated in figure 5.18. The mode-locked laser has a repetition rate of $\sim 6\ GHz$, corresponding to a cavity length of $s + s' \simeq 2.5\ cm$. The laser beam is coupled out via the DBR on the absorber section which has an output coupling of 8 %. We would like to estimate how an IQE eVCA would work in the same laser cavity as the one described above.

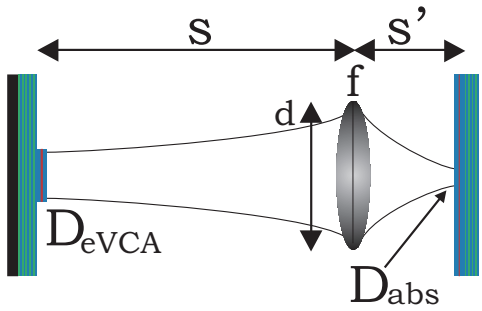

Figure 5.18: The linear cavity of Zhang *et al.* [24].

In order to estimate the abilities of the IQE eVCAs based on the CW results of previous section, we define the pulse fluence (in units of $\mu J/cm^2$) on the absorber of a mode-locked laser to the intra cavity power, P_{intra} divided by the area on the absorber, A_{abs}, times the round trip time of the laser cavity, τ_R:

$$F_p = \frac{P_{intra}}{A_{abs}} \tau_R \tag{5.2}$$

This equation is valid as long as the recovery time of the absorber, τ_A, is shorter or comparable to the round trip time of the laser cavity, τ_R.

The repetition rate and the pulse fluence of a mode-locked VECSEL in a cavity as in figure 5.18 with an eVCA with an aperture diameter of 12 μm has been calculated by the above equation 5.2. The figure 5.19 shows the repetition rate in units of GHz and the saturation fluence in units of $\mu J/cm^2$ versus the distance between the eVCAs and the lens, s, in units of mm. In order to make a safe estimate, the calculations assumes a intra-cavity power of only 9 mW, i.e. half the CW intra-cavity power. The cavity is limited at large s due to the diffraction limit of the lens.

When s is increased, $s + s'$ increases and the repetition rate thus decreases. As s increases, the beam spot size on the absorber decreases, thus increasing the fluence on the absorber.

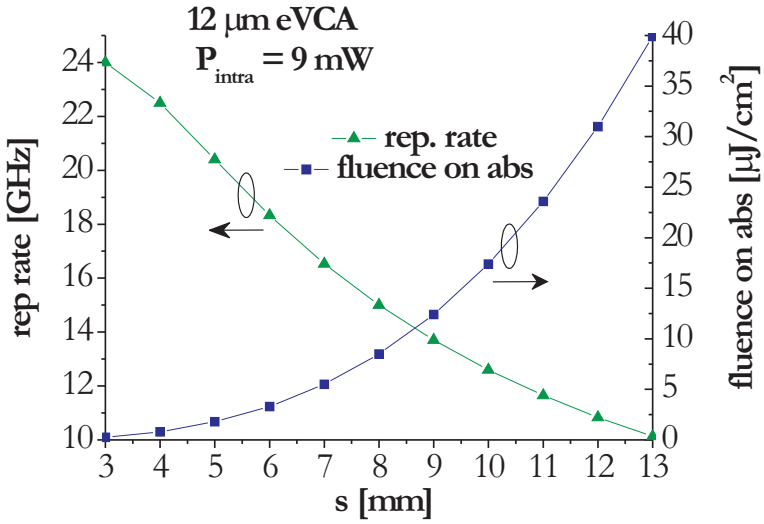

Figure 5.19: The calculated repetition rate and the fluence on the absorber of a IQE eVCAs with aperture diameter of 12 μm and intra-cavity power of 9 mW in a cavity as in figure 5.18.

The pulse fluence increases from ~ 0.3 $\mu J/cm^2$ to ~ 40 $\mu J/cm^2$ when the repetition rate decreases from ~ 23 GHz to ~ 10 GHz.

Assuming the fluence on the absorber should be around a factor of three times larger than the saturation fluence of the absorber [125] and assuming the intra-cavity power of the IQE eVCA in a mode-locked external laser cavity is 9 mW, the IQE eVCA would be able to saturate an absorber with a saturation fluence of 1.1 $\mu J/cm^2$ (presented in [69]) in a linear mode-locked laser similar to that of figure 5.18 with a repetition rate of $\sim 18\ GHz$ and average output power of 270 μW (since the output coupler has a transmittance of 3 %). Again, this estimate assumes an absorber recovery time shorter than the round trip time, which is $\sim 50\ ps$.

A similar calculation has been performed with an intra-cavity power of 400 mW in an eVCA with aperture diameter of 80 μm, i.e. assuming scalability of the output power to aperture area from the 12 μm aperture diameter device to a 80 μm aperture diameter device. The result is presented in figure 5.20.

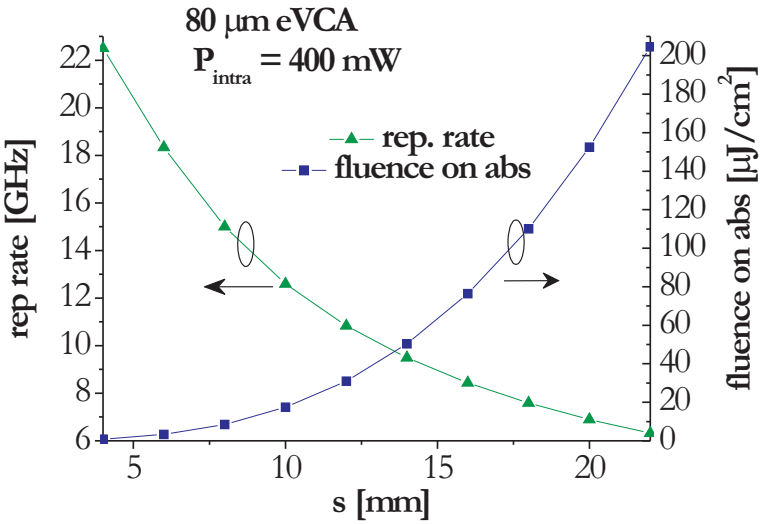

Figure 5.20: The estimated repetition rate and the fluence on the absorber of an eVCA with aperture diameter of 80 μm and intra-cavity power of 300 mW in a cavity as in figure 5.18.

The pulse fluence increases from $\sim 0.8\ \mu J/cm^2$ to $\sim 205\ \mu J/cm^2$ as the repetition rate decreases from $\sim 23\ GHz$ to $\sim 6\ GHz$. The estimate predicts a mode-locked external laser cavity similar to that of figure 5.18 with a repetition rate of $\sim 17\ GHz$ and average output power of 9 mW

(since the output coupler has a transmittance of 3 %). As above, this requires an absorber recovery time faster than ~ 50 *ps*.

Chapter 6

Conclusions and outlook

6.1 Conclusions and outlook

I have investigated, processed and tested new designs of eVCAs for use in compact mode-locked lasers.

Four different eVCA structures have been designed and processed. One of the eVCA structure is a top-emitting structure and the remaining three are all bottom-emitting structures, where light is emitted through the substrate on which the is structure grown.

The top-emitting eVCA does not have a sufficient lateral current spreading to support uniform carrier distribution in aperture diameters larger than $\sim 25\ \mu m$. The top-emitting eVCA is, however, estimated to work in a mode-locked laser with a saturable absorber with low saturation fluence, e.g. a semiconductor quantum-dot based absorber.

Since the doped substrate absorbs the light emitted in the bottom-emitting structures, two of the bottom-emitting eVCAs have an extra DBR on top of the quantum well section in order to enhance the gain in the structure. The top DBR also enhances the lateral current spreading of the devices. However, the enhancement of the gain and current spreading due to the top DBR comes at expense of a higher group delay dispersion and smaller gain bandwidth of the eVCA. The two bottom-emitting eVCAs are found to support aperture diameters up to $\sim 80\ \mu m$, allowing for higher output powers. *The bottom-emitting structures are thus preferable if aperture diameters larger than* $\sim 25\ \mu m$ *are desired.* The third bottom-emitting structure has no top DBR but is supplied with etch-stop layers in order to selectively etch the substrate away. This structure is promising due to its low group delay dispersion and broad gain bandwidth. However, all fully processed eVCAs of this structure show sign of open-circuitry. I believe

that the eVCAs broke during the processing, so efforts have to be made to improve the processing of this structure.

All comparisons between the eVCAs presented in this thesis should be made with caution due to the fact that all four eVCA structures have been grown in four different growth chambers. I would like to stress that the major obstacle and most time-consuming part of this work has been the lack of own growth facilities. It complicates the development of designs due to communication problems and differences in e.g. priorities of the projects, quality of the grown structures and also available materials in the growth facilities of the collaborating institutes or companies.

I have with the *SILVACO* simulations presented a tool for improving the composition and doping levels of the barriers and spacer layers around the quantum wells. The carrier distribution of three quantum well sections have been simulated, all three designs with $InGaAs$ quantum wells. One design is a strain-compensated design with $GaAsP$ barriers, the two other designs have no strain-compensating layers but have barriers of $AlGaAs$ and $GaAs$.

According to these simulations, a design with quantum wells of $InGaAs$, barriers of $AlGaAs$ and spacer layers of $AlGaAs$ seems to perform best in the distribution of carriers in the quantum well section and this design thus has the largest gain coefficient per quantum well of 4600 cm^{-1}.

The two eVCA structures based on the above $InGaAs/AlGaAs$ design, i.e. the TAIWAN and the NBI eVCA, did not bring us closer to an experimental verification of the simulated results. The gain coefficient in the quantum wells of the TAIWAN eVCA is measured to be 1900 cm^{-1}, i.e. much lower than estimated by the simulations. However, due to a misunderstanding between me and the company that grew the TAIWAN structure, the TAIWAN structure was grown incorrectly, and the measured gain coefficients are based on assumptions of *how* the growth of the TAIWAN structure was changed. Had the TAIWAN structure been grown correctly, a gain of or 4600 cm^{-1} in the quantum wells would provide a single pass gain of the structure of 11 % at 960 nm.

A combination of InGaAs quantum wells and AlGaAs barriers is my best suggestion for use in an eVCA structure. However, only three quantum wells of the $InGaAs/AlGaAs$ design can be grown without defects in the structure. *I therefore suggest GaAsP strain-compensating layers in the spacer layers around the quantum well sections in order to increase the number of quantum wells to 9.*

The processing of the eVCAs is described in detail in this thesis. With regards to improvements of the processing, *I suggest that the final samples*

are cleaved into smaller samples than 3 mm × 4 mm, since small samples are easier to silver-glue or solder to carriers. Furthermore, instead of etching mesas into the structures, one can etch ring-shaped grooves in order to confine the carriers on the p-side. In this way, the eVCAs do not rest on the mesas and the contact area between the sample and the carriers is enlarged.

Also, if the samples are cleaved so small that they only contain one active eVCA each, one can avoid the gold-patterned carriers and simply glue or solder the whole p-side area to an electrically conducting carrier. This will enhance the adhesion of the sample to the carrier and prevent breaking of the sample when e.g. the n-contacts are processed.

The NBI-structure (i.e. the bottom-emitting structure without top DBR and with etch-stop layers to remove the substrate) is a very ambitious structure, but the above-mentioned processing adjustments could suffice for the successful realisation of such a device. The structure has a relatively high reflectivity and high gain saturation since it has no top DBR. The structure needs current-spreading layers in order to laterally spread the current to the aperture area. Such layers have been simulated in $SILVACO$ and shown to enhance the lateral current spreading. However, the NBI structure did not allow an experimental verification of the simulations of these current-spreading layers.

The number of periods in the top DBR may be increased to 5.5 in order to ensure a large reflectivity. The TAIWAN structure with 5.5 pairs of top DBR would have a reflectivity of 1.0361, i.e. a single pass gain of 3.6 %, even at a relatively low gain coefficient of 1900 cm^{-1} in the quantum wells.

Alternatively, the absorption of the substrate could be lowered by etching a hole in the substrate on top of the active eVCAs, as illustrated to the right in figure 3.15. The TAIWAN structure with 4.5 pairs of top DBR and a substrate thickness of only 10 μm would have a reflectivity of 1.053, i.e. a single pass gain of 5.3 %, still with a low gain coefficient of only 1900 cm^{-1} in the quantum wells. The group delay dispersion slope of such a structure would be around 750 fs^2/nm. Decreasing the number of top DBR to 3.5 pairs decreases the reflectivity to 1.033 and the group delay dispersion slope to 225 fs^2/nm.

I therefore suggest that the next sample investigated should be similar to the TAIWAN structure with modified strain-compensating spacer layers and an increased number of quantum wells. The number of top DBR pairs can be adjusted to fit to the external mirror reflectivity and the wished gain saturation. Partial removal of the substrate should be investigated and performed in order to minimise the number of top DBR pairs.

With regard to the characterisation of the eVCAs, the transparency measurements showed to be an easy way to test the eVCAs, and I *suggest these measurements to be done as one of the first characterisations of the eVCAs along with simple PI and IV characteristics. The measurements of the reflectivity versus the injection current in the eVCA can be performed on selected eVCAs that are planned to be used in VECSELs.* In order to measure the gain saturation power and pulse energies and thus verify the calculations presented in this thesis, a stable CW or mode-locked laser system with a much higher output power (up to 3 W) at 960-980 nm would be required.

Bibliography

[1] H. Soda, K. Iga, C. Kitahara, and Y. Suematsu. GaInAsP/InP Surface Emitting Injection Lasers. *Jpn. Journ. Appl. Phys.*, 18(12):2329–2330, 1979.

[2] H. Q. Le, S. Di Cecca, and A. Mooradian. Scalable high-power optically pumped *GaAs* laser. *Appl. Phys. Lett.*, 58(18):1967–1969, 1991.

[3] J. P. Zhang. Single mode power and modal behaviour in buried vertical-cavity surface-emitting lasers. *IEE Proc.-Optoelectron.*, 142(2):87–93, 1995.

[4] A. Furukawa, S. Sasaki, M. Hoshi, A. Matsuzono, K. Moritoh, and T. Babab. High-power single-mode vertical-cavity surface-emitting lasers with triangular holey structure. *Appl. Phys. Lett.*, 85(22):5161–5163, 2004.

[5] K. J. Ebeling. *Analysis of vertical cavity surface emitting laser diodes (VCSELs).* Scottish Universities Summer School in Physics & IOP, 1999.

[6] D. Birkedal, S. Bischoff, F. Romstad, M. Madsen, and J. Ostergaard. Photonic bandgap VCSELs. *Conference on Lasers and Electro-Optics, 2004. (CLEO)*, 1, 2004.

[7] Å. Haglund, S. J. Gustavsson, J. Vukušić, P. Jedrasik, and A. Larsson. High-power fundamental-mode and polarisation stabilised VCSELs using sub-wavelength surface grating. *Electr. Lett.*, 41(14), 2005.

[8] G. A. Keeler, D. K. Serkland, K. M. Geib, G. M. Peake, and A. Mar. Single Transverse Mode Operation of Electrically Pumped Vertical-External-Cavity Surface-Emitting Lasers With Micromirrors. *IEEE Photon. Techn. Lett.*, 17(3):522–524, 2005.

[9] B. Kögel, M. Mautea, H. Halbritter, S. Jatta, G. Böhm, M. C. Amann, and P. Meissner. High singlemode output power from long-wavelength VCSELs using curved micromirrors for mode control. *Electr. Lett.*, 41(17), 2005.

[10] K. J. Ebeling, U. Fiedler, R. Michalzik, G. Reiner, and B. Weigl. Recent advances in semiconduct or vertical cavity lasers for optical communications and optical interconnects. *22nd European Conference on Optical Commurication*, 2:81–88, 1996.

[11] M. Kuznetsov, F. Hakimi, R. Sprague, and A. Mooradian. High-Power (¿0.5 − W CW) Diode-Pumped Vertical-External-Cavity Surface-Emitting Semiconductor Lasers with Circular TEM Beams. *IEEE Photon. Techn. Lett.*, 9(8):1063–1065, 1997.

[12] H. A. Haus. Mode-Locking of Lasers. *IEEE Journ. Select. Top. Quant. Electr.*, 6(6):1173–1185, 2000.

[13] L. E. Hargrove, R. L. Fork, and M. A. Pollack. Locking of He-Ne Laser Modes Induced by Synchronnous Intracavity Modulation. *Appl. Phys. Lett.*, 5(1):4–5, 1964.

[14] H. W. Mocker and R. J. Collins. Mode Competition and Self-Locking Effects in a Q-switched Ruby Laser. *Appl. Phys. Lett.*, 7(10):270–273, 1965.

[15] E. P. Ippen, C. V. Shank, and A. Dienes. Passive mode locking of the cw dye laser. *Appl. Phys. Lett.*, 21(8):348–350, 1972.

[16] O. E. Martinez, R. L. Fork, and J. P. Gordon. Theory of passively mode-locked lasers for the case of a nonlinear complex-propagation coefficient. *Journ. Opt. Soc. Am. B*, 2(5):753–760, 1985.

[17] F. X. Kärtner, I. D. Jung, and U. Keller. Soliton Mode-Locking with Saturable Absorbers. *IEEE Journ. of Sel. Topics in Quant. Electr.*, 2(3):540–555, 1996.

[18] P. T. Ho, L. A. Glasser, E. P. Ippen, and H. A. Haus. Picosecond pulse generation with a cw GaAlAs laser diode. *Appl. Phys. Lett.*, 33(3):241–242, 1978.

[19] E. P. Ippen, D. J. Eilenberger, and R. W. Dixon. Picosecond pulse generation by passive modelocking of diode lasers. *Appl. Phys. Lett.*, 37(3):267–269, 1980.

[20] S. Hoogland, S. Dhanjal, A. C. Tropper, J. S. Roberts, R. Häring, R. Paschotta, F. Morier-Genoud, and U. Keller. Passively Mode-Locked Diode-Pumped Surface-Emitting Semiconductor Laser. *IEEE Photon. Techn. Lett.*, 12(9):1135–1137, 2000.

[21] R. Häring, R. Paschotta, F. Morier-Genoud, U. Keller, A. Garnache, U. Oesterle, J. S. Roberts, S. Hoogland, S. Dhanjal, and A. C. Tropper. Passively mode-locked diode-pumped surface-emitting semiconductor laser. *Conference on Lasers and Electro-Optics (CLEO 2000)*, pages 97–98, 2000.

[22] R. Häring, R. Paschotta, E. Gini, F. Morier-Genoud, D. Martin, H. Melchior, and U. Keller. Picoseond surface-emitting semiconductor laser with ¿ 200mW average power. *Electr. Lett.*, 37(12):766–767, 2001.

[23] A. Garnache, S. Hoogland, A. C. Tropper, I. Sagnes, G. Saint-Girons, and J. S. Roberts. ¡500-fs Soliton Pulse in a Passively Mode-locked Surface-emitting Laser with 100-mW Average Power. *Lasers and Electro-Optics (CLEO 2002)*, pages 586–587, 2002.

[24] Q. Zhang, K. Jasim, A. V. Nurmikko, A. Mooradian, G. Carey, W. Ha, and E. Ippen. Operation of a Passively Mode-Locked Extended-Cavity Surface-Emitting Diode Laser in Multi-GHz Regime. *IEEE Photon. Techn. Lett.*, 16(3):885–887, 2004.

[25] A. Aschwanden, D. Lorenser, H. J. Unold, R. Paschotta, E. Gini, and U. Keller. 10 GHz passively mode-locked external-cavity semiconductor laser with 1.4 W average output power. *Appl. Phys. Lett.*, 86(13):131102, 2005.

[26] W. Jiang, M. Shimizu, R. P. Mirin, T. E. Reynolds, and J. E. Bowers. Electrically pumped mode-locked vertical-cavity semiconductor lasers. *OPTICS LETTERS*, 18(22):1937–1939, 1993.

[27] U. Keller, K. J. Weingarten, F. X. Kärtner, D. Kopf, B. Braun, I. D. Jung, R. Fluck, C. Hönninger, N. Manutschek, and J. Aus der Au. Semiconductor Saturable Absorber Mirrors (SESAM's) for Femtosecond to Nanosecond Pulse Generation in Solid-State Lasers. *IEEE Journ. of Sel. Topics in Quant. Electr.*, 2:012711, 1996.

[28] K. Jasim, Q. Zhang, A. V. Nurmikko, A. Mooradian, G. Carey, W. Ha, and E. Ippen. Passively mode-locked vertical extended cavity surface emitting diode laser. *Electr. Lett.*, 39(4):373–374, 2003.

[29] K. Jasim, Q. Zhang, A. V. Nurmikko, E. Ippen, A. Mooradian, G. Carey, and W. Ha. Picosecond pulse generation from passively modelocked vertical cavity diode laser at up to 15GHz pulse repetition rate. *Electr. Lett.*, 40(1):34–35, 2004.

[30] L. Krainer, R. Paschotta, G.J. Sphler, M. Moser, and U. Keller. 29GHz modelocked miniature $Nd : YVO_4$ laser. *ELECTRONICS LETTERS*, 35(14):1160–1161, 1999.

[31] R. Paschotta, L. Krainer, S. Lecomte, G. J. Spühler, S. C. Zeller, A. Aschwanden, D. Lorenser, H. J. Unold, K. J. Weingarten, and U. Keller. Picosecond pulse sources with multi-GHz repetition rates and high output power. *New Journal of Physics*, 6:174, 2004.

[32] L. Krainer, D. Nodop, G. J. Sphler, S. Lecomte, M. Golling, R. Paschotta, D. Ebling, T. Ohgoh, T. Hayakawa, K. J. Weingarten, and U. Keller. Compact 10-GHz $Nd : GdVO_4$ laser with 0.5-W average output power and low timing jitter. *OPTICS LETTERS*, 29(22):2629–2631, 2004.

[33] G. Lin, H. Wei, Z. Hong-bo, S. Zhi-pei, D. Cui, X. Zu-yan, W. Yong-Gang, and M. Xiao-Yu. Diode-end-pumped passively mode-locked ceramic Nd:YAG laser with a semiconductor saturable mirror. *OPTICS EXPRESS*, 13(11):4085–4089, 2005.

[34] C. Hönninger, R. Paschotta, F. Morier-Genoud, M. Moser, and U. Keller. Q-switching stability limits of continuous-wave passive mode locking. *J. Opt. Soc. Am. B*, 16(1):46–56, 1999.

[35] U. Keller and A. C. Tropper. Passively modelocked surface-emitting semiconductor lasers. *Physics Reports 429 (2006) 67 120*, 429:67–120, 2006.

[36] D. A. Yanson, M. W. Street, S. D. McDougall, I. G. Thayne, J. H. Marsh, and E. A. Avrutinb). Terahertz repetition frequencies from harmonic mode-locked monolithic compound-cavity laser diodes. *Appl. Phys. Lett.*, 78(23):3571–3573, 2001.

[37] S. Arahira, Y. Matsui, and Y. Ogawa. Mode-Locking at Very High Repetition Rates More than Terahertz in Passively Mode-Locked Distributed-Bragg-Reflector Laser Diodes. *IEEE Journ. Quant. Electr.*, 12(7):1211–1224, 1996.

[38] K. Yvind, D. Larsson, L. J. Christiansen, C. Angelo, L. K. Oxenlowe, J. Mork, D. Birkedal, J. M. Hvam, and J. Hanberg. Low-jitter and high-power 40-ghz all-active mode-locked lasers. *IEEE Photon. Tech. Lett.*, 16(4):975–977, 2004.

[39] H. A. Haus. Shape of Passively Mode-Locked Laser Pulses. *Optics Communications*, 15(1):29–31, 1975.

[40] M. Bahl, H. Rao, N. C. Panoiu, and Jr. R. M. Osgood. Simulation of mode-locked surface-emitting lasers through a finite-difference time-domain algorithm. *Optics Letters*, 29(14):1689–1691, 2004.

[41] J. Mulet and S. Balle. Mode-Locking Dynamics in Electrically Driven Vertical-External-Cavity Surface-Emitting Lasers. *IEEE Journ. Quant. Electr.*, 41(9):1148–1156, 2005.

[42] P. F. Moulton, K. J. Snell, K. F. Wall, and R. Bergstedt. High-power RGB laser source for displays. *IMAGE Conference*, from http://www.qpeak.com/, 2002.

[43] F. Brunner, E. Innerhofer, S. V. Marchese, T. Suüdmeyer, R. Paschotta, T. Usami, H. Ito, S. Kurimura, K. Kitamura, G. Arisholm, and U. Keller. Powerful red-green-blue laser source pumped with a mode-locked thin disk laser. *OPTICS LETTERS*, 29(16):1921–1923, 2004.

[44] U. Keller. High power modelocked lasers. *Conference paper, Conference on Lasers and Electro-Optics*, pages 43–45, 2005.

[45] J. P. Watson, J. G. McInerney, A. Mooradian, A. Lewis, A. V. Shchegrov, E. M. Strzelecka, D. Lee, A. Umbrasas, G. P. Carey, B. D. Cantos, W. R. Hitchens, V. V. Doan, C. Amsden, and M. Liebman. Compact, efficient visible lasers based on extended cavity surface-emitting lasers. *Proceedings of SPIE - The International Society for Optical Engineering*, 4967:164–171, 2003.

[46] A.V. Shchegrov, J. P. Watson, D. Lee, A. Umbrasas, S. Hallstein, G. P. Carey, W. R. Hitchens, K. Scholz, B. D. Cantos, G. Niven, M. Jansen, J.-M. Pelaprat, and A. Mooradian. Development of compact blue-green lasers for projection display based on novalux extended-cavity surface emitting laser technology. *Progress in Biomedical Optics and Imaging - Proceedings of SPIE*, 5737:113–119, 2005.

[47] E. M. Strzelecka, J. G. McInerneya, A. Mooradian, A. Lewis, A. V. Shchegrov, D. Lee, J. P. Watson, K. W. Kennedy, G. P. Carey, H. Zhou, W. Ha, B. D. Cantos, W. R. Hitchens, D. L. Heald, V. V. Doan, and K. L. Learb. High power, high brightness 980 nm lasers based on the extended cavity surface emitting lasers concept. *proceedings of SPIE*, 4993:57–67, 2003.

[48] J. Michel. Flashlamp pumped dye laser (585nm, low fluence) for aesthetic and medical indications: Own experience/results and review of literature. *Medical Laser Application*, 20:77–83, 2005.

[49] H. Horch and H. Deppe. New aspects of lasers in oral and craniomaxillofacial surgery. *Medical Laser Application*, 20:7–11, 2005.

[50] R.I. Siphanto, K.K. Thumma, R.G.M. Kolkman, T.G. van Leeuwen, F.F.M. de Mul, J.W. van Neck, L.N.A. van Adrichem, and W. Steenbergen. Serial noninvasive photoacoustic imaging of neovascularization in tumor angiogenesis. *OPTICS EXPRESS*, 13(1), 2005.

[51] S. Valette, P. Steyer, L. Richard, B. Forest, C. Donnet, and E. Audouard. Influence of femtosecond laser marking on the corrosion resistance of stainless steels. *Applied Surface Science*, 252:46964701, 2006.

[52] D. A. B. Miller. Optics for low-energy communication inside digital processors: quantum detectors, sources, and modulators as efficient impedance converters. *OPTICS LETTERS*, 14(2):146–148, 1989.

[53] M. J. Kobrinsky, B. A. Block, J. Zheng, B. C. Barnett, E. Mohammed, M. Reshotko, F. Robertson, S. List, I. Young, and K. Cadien. On-chip optical interconnects. *Intel Technology Journal*, 8(2), 2004.

[54] S. Bigo, O. Leclerc, and E. Desurvire. All-optical fiber signal processing and regeneration for soliton communications. *IEEE Journ. Select. Topics Quant. Electr.*, 3(5):1208–1223, 1997.

[55] A.E. Siegman. *Lasers*. University Science Books, 1986.

[56] J. Diels and W. Rudolph. *Ultrafast Laser Pulse Phenomena, Fundamentals, Techniques, and applications on a femtosecond time sacle*. Optics and Photonics, Academic Press, 1996.

[57] R. Paschotta, R. Häring, A. Garnache, S. Hoogland, A. C. Tropper, and U. Keller. Soliton-like pulse-shaping mechanism in passively mode-locked surface-emitting semiconductor lasers. *Appl. Phys. B*, 75:445–451, 2002.

[58] S. N. Tandon, J. T. Gopinath, H. M. Shen, G. S. Petrich, L. A. Kolodziejski, F. X. Kärtner, and E. P. Ippen. Large-area broadband saturable Bragg reflectors by use of oxidized AlAs. *Optics Letters*, 29(21):2551–2553, 2004.

[59] G. Stibenz, G. Steinmeyer, and W. Richter. Dynamic spectral interferometry for measuring the nonlinear amplitude and phase response of a saturable absorber mirror. *Appl. Phys. Lett.*, 86:081105–1 – 081105–3, 2005.

[60] L. A. Coldren and S. W. Corzine. *Diode Lasers and Photonic Integrated Circuits*. Wiley Series in Microwave and Optical Engineering, 1995.

[61] R. Grange, M. Haiml, R. Paschotta, G. J. Spühler, L. Krainer, M. Golling, O. Ostinelli, and U. Keller. New regime of inverse saturable absorption for self-stabilizing passively mode-locked lasers. *Appl. Phys. B*, 80:151–158, 2005.

[62] M. Haiml, R. Grange, and U. Keller. Optical characterization of semiconductor saturable absorbers. *Appl. Phys. B*, 79:331–339, 2004.

[63] E. W. Van Stryland, M. A. Woodall, H. Vanherzeele, and M. J. Soileau. Energy band-gap dependence of two-photon absorption. *Optics Letters*, 10(10):490–492, 1985.

[64] M. J. Lederer, V. Kolev, B. Luther-Davies, H. H. Tan, and C. Jagadish. Ion-implanted InGaAs single quantum well semiconductor saturable absorber mirrors for passive mode-locking. *J. Phys. D: Appl. Phys*, 34:2455–2464, 2001.

[65] T. Hakkarainen, E.-M. Pavelescu, K. Arstila, V. D. S. Dhaka, T. Hakulinen, R. Herda, J. Konttinen, N. Tkachenko, H. Lemmetyinen, J. Keionen, and M. Pessa. Optical properties of ion arradiated and annealed InGaAs/GaAs quantum wells and semiconductor saturable absorber mirrors. *J. Phys. D: Appl. Phys.*, 38:985–989, 2005.

[66] J. T. Gopinath, E. R. Thoen, E. M. Koontz, M. E. Grein, L. A. Kolodziejski, and E. P. Ippen. Recovery dynamics in proton-bombarded semiconductor saturable absorber mirrors. *Appl. Phys. Lett.*, 78(22):3409–3411, 2001.

[67] S. Schön, M. Haiml, L. Gallmann, and U. Keller. GaAs absorber layer growth for broadband AlGaAs/flouride SESAMs. *Journ. Crystal Growth*, 227-228:172–176, 2001.

[68] A. Garnache, B. Sermage, R. Teissier, G. Saint-Girons, and I. Sagnes. A new kind of fast quantum-well Semiconductor Saturable-Absorber Mirror with low losses for ps pulse generation. *International Conference on Indium Phosphide and Related Materials*, pages 247–250, 2003.

[69] G. J. Spühler, K. J. Weingarten, R. Grange, L. Krainer, M. Haiml, V. Liverini, M. Golling, S. Schön, and U. Keller. Semiconductor saturable absorber mirror structures with low satuartion fluence. *Appl. Phys. B*, 81:27–32, 2005.

[70] D. Lorenser, H. J. Unold, D. J. H. C. Maas, A. Aschwanden, R. Grange, R. Paschotta, D. Ebeling, E. Gini, and U. Keller. Towards wafer-scale integration of high repetition rate passively mode-locked surface-emitting semiconductor lasers. *Appl. Phys. B*, 79:927–932, 2004.

[71] S. Gupta, J. F. Whitaker, and G. A. Mourou. Ultrafast Carrier Dynamics in III-V Semiconductors Grown by Molecular-Beam Epitaxy at Very Low Substrate Temperatures. *IEEE Journ. Quant. Electr*, 28(10), 1992.

[72] L. R. Brovelli, U. Keller, and T. H. Chiu. Design and operation of antiresonant FabryPerot saturable semiconductor absorbers for mode-locked solid-state lasers. *J. Opt. Soc. Am. B*, 12(2):311–322, 1995.

[73] M. Kuznetsov, M. Stern, and J. Coppeta. Single transverse mode optical resonators. *OPTICS EXPRESS*, 13(1):171–181, 2005.

[74] M. Grabherr, R. Jager, M. Miller, C. Thalmaier, J. Heerlein, R. Michalzik, and K. J. Ebeling. Bottom-Emitting VCSEL's for High-CW Optical Output Power. *IEEE Photon. Techn. Lett.*, 10(8):1061–1063, 1998.

[75] M. Grabherr, M. Miller, R. Jäger, R. Michalzik, U. Martin, H. J. Unold, and K. J. Ebeling. High-Power VCSEL's: Single Devices and Densely Packed 2-D-Arrays. *IEEE Journ. Select. Top. Quant. Electr.*, 5(3):495–502, 1999.

[76] M. Miller, M. Grabherr, R. King, R. Jäger, R. Michalzik, and K. J. Ebeling. Improved Output Performance of High-Power VCSELs. *IEEE Journ. Select. Top. Quant. Electr.*, 7(2):210–216, 2001.

[77] C. Yan, Y. Ning, L. Qin, D. Cui, Y. Liu, Y. Sun, Z. Jin, H. Li, G. Tao, C. Wang, L. Wang, and H. Jiang. High-Power Vertical-Cavity Surface-Emitting Laser With an Extra Au Layer. *IEEE Photon. Techn. Lett.*, 17(8):1599–1601, 2005.

[78] S. L. Chuang. *Physics of Optoelectronic Devices*. John Wiley & Sons, Wiley Series in Pure and Applied Optics, 1995.

[79] S. H. Park, J. I. Shim, K. Kudo, M. Asada, and S. Arai. Band gap shrinkage in GaInAs/GaInAsP/InP multi-quantum well lasers. *J. Appl. Phys.*, 72(1):279–281, 1992.

[80] D. Ahn and S. C. Choi. Band-gap renormalization effects on 980 nm strained-layer InGaAs/AlGaAs quantum-well lasers. *J. Appl. Phys.*, 76:7648–7650, 1994.

[81] Y. P. Vaarshni. Temperature dependence of the energy gap in semiconductors. *Physica*, 34(1):149–154, 1967.

[82] I. Vurgaftman, J. R. Meyer, and L. R. Ram-Mohan. Band parameters for IIIV compound semiconductors and their alloys. *Journ. Appl. Phys.)*, 89(11):5815–5875, 2001.

[83] E. P. O'Reilly and A. R. Adams. Band-structure Engineering in Strained Semiconductor Lasers. *IEEE Journ. Quant. Electr.*, 30(2):366–379, 1994.

[84] J. Katcki, J. Ratajczak, J. Adamczewska, F. Phillipp, N. Y. Jin-Phillipp, K. Regiński, and M. Bugajski. Formation of Dislocations in InGaAs/GaAs Heterostructures. *Phys. Stat. Sol (a)*, 171:275–282, 1999.

[85] J. R. Jensen. *MBE-grown semiconductor nanostructures with electronic and photonic confinement*. Ph. D. thesis, Research Center COM, Technical University of Denmark, 2000.

[86] A. Rosenauer, M. Melzer, M. Schowalter, D. Gerthsen, E. Piscopiello, A. Passaseo, R. Cingolani, J. P. Reithmaier, R. Krebs, A. Forchel, and G. Van Tendeloo. Segregation in InGaAs/GaAs Quantum Wells: MOCVD versus MBE. *Microscopy and Microanalysis*, 9(Suppl. 3):230–231, 2003.

[87] H. C. Casey and M. B. Panish. *Heterostructure Lasers, Part A: Fundamental Principles*. Academic Press Inc., 1978.

[88] D. L. Huffaker and D. G. Deppe. Intracavity Contacts for Low-Threshold Oxide-Confined Vertical-Cavity Surface-Emitting Lasers. *IEEE Photon. Techn. Lett.*, 11(8):934–936, 1999.

[89] M. H. MacDougal, J. Geske, C. Lin, A. E. Bond, and P. D. Dapkus. Low Resistance Intracavity-Contacted Oxide-Aperture VCSEL's. *IEEE Photon. Techn. Lett.*, 10(1):9–11, 1998.

[90] R. F. Kopf, E. F. Schubert, S. W. Downey, and A. B. Emerson. N- and P-type dopant profiles in distributed Bragg reflector structures and their effect on resistance. *Appl. Phys. Lett.*, 61(15):1020–1022, 1992.

[91] R. Baets, P. Demeester, and P. E. Lagasse. High-reflectivity $GaAs - AlGaAs$ mirrors: Sensitivity analysis with respect to epitaxial growth parameters. *J. Appl. Phys.*, 62(2):723–726, 1987.

[92] M. G. Peters, B. J. Thibeault, D. B. Young, J. W. Scott, F. H. Peters, A. C. Gossard, and L. A. Coldren. Band-gap engineered digital alloy interfaces for lower resistance vertical-cavity surface-emitting lasers. *Appl. Phys. Lett.*, 63(26):3411–3413, 1993.

[93] K. Tai, L. Yang, Y. H. Wang, J. D. Wynn, and A. Y. Cho. Drastic reduction of series resistance in doped semiconductor distributed Bragg reflectors for surface-emitting lasers. *Appl. Phys. Lett.*, 56(25):2496–2498, 1990.

[94] K. Kurihara, T. Numai, I. Ogura, A. Yasuda, M. Sugimoto, and K. Kasahara. Reduction in the series resistance of the distributed Bragg reflector in vertical cavities by using quasi-graded superlattices at the heterointerfaces. *J. Appl. Phys.*, 73(1):21–27, 1993.

[95] E. F. Schubert, L. W. Tu, G. J. Zydzik, R. F. Kopf, A. Benvenuti, and M. R. Pinto. Elimination of heterojunction band discontinuities by modulation doping. *Appl. Phys. Lett.*, 60(4):466–468, 1992.

[96] D. I. Babic, J. Piprek, K. Streubel, R. P. Mirin, N. M. Margalit, D. E. Mars, J. E. Bowers, and E. L. Hu. Design and Analysis of Double-Fused 1.55- m Vertical-Cavity Lasers. *IEEE Journ. Quant. Electr.*, 33(8):1369–1383, 1997.

[97] C. Asplund, S. Mogg, G. Plaine, F. Salomonsson, N. Chitica, and M. Hammar. Doping-induced losses in AlAs/GaAs distributed Bragg reflectors. *Journ. Appl. Phys.*, 90(2):794–800, July 2001.

[98] W. Nakwaski, M. Wasiak, P. Maćkowiak, W. Bedyk, M. Osiński, A. Passaseo, V. Tasco, M. T. Todaro, M. De Vittorio, R. Joray, J. X. Chen, R. P. Stanley, and A. Fiore. Oxidation kinetics of AlAs and (AlGa)As layers in GaAs-based diode laser structures: comparative analysis of available experimental data. *Semicond. Sci. Technol.*, 19:333–341, 2004.

[99] K. D. Choquette, K. M. Geib, C. I. H. Ashby, R. D. Twesten, O. Blum, H. Q. Hou, D. M. Follstaedt, B. E. Hammons, D. Mathes, and R. Hull. Advances in Selective Wet Oxidation of AlGaAs Alloys. *IEEE Journ. Select. Top. Quant. Electr.*, 3(3):916–926, 1997.

[100] P. O. Vaccaro, K. Koizumi, K. Fujita, and T. Ohachi. AlAs oxidation process in GaAs/AlGaAs/AlAs heterostructures grown by molecular beam epitaxy on GaAs (n11)A substrates. *Microelectronics Journal*, 30:387–391, 1999.

[101] B. Koley, M. Dagenais, R. Jin, J. Pham, G. Simonis, G. McLane, and D. Stone. Kinetics of growth of AlAs oxide in selectively oxidized vertical cavity surface emitting lasers. *Journ. Appl. Phys.*, 82(9):4586–4589, 1997.

[102] S. A. Feld, J. P. Loehr, R. E. Sheriff, J. Wiemeri, and R. Kaspi. Kinetics of AlAs Steam Oxidation at Low Pressure and Low Temperature Measured In-Situ Using a Novel Furnace Design with an Integral Optic Port. *Proceedings of IEEE International Symposium on Compound Semiconductors*, pages 325 –328, 1997.

[103] J.-T. Chu, C.-C. Kao, H.-W Huang, W.-D. Liang, C.-F. Chu, T.-C. Lu, H.-C. Kuo, and S.-C. Wang. Effects of different n-electrode patterns on optical characteristics of large-area p-side-down InGaN light-emitting diodes fabricated by laser lift-off. *Jpn. Journ. Appl. Phys.*, 44(11):7910–7912, 2005.

[104] A. Porch, D. V. Morgan, R. M. Perks, M. O. Jones, and P. P. Edwards. Transparent current spreading layers for optoelectronic devices. *Journ. Appl. Phys.*, 96(8):4211–4218, 2004.

[105] H. X. Wang, N. Jiang, H. Hiraki, K. Nishimura, H. Sasaoka, A. Hiraki, and S. Sakai. Fabrication of high-performance 407 nm violet light-emitting diode. *Journ. Crystal Growth*, 270:57–61, 2004.

[106] J. K. Sheu, G. C. Chi, and M. J. Jou. Enhanced output power in an InGaNGaN multiquantum-well light-emitting diode with an InGaN current-spreading layer. *IEEE Photon. Tech. Lett.*, 13(11):1164–1166, 2001.

[107] B. G. Streetman. *Solid State Electrnoc Devices*. Prentice Hall Inc., 1995.

[108] J. Morais, T. A. Fazan, R. Landers, R. G. Pereira, E. A. S. Sato, and Jr. W. Carvalho. Effect of rapid thermal annealing on the microstructure and electrical characteristics of Au/Ni/Au/Ge/Ni multilayers deposited on n-type InGaAs. *J. Vac. Sci. Technol. B*, 15(6):1983–1986, 1997.

[109] P. K. Seigal, R. D. Brigss, D. J. Rieger, A. G. Baca, and A. J. Howard. Adhesion studies of GaAs-based ohmic contact and bond pad metallization. *Thin Solid Films*, 290-291:503–507, 1996.

[110] M. Kang, J. Kim, and H. Park. New passivation of GaAs Schottky contact using sulfidation and hydrogenation. *Microprocesses and Nanotechnology Conference*, pages 220–221, 2000.

[111] F. Ren, A. Y. Cho, D. L. Sivco, S. J. Pearton, and C. R. Abernathy. Use of Sn-doped GaAs for non-alloyed ohmic contcas to HEMTs. *Electr. Lett.*, 30(11):912–914, 1994.

[112] W. O. Barnard, G. Myburg, F. D. Auret, S. A. Goodman, and W. E. Meyer. Metal contacts to Gallium Arsenide. *Journ. Electr. Materials*, 25(11):1695–1702, 1996.

[113] P. Royo, R. Koda, and L. A. Coldren. Vertical Cavity Semiconductor Optical Amplifiers: Comparison of Fabry-Perot and Rate Equation Approaches. *IEEE Journ. Quant. Electr.*, 38(3):279–284, 2002.

[114] P. Royo, R. Koda, and L. A. Coldren. Rate equations of vertical-cavity semiconductor optical amplifiers. *Appl. Phys. Lett.*, 80(317):3057–3059, 2002.

[115] E. S. Björlin. *Long-Wavelength Vertical-Cavity Semiconductor Optical Amplifiers*. Doctoral Thesis, University of California, Santa Barbara, 2002.

[116] G. P. Agrawal and N. A. Olsson. Self-phase Modulation and Spectral Broadening of Optical Pulses in Semiconductor Laser Amplifiers. *IEEE Journ. Quant. Electr.*, 25(11):2297–2306, 1989.

[117] M. Hatzakis, B. J. Canavello, and J. M. Shaw. Single-Step Optical Lift-Off Process. *IBM Journal of Research and Development*, 24(4):452–460, 1980.

[118] N. Gregersen. *Oxide Confined Vertical Cavity Surface Emitting Lasers*. Master Thesis Project, rsted Laboratory, Niels Bohr Institute, Copenhagen University, 2002.

[119] J. J. LePore. An improved technique for selective etching of GaAs and $Ga_{1-x}Al_xAs$. *Journ. Appl. Phys.*, 51(12):6441–6442, 1980.

[120] E. Yablonovitch, T. Gmitter, J. P. Harbinson, and R. Bhat. Extreme selectivity in the lift-off of epitaxial GaAs films. *Appl. Phys. Lett.*, 51(26):2222–2224, 1987.

[121] M. Tong, D. G. Ballegeer, A. Ketterson, E. J. Roan, K. Y. Cheng, and I. Adesida. A Comparative Study of Wet and Dry Selective Etching Processes for GaAs/AlGaAs/InGaAs Pseudomorphic MODFETs. *Journ. Electr. Mater.*, 21(1):9–15, 1992.

[122] K. Yvind. *Semiconductor mode-locked lasers for optical communications systems*. Ph.D. Thesis, $DTU \cdot COM$, Technical University of Denmark, Kgs. Lyngby, Denmark, 2003.

[123] Jasprit Singh. *Semiconductor Optoelectronics, Physics and Technology*. McGraw-Hill International Editions, 1995.

[124] K. E. Moselund. *Vertical-Cavity Surface-Emitting Lasers*. Master Thesis Project, COM, Technical University of Denmark, 2002.

[125] R. Paschotta and U. Keller. Passive mode locking with slow saturable absorbers. *Appl. Phys. B*, 73:653–662, 2001.

[126] C. Y.-P. Chao and S. L. Chuang. Spin-orbit-coupling effects on the valence-band structure of strained semiconductor quantum wells. *Phys. Rev. B*, 46(7):4110–4122, 1992.

[127] B. H. Brandsen and C. J. Joachain. *Introduction to Quantum Mechanics*. Longman Scientific Technical, 1989.

[128] M. Yamanishi and I. Suemune. Comment on Polarization Dependent Momentum Matrix Elements in Quantum Well Lasers. *Japanese Journ. Apll. Phys.*, 23(1):L35–L36, 1984.

[129] S. Hausser, G. Fuchs, A. Hangleiter, and K. Streubel. Auger recombination in bulk and quantum well InGaAs. *Appl. Phys. Lett.*, 56:913–915, 1990.

[130] U. Strauss and W. W. Rühle. Auger recombination in intrinsic GaAs. *Appl. Phys. Lett.*, 62(1):55–57, 1993.

[131] M. A. Afromowitz. Refractive Index of $Ga_{1-x}Al_xAs$. *Solid State Comm.*, 15:59–63, 1974.

Appendix A

Strain and gain in QWs

A.1 Strain of the quantum wells

The in-plane lattice constant of the $In_{1-x}Ga_xAs$-quantum wells of eVCAs in this project varies from around $5.77 - 5.80$ ($0.80 \leq x \leq 0.85$), i.e. a percentage strain of around $2 - 2.6$ when grown on $AlGaAs$. The quantum wells are compressively strained as the native in-plane lattice-constant of the wells is *larger* than that of $AlGaAs$.

The corrections of the conduction band and valence band calculated here are based on the model-solid theory presented in *Physics of Optoelectronic Devices, John Wiley & Sons* [78] and Chao *et al.* [126], and using band-, and material-parameters from Vurgaftman *et al.* [82].

The hydrostatic component of the strain arises as the volume of the unit cell of the quantum well material is changed. The hydrostatic strain shifts the band gap of the material. The shear strain introduces a separation of the heavy hole and light hole bands at $\mathbf{k} = 0$. This separation leads to a smaller interaction between the heavy hole and light hole bands, which favours the conduction band to heavy hole band transition.

The strain reduces the in-plane effective mass of the heavy hole band, i.e. increases the heavy hole band curvature to be closer to the curvature of the conduction band [78]. This leads to a more symmetrical separation of the quasi-Fermi levels and, as a result, the strained material has a lower transparency carrier density, which leads to a reduced carrier injection level. In turn, the Auger recombination rate is reduced and this enhances the differential quantum efficiency and thus leads to an increased differential gain.

The calculation of the strain effect on the band energies is based on the 6×6 Luttinger-Kohn Hamiltonian matrix (for $\mathbf{k} = 0$) which includes the

coupling between the heavy-hole (HH), light-hole (LH) and spin-orbit split-off (SO) bands [78]. Biaxial strain is assumed, i.e. $\epsilon_{xy} = \epsilon_{yz} = \epsilon_{zx} = 0$ and $\epsilon_{xx} = \epsilon_{yy} \neq \epsilon_{zz}$, where x and y are the in-plane (or transversal) directions whereas z is the out-of plane direction.

The strain is expressed in terms of the deformation of the valence-band, $P_e = -a_v(\epsilon_{xx} + \epsilon_{yy} + \epsilon_{zz})$, and conduction-band, $Q_e = -\frac{b}{2}(\epsilon_{xx} + \epsilon_{yy} - 2\epsilon_{zz})$, where a_v and b are the hydrostatic deformation potentials. In case of biaxial strained material $\epsilon_{xx} = \epsilon_{yy} = \frac{a_{sub}-a}{a}$, where a_{sub} and a are the in-plane lattice constant of the substrate and strained material respectively. $\epsilon_{zz} = -\epsilon_{xx}\frac{2C_{12}}{C_{11}}$ expresses the out-of plane strain tensor which depends on the stiffness of the strained material given by C_{11} and C_{12}.

The stiffness-parameters, the in-plane lattice constants, the deformation potentials and the spin-orbit split-off energies, Δ, of the binary compounds $GaAs$, $InAs$ and $AlAs$ and the bowing parameter, C, for the ternary alloys $AlGaAs$ and $InGaAs$ are parameters taken from Vurgaftman *et al.* [82] and are presented in table A.2. The energy-gap of the ternary alloy $AlGaAs$ is equal to

$$E_g(Al_{1-x}Ga_xAs) = (1-x)E_g(AlAs) + xE_g(GaAs) - x(1-x)C. \quad \text{(A.1)}$$

where C is the bowing parameter.

The shifts of the heavy hole, light hole, and split-off bands respectively at $\mathbf{k} = 0$ calculated via the Hamiltonian Matrix are equal to

$$\Delta E_{HH}(0) = -P_e - Q_e \quad \text{(A.2)}$$

$$\Delta E_{LH}(0) = -P_e + \frac{1}{2}(Q_e - \Delta + \sqrt{\Delta^2 + 2\Delta Q_e + 9Q_e^2}) \quad \text{(A.3)}$$

$$\Delta E_{SO}(0) = -P_e + \frac{1}{2}(Q_e - \Delta - \sqrt{\Delta^2 + 2\Delta Q_e + 9Q_e^2}) \quad \text{(A.4)}$$

The mass in the z-direction and the transversal mass (in the xy-plane) masses are defined by the Luttinger-parameters [126]

$$\frac{m^*_{hhz}}{m_0} = \frac{1}{\gamma_1 - 2\gamma_2}, \frac{m^*_{hht}}{m_0} = \frac{1}{\gamma_1 + \gamma_2} \quad \text{(A.5)}$$

$$\frac{m^*_{lhz}}{m_0} = \frac{1}{\gamma_1 + 2\gamma_2}, \frac{m^*_{lht}}{m_0} = \frac{1}{\gamma_1 - \gamma_2} \quad \text{(A.6)}$$

	$GaAs$	$AlAs$	$InAs$	GaP
$a[\dot{A}]$	$5.65 + 3.88 \cdot 10^{-5}T$ ‡	$5.66 + 2.90 \cdot 10^{-5}T$ ‡	$6.06 + 2.74 \cdot 10^{-5}T$ ‡	$5.25 + 2.92 \cdot 10^{-5}T$ ‡
E_g	1.519	3.099	0.417	2.886
Δ	0.341	0.280	0.390	0.08
γ_1	6.98	3.76	20.0	4.05
γ_2	2.06	0.82	8.5	0.49
γ_3	2.93	1.42	9.2	2.93
E_p	28.8	21.1	21.5	31.4
F	−1.94	−0.48	−2.90	-2.04
VBO	−0.80	−1.33	−0.59	-1.27
a_c	−7.17	−5.64	−5.08	-8.2
a_v	−1.16	−2.47	−1.00	-1.7
b	−2.0	−2.3	−1.8	-1.6
C_{11}	1221	1250	832.9	1405
C_{12}	566	534	452.6	620.3

Table A.1: Parameters extracted from [82]. ‡: T in K

	$C(Al_{1-x}Ga_xAs)$	$C(In_{1-x}Ga_xAs)$	$C(GaAs_{1-x}P_x)$
E_g	$-0.127 + 1.310(1-x)$	0.477	0.8
Δ	-	0.15	0.15
γ_2	-	$0.481*$	-
γ_3	-	$0.481*$	-
E_p	-	-1.48	-
F	-	1.77	-
VBO	-	-0.38	1.71
a_c	-	2.61	-

Table A.2: Bowing parameters extracted from [82]. $*$: bowing parameter value valid for $\gamma_3 - \gamma_2$.

The Luttinger-parameters are extracted from Vurgaftman *et al.* [82] and are also presented in table A.2.

The strained material *relaxes* when its thickness reaches a critical thickness. When a strained material relaxes, misfit defects such as dislocations occur. These defects lead to deep-gap states in the materials which should be avoided if the material is to be used as the active materials in e.g. lasers or diodes. The strain can be equaled out by introducing strain of opposite sign, why some laser- or diode-designs have barriers of materials with a *smaller* in-plane lattice constant, e.g. $GaAsP$, around the active region.

All optical transitions of the strained quantum wells in designs presented in this thesis have been calculated using MATLAB using the above equations and parameters. The quantum levels of the strained quantum wells are calculated using simple quantum mechanics [127].

A.2 Gain in quantum wells

This section is dedicated to the calculations of the interband absorption and gain in a quantum well. All calculations are based on chapter 9 of *Physics of Optoelectronic Devices, John Wiley & Sons* [78] and uses a parabolic band model.

The gain coefficient of the transition from the n'th electron sub-band to the m'th valence sub-band is calculated for photons of energy $\hbar\omega$, see figure A.1, by the following equation

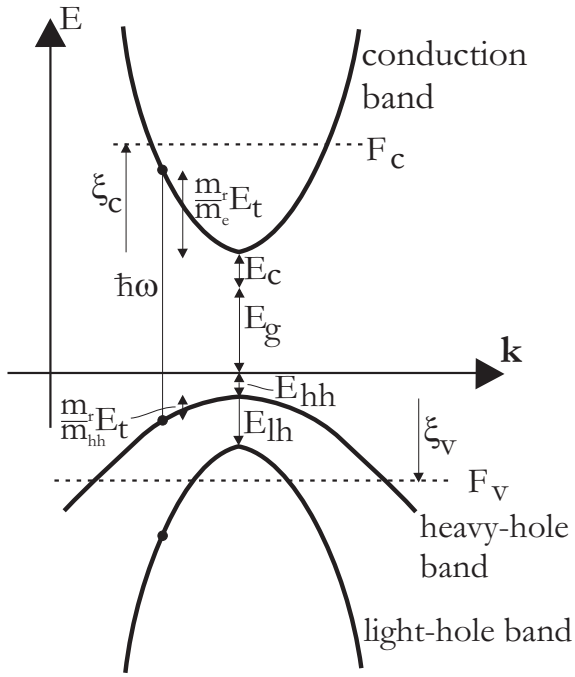

Figure A.1: A quantum well and its conduction band heavy-hole band and light-hole band. $\hbar\omega$ is the energy of the amplified photon, ξ_c is the quasi-Fermi level in the conduction band, calculated positive when positioned in the conduction band. The same applies for the the quasi-Fermi level in the valence band.

$$g(\hbar\omega) = \sum_{n,m} C_0 |I_{hm}^{en}|^2 \rho_r^{2D} |\widehat{e} \cdot \overline{p}_{cv}|^2 \cdot [f_c(E_t = \hbar\omega - E_{hm}^{en}) - f_v(E_t = \hbar\omega - E_{hm}^{en})] H(\hbar\omega - E_{hm}^{en}) \tag{A.7}$$

the sum runs over all electron and hole states, E_{en} and E_{hm}. The pre-factor is equal to

$$C_0 = \frac{1}{\hbar\omega} \frac{\hbar\pi e^2}{n_r c \varepsilon_0 m_0^2} \tag{A.8}$$

where e is the elementary electron charge, n_r is the refractive index of the gain-material which is set to 3.65, ε_0 is the permittivity of free space and m_0 is the electron mass. The overlap integral of the conduction band and valence band envelope functions is

$$I_{hm}^{en} = \int_{-\infty}^{\infty} \phi_n(z)\psi_m(z)dz \tag{A.9}$$

and $|I_{hm}^{en}|^2$ is here assumed to be equal to 1 for transitions where $m = n$ and otherwise 0.

The two-dimensional density of states is $\rho_r^{2D} = \frac{m_{hh}}{\pi\hbar L_z}$ for heavy holes and $\rho_r^{2D} = 2\frac{m_{lh}}{\pi\hbar L_z}$ for light holes, where m_{hh} and m_{lh} are the transversal masses of the heavy holes and light holes respectively. $H(\hbar\omega - E_{hm}^{en})$ is a step-function that is equal to one for $\hbar\omega > E_g + E_c + E_{hh}$ for the conduction band to heavy hole transition and otherwise zero. Likewise, $H(\hbar\omega - E_{hm}^{en})$ is equal to one for the conduction band to light hole transition when $\hbar\omega > E_g + E_c + E_{lh}$.

The optical matrix element in quantum well structures depends on the polarisation of the interacting electromagnetic field, $\hat{\mathbf{e}}$, and the momentum of the involved carriers, $\mathbf{p}$. The heavy hole and light hole contribution to the gain is thus polarisation dependent; the conduction band to heavy hole transition only interacts with light polarised in plane with the quantum well (TE mode). The conduction band to light hole transition interacts both with light polarised in plane and perpendicular to the quantum well (TM mode). The matrix elements are thus different from transverse electric (TE) and transverse magnetic (TM) field. The following expressions of the optical matrix elements of the conduction band to heavy hole (CHH) or light hole (CLH) transitions are used [78, 128]:

$$|\widehat{e}\cdot\overline{p}_{cv}|^2_{CHH,TE} = \frac{3}{4}(1 + cos^2\Theta)M_b^2 \tag{A.10}$$

$$|\widehat{e}\cdot\overline{p}_{cv}|^2_{CLH,TE} = (\frac{5}{4} - \frac{3}{4} - 3/4cos^2\Theta)M_b^2 \tag{A.11}$$

$$|\widehat{e}\cdot\overline{p}_{cv}|^2_{CHH,TM} = \frac{3}{2}sin^2\Theta M_b^2 \tag{A.12}$$

$$|\widehat{e}\cdot\overline{p}_{cv}|^2_{CLH,TM} = \frac{1}{2}(1 + 3cos^2\Theta)M_b^2 \tag{A.13}$$

where the angular factor $cos^2\Theta = \frac{E_c+E_{hh}}{E_c+E_v+\frac{\hbar^2k_t^2}{2m_r}}$ where e.g. $\frac{\hbar^2k_t^2}{2m_r} = \frac{m_r}{m_{hh}}E_t = \frac{m_r}{m_{hh}}(\hbar\omega - (E_g + E_c + E_{hh}))$ is the penetration of the incoming photon of energy $\hbar\omega$ into the heavy hole band, see figure A.1. The reduced mass, m_r is assumed equal to $(1/m_e + 1/m_v)^{-1}$ (where m_v is the effective mass of the valence band) and $M_b^2 = (m_0/6)E_p$ where E_p according to [78] is equal to $25eV$ for $GaAs$ (no value for $InGaAs$ is available).

The quasi-fermi levels for electrons and holes are denoted F_c and F_v respectively in figure A.1. The separation of the quasi-Fermi levels to the energy bands are in he following calculations expressed by ξ_c and ξ_v in units of eV and are positive values when the quasi-Fermi levels are located in the conduction band and valence band respectively. The quasi-Fermi levels determine the number of carriers, and are thus connected to the applied current of the structure.

The Fermi-Dirac distribution for the electrons in the conduction band in terms of the quasi-Fermi level in the conduction band, ξ_c, is

$$\begin{aligned} f_c(E(t)) &= (1 + exp[(\frac{E_g + E_c + \frac{m_r}{m_e}E_t - F_c)}{kT}])^{-1} \\ &= (1 + exp[\frac{(-\xi_c + \frac{m_r}{m_e}E_t)}{kT}])^{-1} \end{aligned} \tag{A.14}$$

A similar expression of the distribution of the heavy-holes in the valence band equals

$$\begin{aligned} f_v(E(t)) &= (1 + exp[\frac{(E_{hh} + \frac{m_r}{m_{hh}}E_t - F_v)}{kT}])^{-1} \\ &= (1 + exp[\frac{(\xi_v - \frac{m_r}{m_{hh}}E_t)}{kT}])^{-1} \end{aligned} \tag{A.15}$$

The gain coefficient in units of cm^{-1} of the TE-polarised field in the conduction band to heavy hole *and* light hole transitions in a $8 - nm$ $In_{0.175}Ga_{0.825}As$ quantum well with $Al_{0.15}Ga_{0.85}As$ barriers (equal to the TAIWAN and NBI structure) at different quasi-Fermi separations denoted by ξ_c and ξ_v is calculated and illustrated in figure A.2. The gain coefficient at 960 nm of the conduction band to heavy hole transition versus the quasi-Fermi separation is also illustrated in figure A.3. This figure shows the importance of increasing *both* ξ_c and ξ_v to obtain a high gain coefficient.

The optical transition is broadened due to a finite state lifetime. The gain in figure 3.5 is thus convoluted with a Gaussian linewidth with a full width half maximum of 100 fs [60]. Additional broadening of the optical transitions of the quantum wells is not considered here.

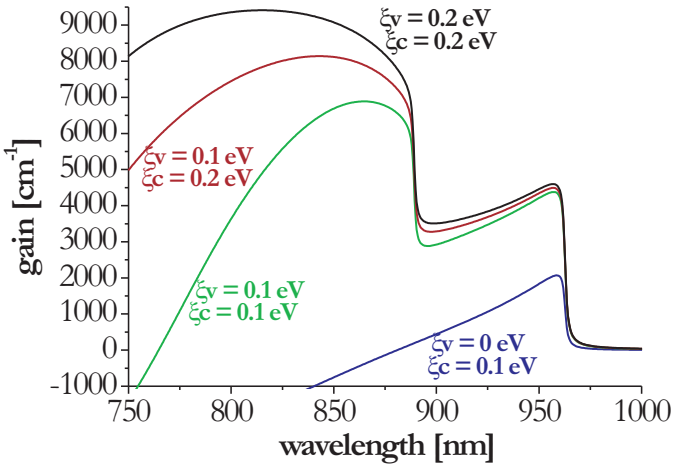

Figure A.2: TE-gain coefficient of the conduction band to heavy hole *and* light hole transition in a $8 - nm$ $In_{0.175}Ga_{0.825}As$ quantum well with $Al_{0.15}Ga_{0.85}As$ barriers (equal to the TAIWAN and NBI structure) at different separations of the quasi-Fermi levels to the energy bands denoted by ξ_c and ξ_v. The conduction band to heavy hole transition is located at 955 nm, and the conduction band to light hole transition is located at 870 nm. The gain in the conduction band to heavy hole transition is illustrated in figure A.3 as well.

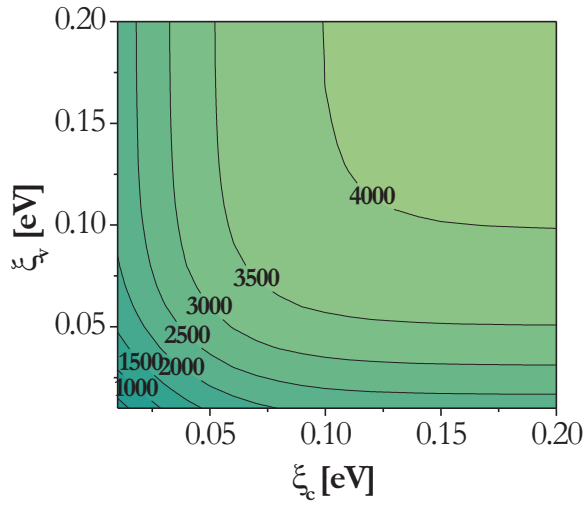

Figure A.3: TE-gain coefficients of the conduction band to heavy hole transition in a $8-nm$ $In_{0.175}Ga_{0.825}As$ quantum well with $Al_{0.15}Ga_{0.85}As$ barriers (similar to figure A.2) versus the separations, ξ_c and ξ_v. The gain coefficients are in units of cm^{-1}.

Appendix B

Gain saturation

The gain saturation power of the devices is calculated by a model based on a set of modified rate equations presented in Royo *et al.* [113, 114] and the Ph.D. thesis of Björlin [115]. The rate equations include a mirror loss, α_m, which makes the model valid for devices with highly reflective mirrors such as vertical-cavity semiconductor optical amplifiers (VCSOAs); in these devices, the carrier density is reduced due to an enhancement of stimulated emission close to threshold or at high external input powers.

The rate equations express the decay or increase of the carrier density, dN/dt, in the active region and the photon density, dS/dt, in the structure, both in units of $s^{-1}cm^{-3}$:

$$\begin{aligned} \frac{dN}{dt} &= G_{gen} - R_{st} - R_{nr} \\ &= \frac{\eta_i I}{qV_a} - \Gamma v_g g S - (AN + BN^2 + CN^3) \end{aligned} \tag{B.1}$$

$$\begin{aligned} \frac{dS}{dt} &= \frac{\delta S_{ext}}{\delta t} + R_{sp} + R_{st} - R_{loss} \\ &= \frac{P_{ext}}{h\nu_{ext}V_{eff}} + \beta\Gamma_{QW}BN^2 + \Gamma\Gamma_{QW}gv_gS - (\alpha_i + \alpha_m)v_gS \end{aligned} \tag{B.2}$$

where G_{gen} equals the generated carriers per second per volume via the current-injection of I and injection efficiency, η_i, in the active volume V_a. The second term in equation B.1 expresses the stimulated recombination and is proportional to the product of the photon density, S, the gain coefficient per unit length, g, the group velocity, v_g, and the confinement factor, Γ. The third term is a sum of recombinations that do not contribute to

the gain in the device expressed by the A, B and C coefficients (defect recombination coefficient, bimolecular recombination coefficient and Auger recombination coefficient).

$\delta S_{ext}/\delta t$ is the density of photons with energy $h\nu_{ext}$ added per second to the effective volume of the structure, V_{eff}, by the external input signal with a power of P_{ext}. The second and third terms in equation B.2 express the spontaneous and stimulated recombinations where the confinement factor Γ_{QW} has been added which is equal to the length of the active material divided by the total effective length of the structure, L_a/L_{eff}. The effective length of the structure, L_{eff}, is the length of the cavity *plus* the penetration depth into the BDRs, which for a DBR with reflectivity R at the design wavelength λ_B and refractive index difference of Δn is equal to $\sqrt{R}\lambda_B/4\Delta n$ [5]. Furthermore, the spontaneous recombination is proportional to the spontaneous emission factor, β.

The fourth term in equation B.2 is the sum of mirror loss and internal loss, denoted by the absorption coefficients α_m and α_i respectively. The internal loss is the average free carrier loss in the effective structure length and can be estimated on the basis of equation 3.5 on page 46. The mirror loss is a cavity-related loss equal to [113]

$$\alpha_m = \frac{1}{L_{eff}} \frac{G}{G-1} ln[G_s] \tag{B.3}$$

where G is the total gain of the structure and equal to

$$G = 1 + \frac{(1-R_t)(1+R_bG_s)(G_s-1)}{(1-\sqrt{R_tR_b}G_s)^2 + 4\sqrt{R_tR_b}G_s sin^2(\varphi)} \tag{B.4}$$

where R_b and R_t are the bottom and top DBR reflectivities. φ is the detuning of the wavelength and equal to 0 at the design wavelength. The gain saturation of the structure has only been calculated at the design wavelength of the structure why this term is neglected. The single-pass gain, G_s is equal to

$$G_s = e^{(\Gamma g L_a - \alpha_i L_{eff})} \tag{B.5}$$

And the gain coefficient as a function of the carrier-density, N is expressed by a first-order approximation [60]

$$g = g_0 ln(\frac{N}{N_{tr}}) \tag{B.6}$$

where N_{tr} is the carrier density at transparency and g_0 is a fitting parameter.

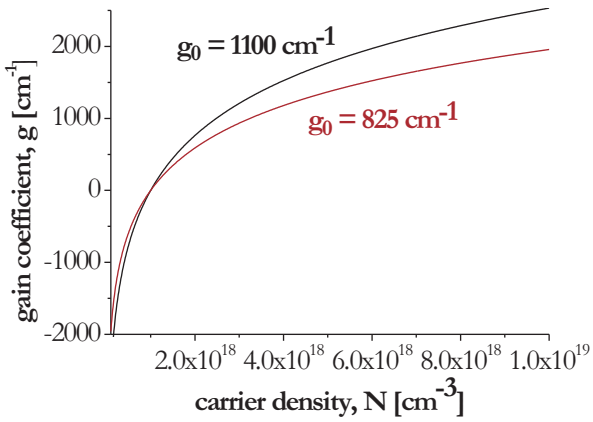

Figure B.1: Gain coefficient in units of cm^{-1} as a function of carrier density accordingly to equation B.6. g_0 is set to $1100cm^{-1}$ for the IQE structure and 825 cm^{-1} in the TAIWAN structure.

A steady-state gain saturation is calculated by letting $\frac{dS}{dt} = \frac{dN}{dt} = 0$ and inserting an expression for S from equation B.2 into equation B.1. The expression of the gain, equation B.6, is also inserted, thus ending up with an equation which only depends on the carrier density, N. This equation is solved for N for different external signal powers P_{ext}, and this N is again inserted in the gain equations B.6 and B.5 to calculate the single pass gain, G_s. The total reflection of the structure with a single-pass gain of G_s is expressed by [113]

$$R_G = \frac{(\sqrt{R_t} - \sqrt{R_b}G_s)^2 + 4\sqrt{R_t R_b}G_s sin^2(\varphi)}{(1 - \sqrt{R_t R_b}G_s)^2 + 4\sqrt{R_t R_b}G_s sin^2(\varphi)} \tag{B.7}$$

The gain saturation power is defined as the external signal power where the gain of the structure, i.e. $R_G - 1$, is decreased to half its value at infinitely small external signal power.

The gain saturation power has been calculated for two of the four types of eVCAs presented in chapter 4 and 5 of this thesis, namely the IQE and TAIWAN eVCAs. The parameters used to calculate the gain saturation of these two eVCAs are presented in table B.1. The confinement factor Γ is calculated using the equation presented at page 160. The injection efficiency is estimated to be 0.5.

The carrier density at transparency is estimated from the $SILVACO$

parameter	IQE	TAIWAN	description
R_b	0.999	0.999	bottom mirror reflectivity
R_t	0.03	0.700	top mirror reflectivity
Γ ♮	1.718	1.785	confinement factor
N_{tr}	$1 \cdot 10^{18}$	$1 \cdot 10^{18}$	carrier density at transparency (cm^{-3})
g_0	1100	825	fitting parameter to gain (cm^{-1})
v_g *	$9 \cdot 10^{-9}$	$9 \cdot 10^{-9}$	group velocity (cm/s)
A *	$3 \cdot 10^{8}$	$3 \cdot 10^{8}$	defect recombination coefficient ($1/s$)
B *	$1 \cdot 10^{-10}$	$1 \cdot 10^{-10}$	bimolecular recombination coefficient (cm^3/s)
C *	$4 \cdot 10^{-30}$	$4 \cdot 10^{-30}$	Auger recombination coefficient (cm^6/s)
β *	0.02	0.02	spontaneous emission factor
α_i	15	15	internal loss (cm^{-1})
η_i *	0.3	0.3	injection efficiency
$h\nu_{ext}(= hc/\lambda_B)$	$2.03 \cdot 10^{-19}$	$2.07 \cdot 10^{-19}$	photon energy of external input (J)
d_a	$30 \cdot 10^{-4}$	$150 \cdot 10^{-4}$	aperture diameter (μm)
A_a	$0.7069 \cdot 10^{-5}$	$17.67 \cdot 10^{-5}$	aperture area (cm^2)
L_{eff}	$1 \cdot 10^{-5}$	$1 \cdot 10^{-5}$	effective cavity-length (cm)
$V_{eff}(= L_{eff} \cdot A_a)$	$706.9 \cdot 10^{-12}$	$17.67 \cdot 10^{-9}$	volume of effective cavity (cm^3)
L_a	$81 \cdot 10^{-7}$	$24 \cdot 10^{-7}$	vertical length of active region (cm)
$V_a(= L_a \cdot A_a)$	$57.26 \cdot 10^{-12}$	$424.1 \cdot 10^{-12}$	volume of active region (cm^3)
$\Gamma_{QW}(= L_a/L_{eff})$	0.081	0.024	volume of active region (cm^3)

Table B.1: Parameters for gain saturation model. Values marked with * are extracted from [115]. Value marked with ♮ is calculated from equation B.8.

simulations from section 3.4 to be around $1 \cdot 10^{18}$ cm^{-3} for both structures. The gain-fitting parameter, g_0 (equation B.6) is fitted to the measured gain coefficients of the IQE and TAIWAN quantum wells presented in table 5.2, which is 2650 cm^{-1} in the IQE quantum wells and 1900 cm^{-1} in the TAIWAN quantum wells.

In the bottom-emitting TAIWAN eVCA, the gain saturation power is calculated for a device without substrate. The reflectivity of the TAIWAN structure without substrate and with a gain coefficient of 1900 cm^{-1} is calculated to 1.02.

The gain saturation power depends on the current injected to the eVCAs, I. The injected current, I, is set so that the reflectivities of the structures at small external signal powers are equal to the measured reflectivity (IQE) and calculated reflectivity (TAIWAN). The injection efficiency, η_i, is set to 0.3.

Even though there is no top mirror on the IQE structure, it has an oxidation layer of 30 nm $AlAs$. This means that the structure effectively has a single $GaAs/AlAs$ DBR pair corresponding to a R_t of 3 %.

The resulting gain saturation powers of the two structures are presented in table B.2.

name	reflectivity	aperture diameter $[\mu m]$	P_{sat} $[W]$	F_{sat} $[kW/cm^2]$
IQE	1.087	43	3.77	260
TAIWAN	1.02	150	0.391	2.21

Table B.2: Measured (IQE) and calculated (TAIWAN) small-signal reflectivities and gain saturation powers of the IQE and TAIWAN structures. The aperture diameter of the IQE and TAIWAN eVCAs are 43 μm^2 and 150 μm^2, which gives the gain saturation fluences (in units of W/cm^2) as listed to the right.

As the loss in the substrate is not included in these calculations, the listed gain saturation power of the TAIWAN eVCA in table B.2 should be multiplied with a factor of e^{at}, where a is the absorption coefficient of the substrate (-6 cm^{-1} in a substrate n-doped with $2 \cdot 10^{18}$ cm^{-3}) and t the thickness of the substrate.

The gain saturation power has been calculated for the TAIWAN structure (without substrate) with a gain coefficient of 2500 cm^{-1} in the quantum wells and a varying top mirror reflectivity, R_t, from 0 to 1. The result is shown in figure B.2; as the top mirror reflectivity is increased from 0 to 1, the gain saturation decreases from ~ 2.5 W to ~ 0.01 W. The maximum reflectivity increases from ~ 1 to ~ 1.8.

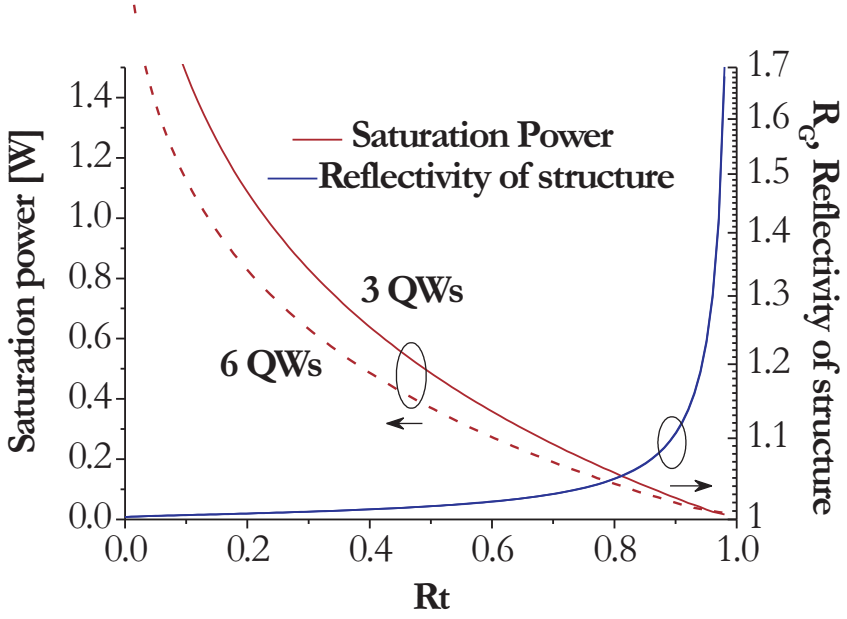

Figure B.2: The reflectivity and saturation power of the TAIWAN structure with a gain coefficient of 2500 cm^{-1} in the quantum wells versus the top mirror reflection, R_t, varied from 0 to 1.

The NBI structure is very close to the TAIWAN structure except that the NBI structure only has 0.5 pair of top $GaAs/AlAs$ DBR, R_t is thus close to 38 % if the structure is left un-coated. Assuming the quantum wells in the NBI structure have same gain coefficient in as the wells in the TAIWAN structure, the gain saturation power of the NBI structure with a top DBR reflectivity of 38 % is 0.87 W according to the graph of figure B.2. If the NBI structure is AR-coated, the top DBR will have a reflectivity close to 0.79 % and a gain saturation power of around 3.9 W.

Confinement factor, Γ

The confinement factor in a vertical-cavity structure is proportional to the overlap between the standing longitudinal optical field and the active region. In case of M active sections located at $z_{il} \leq z \leq z_{ih}$ where $i = 1..M$, Γ is given by [5]

$$\Gamma = 1 + \frac{\lambda}{4\pi\bar{n}}(1 + \frac{\sum_{i=1}^{M}(sin(\frac{4\pi\bar{n}z_{ih}}{\lambda}) - sin(\frac{4\pi\bar{n}z_{il}}{\lambda}))}{\sum_{i=1}^{M}(z_{ih} - z_{il})}) \tag{B.8}$$

where $\bar{n}$ is the average index of refraction in the cavity.

According to [5], a structure with three $8nm$-thick quantum wells separated by 10 nm thick barriers located in an antinode has a confinement-factor of $\Gamma \simeq 1.785$.

Appendix C

Simulations in *SILVACO*

C.1 Modelling of eVCA using *SILVACO*

In order to improve the design of the quantum well region and current spreading layers in the eVCAs, these regions have been simulated using *ATLAS*, which is a part of the *SILVACO*-package (*www.silvaco.com*). This appendix elaborates the programming in *SILVACO* and *ATLAS*.

ATLAS can simulate the electrical and thermal behavior of 2 or 3 dimensional semiconductor devices. It includes a variety of physical models such as drift-diffusion, lattice-heating, Fermi-Dirac and Boltzmann statistics and Shockley-Read-Hall and Auger recombination. It uses the numerical techniques of Gummel and Newton to solve the models, and it interfaces the output to a *SILVACO*-package called *TONYPLOT* which displays the structure layer for layer and allows you to make cut-lines through the device in order to investigate e.g. the band line up or the lateral current profile in any layer.

The structure is defined in the growth-direction (y-direction) layer by layer by the MATERIAL-statement, e.g. ;

```
x.mesh location=0 spacing=0.5
x.mesh location=5 spacing=0.5

region number=1 material=AlGaAs x.composition=0.7
                thick=0.1 ny=5 donor=1e17

region number=2 material=oxide x.min=2 x.max=5 thick=0.1 ny=5


region number=3 material=AlAs x.min=0 x.max=2  thick=0.1 ny=5
                donor=1e17
```

```
region number=4 material=AlGaAs x.composition=0.7
                thick=0.1 ny=5 donor=1e17

region number=5 material=GaAs thick=0.1 ny=5 donor=1e17

region=1 affinity=3.8790 eg300=1.7159
```

The above statements define the structure shown in figure C.1. The mesh in the x-direction is specified at the beginning of the program by the `x.mesh` statement; here a structure of 5 μm in width with a mesh of 0.5 μm is used. The last statement (`region=1 affinity..`) adds information on the affinity and band-gap of region 1. This is necessary for all layers other than $GaAs$, as the affinity and band-gap of $AlGaAs$ and $GaAsP$ by default are set equal to those of $GaAs$.

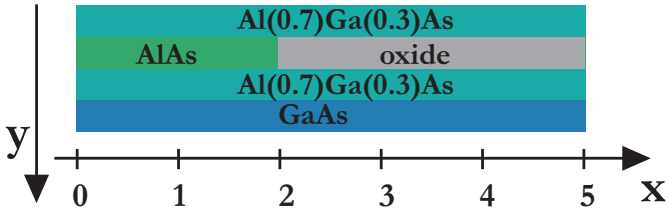

Figure C.1: A structure in *SILVACO*

The doping of each layer is stated by either `accept` or `donor` and is in units of cm^{-3}. In *SILVACO* it was necessary to simulate the un-doped layers of the structure with slightly doped layers with a donor concentration of 10^{16} cm^{-3}, otherwise the resistivity of the layers would be too high.

The mesh in the y-direction is specified for each layer with the statement `sy` which defines the distance between the mesh-points in the y-direction, or by `ny` that defines the number of mesh-points in the y-region in that specific layer.

The contacts (*electrodes*) are defined by the `electrode`-statement which also allows to confine the contacts to certain regions, in this case a cathode from $x = 3$ to $x = 5$ μm and an anode that covers the entire bottom surface of the device:

```
electrode name=cathode x.min=3 x.max=5 top

electrode name=anode bottom
```

All simulations are performed in cylindrical coordinates which is stated at the beginning of the program with

```
mesh cylindrical
```

In cylindrical coordinates, the program operates with $x = 0$ as the axis of symmetry.

Before the program applies a voltage across the structure, preferred models are turned on, e.g. by the statement

```
models srh auger optr fermidirac print
```

which turns on the Shockley-Read-Hall, Auger and optical recombination processes in the device. With the above statement the carrier distributions is calculated with a Fermi-Dirac distribution and the program prints the status of the models and the constants used in the simulations on the screen while calculating.

The output of the calculations can be defined by using `output`, e.g.

```
output band.param con.band val.band u.auger u.radiative u.srh
```

which enables the plotting of the energy band parameters, Auger and Shockley-Read-Hall recombinations and radiative recombinations.

Finally, the statements

```
solve init

save outf=design1init.str

solve prev

solve vstep=0.01 name=anodevfinal=0.1
save outf=design1.str
```

let *ATLAS* solve the initial structure without any applied voltage, and save the calculations in a file of str-format. The voltage across the structure is ramped up to 0.1 V in steps of 0.01 V, and the output is saved. The str-files and thus the output of the simulations are interfaced to *TONYPLOT* which displays the structure seen perpendicularly to the "growth"-direction, as in figure C.1. In *TONYPLOT*, the carrier concentrations, conduction and valence bands, electrical field can be plotted in user-defined cut-lines in the x or y directions of the structure. In this way, e.g. the carrier concentration in the $Al_{0.70}Ga_{0.30}As$ layers can be investigated by defining cut-lines in the x direction in these regions.

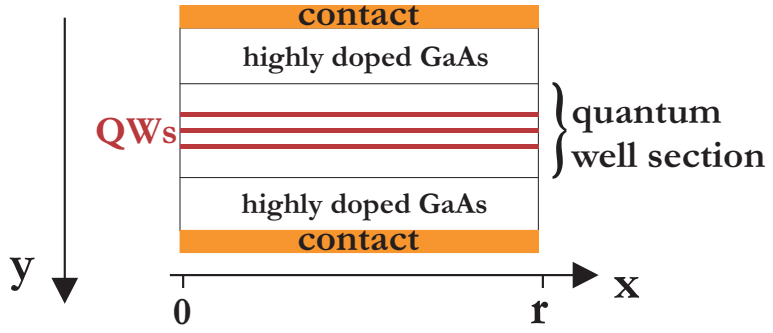

Figure C.2: The simulated structure. Only the middle layers (marked with bracket) containing the quantum wells (QWs) are changed in the designs.

C.1.1 Quantum well simultaions

The carrier distribution in three different quantum well and barrier designs has been calculated using *SILVACO*. All three designs have $InGaAs$ quantum wells, and the barriers in the three designs are $GaAsP$, $GaAs$ and $AlGaAs$. The $InGaAs/GaAsP$ design has an optical transition at 980 nm whereas the other two designs have optical transitions of 960 nm. The simulated structure is illustrated in figure C.2.

The affinity, χ, and band gap, E_{g300}, of the wells include the lowest quantum-confined state as illustrated in figure C.4. Only the conduction band to heavy hole transition is thus included in these simulations. The exact compositions and affinities and band gaps of each design are summarised in table C.1. The electron and heavy hole masses in the quantum wells are summarised in table C.2

well/barrier material	χ $[eV]$	E_{g300} $[eV]$
$In_{0.17}Ga_{0.83}As/GaAs_{0.75}P_{0.25}$ (IQE)	4.1243	1.266
$In_{0.20}Ga_{0.80}As/GaAs$ (ORC)	4.109	1.266
$In_{0.175}Ga_{0.825}As/Al_{0.15}Ga_{0.85}As$ (NBI and TAIWAN)	4.152	1.2983

Table C.1: The well and barrier material, affinities and band gap transitions in the four wafer-types, IQE, ORC, NBI and TAIWAN. Note, that the affinity of the well *includes* the lowest conduction band level and the heavy hole level.

The affinity and band gap of $AlGaAs$ is extracted from [82] and illustrated in figure C.3.

material	m_e $[m_0]$	m_{hh} $[m_0]$
$InGaAs/AlGaAs$	0.055	0.080
$InGaAs/GaAs$	0.055	0.081
$InGaAs/GaAsP$	0.055	0.081

Table C.2: Electron and heavy hole masses of the quantum wells in the three designs, calculated by the Luttinger parameter, see appendix A.

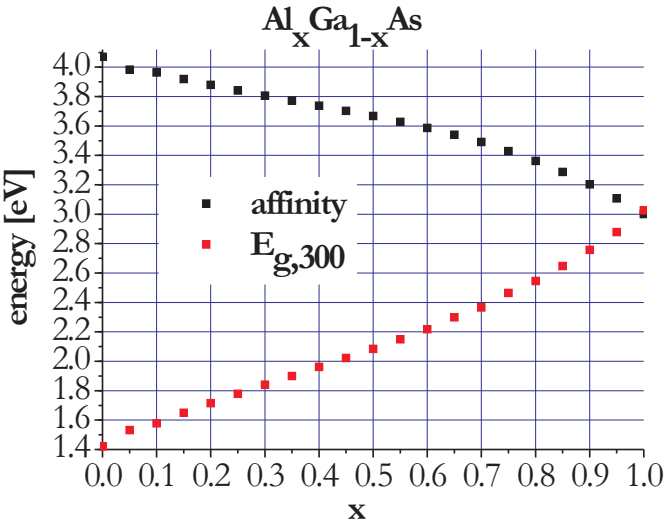

Figure C.3: The affinity, χ, and band gap, $E_{g,300}$ (at 300 K), of $Al_xGa_{1-x}As$.

The masses of the holes and electrons in the quantum wells have been adjusted by adjusting the density of states, `NV300` and `NC300`, defined by *SILVACO*

$$N_V(T) = 2\frac{2\pi m_{hh} kT}{h^2} = (\frac{T}{300})^{3/2} NV300 \tag{C.1}$$

$$N_C(T) = 2\frac{2\pi m_e kT}{h^2} = (\frac{T}{300})^{3/2} NC300 \tag{C.2}$$

Where m_{hh} and m_e is the heavy hole and electron mass of the wells. For convenience, the default values have been used, only `NV300` in the quantum

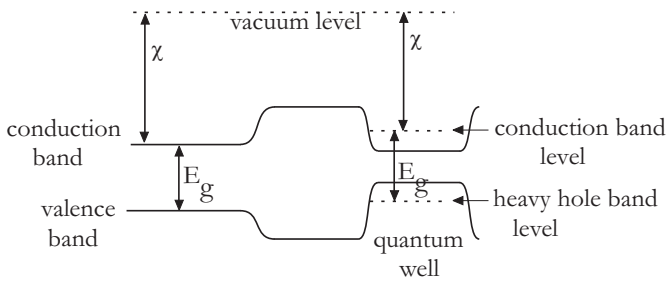

Figure C.4: Definition of affinity, χ and band gap, E_g. The band gap and affinities in the quantum well include the conduction band and heavy hole levels as illustrated.

wells has been adjusted to $1 \cdot 10^{18} cm^{-3}$ so as to fit the reduced effective mass in the valence band.

There are two types of non-radiative recombination that involve deep-level states that might stem from defects in the crystal; the Shockley-Read-Hall and the Auger processes.

The Shockley-Read-Hall-process (SHR) engages a deep-level (bound) state. The deep-level state may capture or emit electrons or holes, and the process may result in emission or absorption of photons. The SHR-process is proportional to the density of carriers and inverse proportional to the electron and hole capture times, τ_e and τ_p, and is expressed by the equation

$$R_{SRH} = \frac{pn - n_i^2}{\tau_p(n + n_i) + \tau_n(p + n_i)} \tag{C.3}$$

where p and n are the electron and hole concentrations and $n_i = n_0 p_0$ the intrinsic carrier concentration.

Modern MBEs and MOCVDs/MOVPEs grow devices with quite good crystallinity wherefore the Shockley-Read-Hall often is negligible in un-doped regions. In doped regions, however, the dopant creates impurities which gives rise to Shockley-Read-Hall processes. In the doped regions, a typical value of $\tau_n = \tau_p = 1\ ns$ has been used in the *SILVACO* simulations whereas $\tau_n = \tau_p = 1\ \mu s$ has been used in un-doped regions.

The Auger-process is a collision between two carriers. An electron may bash one electron down to the valence-band and one electron higher up in the conduction-band. Both band-to-trap-transitions and interband (*conduction band to valence band*) transitions of electrons and holes are possible. The Auger-recombination rate equals

	unit	bulk un-doped/doped	InGaAs QWs	reference
τ_p,τ_n	s	$1 \cdot 10^{-6}/1 \cdot 10^{-9}$	$1 \cdot 10^{-6}$	[129]
C_n	cm^6/s	$5 \cdot 10^{-30}$	$5 \cdot 10^{-30}$	[60]
C_p	cm^6/s	$1 \cdot 10^{-30}$	$1 \cdot 10^{-31}$	[60]
C_{opt}	cm^3/s	$1.2 \cdot 10^{-21}$	$300 \cdot 10^{-22}$	[60] [129] [130]

Table C.3: τ_n, τ_p, C_n, C_p and C_{opt} recombination coefficients used in the simulations.

$$R_{Auger} = C_n(n^2p) + C_p(n^2p^2) \tag{C.4}$$

where C_n and C_p are adjustable in *SILVACO* and set to $5 \cdot 10^{-30}$ cm^6s^{-1} and $1 \cdot 10^{-31}$ cm^6s^{-1} respectively.

The radiative transition is proportional to the carrier concentration, i.e.

$$R_{rad} = C_{opt}(pn - n_{ie}^2) \tag{C.5}$$

where C_{opt} is set to $300 \cdot 10^{-22}$ cm^3/s in the quantum wells and $1.2 \cdot 10^{-21}$ cm^3/s elsewhere.

The used values are summarised in table C.3.

C.1.2 Current spreading simulations

The current spreading in several highly doped *GaAs* layers has been simulated. The simulated structure is illustrated in figure C.5.

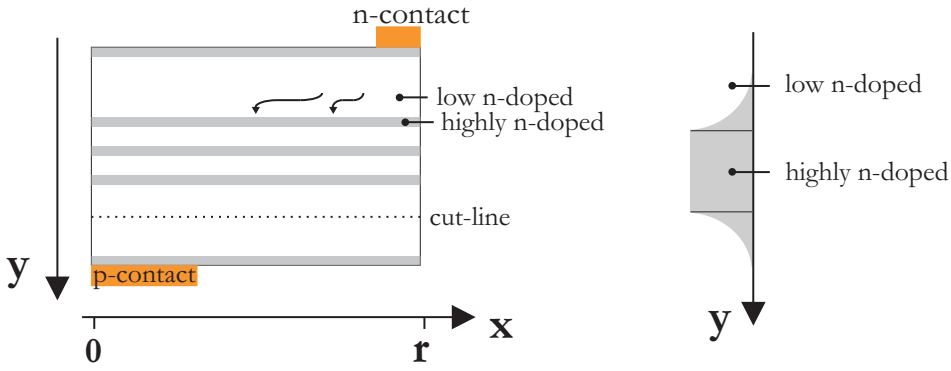

Figure C.5: The simulated structure simulated in *SILVACO*. The grey area represents the highly doped layers.

The only parameter changed in the high and low doped layers is the mobility. The mobility is in the simulations equal to

$$\mu_{n,0} = \mu_n(\frac{T_L}{300})^{-t_n}\mu_{p,0} = \mu_p(\frac{T_L}{300})^{-t_p} \tag{C.6}$$

where T_L is the lattice temperature and calculated by *SILVACO*, and the exponents, t_n and t_p are set to default values of 1 and 2.1 respectively. The temperature independent mobilities, μ_n and μ_p, are listed in table C.4 versus the carrier concentration [107].

imp. conc cm^{-3}	μ_n cm^2/Vs	μ_p cm^2/Vs
10^{16}	7000	350
10^{17}	5000	300
10^{18}	2000	200
10^{19}	1000	60

Table C.4: Electron and hole mobilities (μ_n and μ_p) versus free carrier concentration used in the *SILVACO*-simulations. Extracted from graph in [107]

Figure C.6 shows the total current density in the y direction, J_y, plotted in a cut-line positioned at the dotted line of figure 3.19. The top graph is the structure without 5 current-spreading layers, and the bottom graph is for a structure with 10 current-spreading layers. The is a slight enhancement of the current density when the number of current-spreading layers is increased from 5 to 10.

C.2 Input files

C.2.1 Quantum well simulations

```
#
# tine greibe, COM 2006 #
# FIRST STRUCTURE WITH AlGaAs 15% barriers, AlGaAs 40% claddings,
# THREE QUANTUM WELLS go atlas

options verbose mesh cyl auto

# X Mesh lines (Note Y lines defined by region statements)

x.mesh location=0 spacing=0.5
x.mesh location=5 spacing=0.5


# Define top regions going up from y=0
```

```
region num=2 material=GaAs thick=0.2 sy=0.01 acceptors=3e18 top
region num=1 material=GaAs thick=2 sy=0.02 acceptors=3e18 top

#bottom region

region num=3 material=GaAs thick=0.050 sy=0.02 acceptors=3e18 top
region num=4 material=AlGaAs x.composition=0.40 thick=0.085 ny=5
    acceptors=3e18 bottom

region num=5 material=AlGaAs x.composition=0.40 thick=0.01 ny=5
    acceptors=3e18 bottom

region num=6 material=AlGaAs x.composition=0.15 thick=0.010 ny=5
    acceptors=3e18 bottom
region num=7 material=AlGaAs x.composition=0.15 thick=0.010 ny=5
    donors=1e16 bottom

region num=8 material=AlGaAs x.composition=0.15 thick=0.005
    sy=0.001 donors=1e16 bottom
region num=9 material=InGaAs x.composition=0.835 thick=0.008
    sy=0.001 donors=1e16 bottom
region num=10 material=AlGaAs x.composition=0.15 thick=0.01
    sy=0.001 donors=1e16 bottom
region num=11 material=InGaAs x.composition=0.835 thick=0.008
    sy=0.001 donors=1e16 bottom
region num=12 material=AlGaAs x.composition=0.15 thick=0.01
    sy=0.001 donors=1e16 bottom
region num=13 material=InGaAs x.composition=0.835 thick=0.008
    sy=0.001 donors=1e16 bottom
region num=14 material=AlGaAs x.composition=0.15 thick=0.01
    sy=0.001 donors=1e16 bottom

region num=15 material=AlGaAs x.composition=0.15 thick=0.010 ny=5
    donors=1e16 bottom
region num=16 material=AlGaAs x.composition=0.15 thick=0.010 ny=5
    donors=3e18 bottom

region num=17 material=AlGaAs x.composition=0.40 thick=0.023 ny=5
    donors=3e18 bottom

region num=18 material=GaAs thick=0.067 ny=2 donor=3e18 bottom

region num=19 material=GaAs thick=0.2 sy=0.01  donor=3e18 bottom
region num=20 material=GaAs thick=2 sy=0.02  donor=3e18 bottom

elec  num=1  name=anode top
elec  num=2  name=cathode  bottom

#additional to quantum wells

material reg=9 taun0=1e-7 taup0=1e-7 augn=5e-30 augp=1e-31
    copt=300e-22 affin=4.0817 eg300=1.2959 NV300=1e18
material reg=11 taun0=1e-7 taup0=1e-7 augn=5e-30 augp=1e-31
    copt=300e-22 affin=4.0817 eg300=1.2959 NV300=1e18
material reg=13 taun0=1e-7 taup0=1e-7 augn=5e-30 augp=1e-31
    copt=300e-22 affin=4.0817 eg300=1.2959 NV300=1e18
```

```
#additional to barriers

material reg=8 taun0=1e-9 taup0=1e-9 augn=5e-30 augp=1e-31
    copt=1.2e-21 eg300=1.6498 affin=3.9186 vsatn=7.7e6 vsatp=7.7e6
material reg=10 taun0=1e-9 taup0=1e-9 augn=5e-30 augp=1e-31
    copt=1.2e-21 eg300=1.6498 affin=3.9186 vsatn=7.7e6 vsatp=7.7e6
material reg=12 taun0=1e-9 taup0=1e-9 augn=5e-30 augp=1e-31
    copt=1.2e-21 eg300=1.6498 affin=3.9186 vsatn=7.7e6 vsatp=7.7e6
material reg=14 taun0=1e-9 taup0=1e-9 augn=5e-30 augp=1e-31
    copt=1.2e-21 eg300=1.6498 affin=3.9186 vsatn=7.7e6 vsatp=7.7e6

#additional to AlGaAs 15%
material reg=6 taun0=1e-9 taup0=1e-9 augn=5e-30 augp=1e-31
    copt=1.2e-21 eg300=1.6498 affin=3.9186 vsatn=7.7e6 vsatp=7.7e6
material reg=7 taun0=1e-9 taup0=1e-9 augn=5e-30 augp=1e-31
    copt=1.2e-21 eg300=1.6498 affin=3.9186 vsatn=7.7e6 vsatp=7.7e6
material reg=15 taun0=1e-9 taup0=1e-9 augn=5e-30 augp=1e-31
    copt=1.2e-21 eg300=1.6498 affin=3.9186 vsatn=7.7e6 vsatp=7.7e6
material reg=16 taun0=1e-9 taup0=1e-9 augn=5e-30 augp=1e-31
    copt=1.2e-21 eg300=1.6498 affin=3.9186 vsatn=7.7e6 vsatp=7.7e6

#additional to AlGaAs 40% cladding
material reg=4 taun0=1e-9 taup0=1e-9 augn=5e-30 augp=1e-31
    copt=1.2e-21 affin=3.72 eg300=1.96 vsatn=7.7e6 vsatp=7.7e6
material reg=5 taun0=1e-9 taup0=1e-9 augn=5e-30 augp=1e-31
    copt=1.2e-21 affin=3.72 eg300=1.96 vsatn=7.7e6 vsatp=7.7e6
material reg=17 taun0=1e-9 taup0=1e-9 augn=5e-30 augp=1e-31
    copt=1.2e-21 affin=3.72 eg300=1.96 vsatn=7.7e6 vsatp=7.7e6

#lifetime in surrounding doped contact-regions

material reg=1 mun=3000 mup=200 copt=1.2e-21 taun0=1e-9 taup0=1e-9
material reg=2 mun=3000 mup=200 copt=1.2e-21 taun0=1e-9 taup0=1e-9
material reg=3 mun=8000 mup=400 copt=1.2e-21 taun0=1e-9 taup0=1e-9
material reg=18 mun=8000 mup=400 copt=1.2e-21 taun0=1e-9
    taup0=1e-9 material reg=19 mun=3000 mup=200 copt=1.2e-21
    taun0=1e-9 taup0=1e-9 material reg=20 mun=3000 mup=200
    copt=1.2e-21 taun0=1e-9 taup0=1e-9


#models
models srh auger optr fermidirac print

#output
output band.param con.band val.band u.auger u.radiative
    u.srh charge devdeg e.field flowlines tot.doping recomb

solve init

log outf=design1.log

save outf=design1init.str

solve prev

solve vstep=0.01 name=anode vfinal=0.1 save outf=design1.str

solve vstep=0.02 name=anode vfinal=1.34 save outf=design1_134.str
```

```
solve vstep=0.02 name=anode vfinal=1.46 save outf=design1_146.str

solve vstep=0.02 name=anode vfinal=1.55 save outf=design1_155.str

solve vstep=0.02 name=anode vfinal=1.64 save outf=design1_164.str

quit
```

C.2.2 Current-spreading layers

```
# tine greibe, COM 2005, 5 CURRENT SPREADING LAYERS

go atlas

options verbose mesh cyl auto

# X Mesh lines (Note Y lines defined by region statements)
x.mesh location=0 spacing=2
x.mesh location=49.8 spacing=0.2
x.mesh location=50 spacing=0.2

# Define top regions going up from y=0

region num=22 material=GaAs thick=0.1099 sy=0.01  donor=1e17 top
region num=21 material=GaAs thick=0.03 sy=0.006 donor=1e19 top
region num=20 material=GaAs thick=0.1099 sy=0.01 donor=1e17 top
region num=19 material=GaAs thick=0.03 sy=0.006 donor=1e19 top
region num=18 material=GaAs thick=0.1099 sy=0.01 donor=1e17 top
region num=17 material=GaAs thick=0.03 sy=0.006 donor=1e19 top
region num=16 material=GaAs thick=0.1099 sy=0.01 donor=1e17 top
region num=15 material=GaAs thick=0.03 sy=0.006 donor=1e19 top
region num=14 material=GaAs thick=0.1099 sy=0.01 donor=1e17 top
region num=13 material=GaAs thick=0.03 sy=0.006 donor=1e19 top
region num=12 material=GaAs thick=0.1099 sy=0.01 donor=1e17 top
region num=11 material=GaAs thick=0.03 sy=0.006 donor=1e19 top
region num=10 material=GaAs thick=0.1099 sy=0.01 donor=1e17 top
region num=9 material=GaAs thick=0.03 sy=0.006 donor=1e19 top
region num=8 material=GaAs thick=0.1099 sy=0.01 donor=1e17 top
region num=7 material=GaAs thick=0.03 sy=0.006 donor=1e19 top
region num=6 material=GaAs thick=0.1099 sy=0.01 donor=1e17 top
region num=5 material=GaAs thick=0.03 sy=0.006 donor=1e19 top
region num=4 material=GaAs thick=0.1099 sy=0.01 donor=1e17 top
region num=3 material=GaAs thick=0.03 sy=0.006 donor=1e19 top
region num=2 material=GaAs thick=0.1099 sy=0.01 donor=1e17 top
region num=1 material=GaAs thick=0.1 sy=0.01 donor=1e20 top


#bottom region

region num=23 material=GaAs thick=0.2 ny=10 donor=1e18 bottom
region num=24 material=GaAs thick=0.5 ny=10 donor=1e20 bottom
```

```
elec  num=1  name=cathode x.min=49.8 x.max=50 top

elec  num=2 name=anode  x.min=0 x.max=20 bottom

#addition to low-doped region

material region=2 mun=6000 mup=300
material region=3 mun=1000 mup=80
material region=4 mun=6000 mup=300
material region=5 mun=1000 mup=80
material region=6 mun=6000 mup=300
material region=7 mun=1000 mup=80
material region=8 mun=6000 mup=300
material region=9 mun=1000 mup=80
material region=10 mun=6000 mup=300
material region=11 mun=1000 mup=80
material region=12 mun=6000 mup=300
material region=13 mun=1000 mup=80
material region=14 mun=6000 mup=300
material region=15 mun=1000 mup=80
material region=16 mun=6000 mup=300
material region=17 mun=1000 mup=80
material region=18 mun=6000 mup=300
material region=19 mun=1000 mup=80
material region=20 mun=6000 mup=300
material region=21 mun=1000 mup=80
material region=22 mun=6000 mup=300

#models
models fldmob fermidirac HCTE print

#output
output band.param con.band val.band u.auger u.radiative charge
solve init

save outf=BEEWinit.str tonyplot BEEWinit.str

solve prev
solve vstep=0.001 name=anode vfinal=0.1
save outf=BEEW0_2.str
solve vstep=0.001 name=anode vfinal=0.5
save outf=BEEWFINAL.str

quit
```

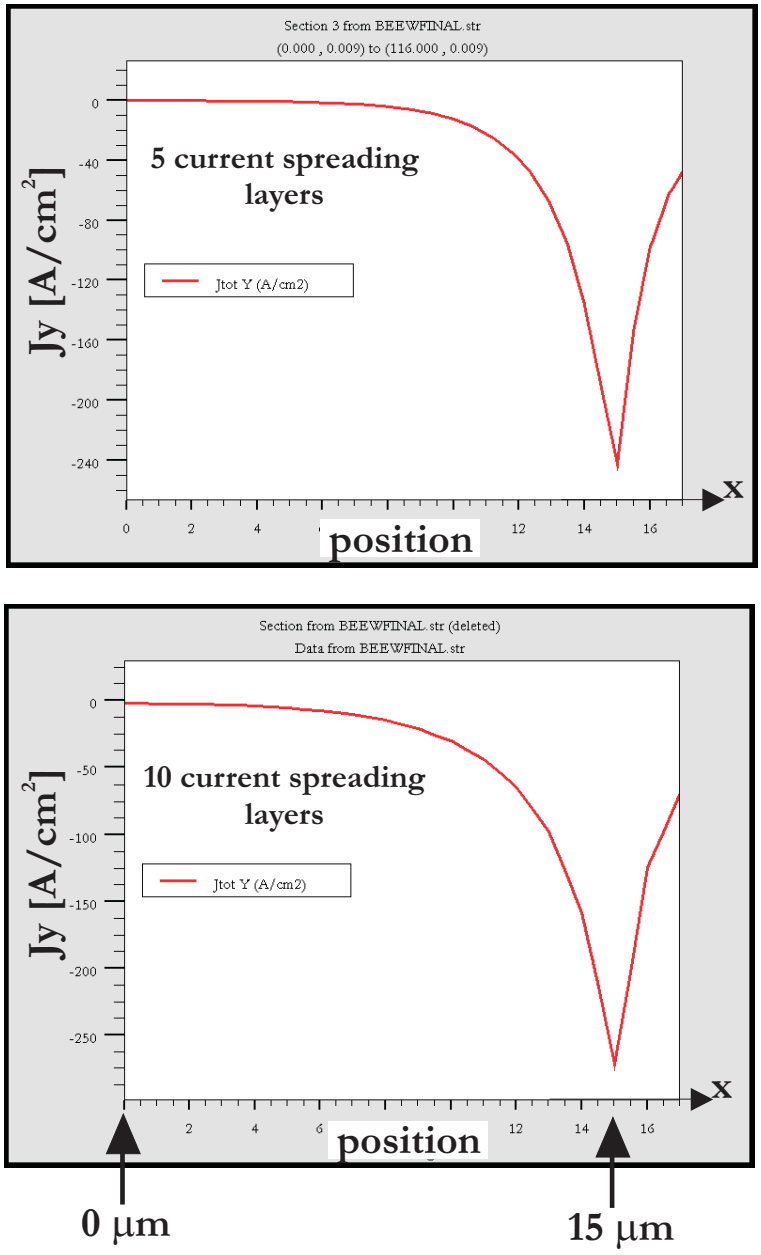

Figure C.6: The total current density in the y direction, J_y, plotted in a cut-line positioned at the dotted line of figure 3.19. The top graph is the structure without 5 current-spreading layers, and the bottom graph is for a structure with 10 current-spreading layers.

Appendix D

Growth recipes of eVCAs

The structures have been designed with use of refractive indexes of [131].

IQE-wafer							
layer no.	no. of repeats	material	comp. x	thickness nm	doping start	doping end	dopant type
24		$GaAs$		30.00	$1 \cdot 10^{20}$		$P(C)$
23		$GaAs$		10.00	$1 \cdot 10^{19}$		$P(C)$
22		$GaAs$		99.00	$1 \cdot 10^{18}$	$1 \cdot 10^{17}$	$P(C)$
21		$Al(x)GaAs$	0.70	24.80	$1 \cdot 10^{17}$		$P(C)$
20		$AlAs$		30.00	$1 \cdot 10^{17}$		$P(C)$
19		$Al(x)GaAs$	0.70	24.80	$1 \cdot 10^{17}$		$P(C)$
18		$Al(x)GaAs$	0.35	73.47	$5 \cdot 10^{17}$		$P(C)$
17	3	$GaAs$		37.54			
16		$GaAs(x)P$	0.75	6.190			
15		$In(x)GaAs$	0.17	9.000			
14		$GaAs(x)P$	0.75	12.38			
13		$In(x)GaAs$	0.17	9.000			
12		$GaAs(x)P$	0.75	12.38			
11		$In(x)GaAs$	0.17	9.000			
10		$GaAs(x)P$	0.75	6.190			
9		$GaAs$		37.54			
8		$Al(x)GaAs$	0.35	73.47	$3 \cdot 10^{17}$		$N(Si)$
7		$AlAs$		82.60	$1 \cdot 10^{17}$		$N(Si)$
6		$GaAs$		69.50	$1 \cdot 10^{17}$	$9 \cdot 10^{17}$	$N(Si)$
5		$AlAs$		82.60	$2 \cdot 10^{18}$	10^{18}	$N(Si)$
4	29	$GaAs$		69.50	$2 \cdot 10^{18}$		$N(Si)$
3		$AlAs$		82.60	$2 \cdot 10^{18}$		$N(Si)$
2		$GaAs$		50.00	$3 \cdot 10^{18}$		$N(Si)$
1		$GaAs$		$substrate$	$2 \cdot 10^{18}$		$N(Si)$

Table D.1: Growth recipe of top-emitting IQE-wafer.

ORC-wafer							
layer no.	no. of repeats		material	comp. x	thickness nm	doping cm^{-3}	dopant type
2			$GaAs$		*substrate*	$2 \cdot 10^{18}$	$N(Si)$
1		7	$AlAs$		82.93	$2 \cdot 10^{18}$	$N(Si)$
2			$GaAs$		69.50	$2 \cdot 10^{18}$	$N(Si)$
3			$AlAs$		82.93	$2 \cdot 10^{18}$	$N(Si)$
4			$Al(x)GaAs$	0.35	74.17	$3 \cdot 10^{17}$	$N(Si)$
5		3	$GaAs$		47.00		
6			$In(x)GaAs$	0.17	8.000		
7			$GaAs$		10.00		
8			$In(x)GaAs$	0.17	8.000		
9			$GaAs$		10.00		
10			$In(x)GaAs$	0.17	8.000		
11			$GaAs$		47.00		
12			$Al(x)GaAs$	0.35	74.17	$4 \cdot 10^{18}$	$P(Be)$
13			$Al(x)GaAs$	0.70	25.20	$1 \cdot 10^{19}$	$P(Be)$
14			$AlAs$		30.00	$1 \cdot 10^{19}$	$P(Be)$
15			$Al(x)GaAs$	0.70	25.20	$1 \cdot 10^{19}$	$P(Be)$
16			*deltadoping*			$1 \cdot 10^{19}$	$P(Be)$
17	20	10	$GaAs$		49.50	$5 \cdot 10^{18}$	$P(Be)$
18			$Al(x)GaAs$	0.7	1.000	$1 \cdot 10^{19}$	$P(Be)$
19			$GaAs$		1.000	$5 \cdot 10^{18}$	$P(Be)$
20			$Al(x)GaAs$	0.7	58.80	$1 \cdot 10^{19}$	$P(Be)$
21			*deltadoping*			$1 \cdot 10^{19}$	$P(Be)$
22		10	$GaAs$		1.000	$5 \cdot 10^{18}$	$P(Be)$
23			$Al(x)GaAs$	0.7	1.000	$1 \cdot 10^{19}$	$P(Be)$
24			$GaAs$		59.50	$1 \cdot 10^{20}$	$P(Be)$

Table D.2: Growth recipe of ORC-wafer

TAIWAN-wafer						
layer no.	no. of repeats	material	comp. x	thickness nm	doping cm^{-3}	dopant type
1		$GaAs$		*substrate*	$2 \cdot 10^{18}$	$N(Si)$
2		$AlAs$		81.12	$3 \cdot 10^{18}$	$N(Si)$
3		$GaAs$		67.84	$2 \cdot 10^{18}$	$N(Si)$
4	3	$AlAs$		81.12	$2 \cdot 10^{18}$	$N(Si)$
5		$GaAs$		67.84	$2 \cdot 10^{18}$	$N(Si)$
6		$Al(x)GaAs$	0.40	23.00	$2 \cdot 10^{18}$	$N(Si)$
7		$Al(x)GaAs$	0.15	10.00	$2 \cdot 10^{18}$	$N(Si)$
8		$Al(x)GaAs$	0.15	10.00		
9		$Al(x)GaAs$	0.15	5.00		
10		$In(x)GaAs$	0.165	8.000		
11		$Al(x)GaAs$	0.15	10.00		
12		$In(x)GaAs$	0.165	8.000		
13		$Al(x)GaAs$	0.15	10.00		
14		$In(x)GaAs$	0.165	8.000		
15		$Al(x)GaAs$	0.15	5.00		
16		$Al(x)GaAs$	0.15	10.00		
17		$Al(x)GaAs$	0.15	10.00	$3 \cdot 10^{18}$	$P(C)$
18		$Al(x)GaAs$	0.40	10.00	$3 \cdot 10^{18}$	$P(C)$
19		$Al(x)GaAs$	0.40	85.00	$2 \cdot 10^{18}$	$P(C)$
20		$Al(x)GaAs$	0.90	69.76	$2 \cdot 10^{18}$	$P(C)$
21		$Al(x)GaAs$	$0.90 \rightarrow 0.00$	20.00	$2 \cdot 10^{18}$	$P(C)$
22		$GaAs$		47.84	$2 \cdot 10^{18}$	$P(C)$
23		$Al(x)GaAs$	$0.00 \rightarrow 0.90$	20.00	$2 \cdot 10^{18}$	$P(C)$
24		$Al(x)GaAs$	0.90	30.16	$2 \cdot 10^{18}$	$P(C)$
25		$Al(x)GaAs$	0.98	30.00	$2 \cdot 10^{18}$	$P(C)$
26	8	$Al(x)GaAs$	$0.90 \rightarrow 0.00$	20.00	$3 \cdot 10^{18}$	$P(C)$
27		$GaAs$		47.84	$2 \cdot 10^{18}$	$P(C)$
28		$Al(x)GaAs$	$0.00 \rightarrow 0.90$	20.00	$1 \cdot 10^{18}$	$P(C)$
29		$Al(x)GaAs$	0.90	59.76	$2 \cdot 10^{18}$	$P(C)$
30	22	$Al(x)GaAs$	$0.90 \rightarrow 0.00$	20.00	$6 \cdot 10^{18}$	$P(C)$
31		$GaAs$		47.84	$3 \cdot 10^{18}$	$P(C)$
32		$Al(x)GaAs$	$0.00 \rightarrow 0.90$	20.00	$2 \cdot 10^{18}$	$P(C)$
33		$Al(x)GaAs$	0.90	59.76	$3 \cdot 10^{18}$	$P(C)$
34		$Al(x)GaAs$	$0.90 \rightarrow 0.00$	20.00	$6 \cdot 10^{18}$	$P(C)$
35		$Al(x)GaAs$	0.00	57.85	$> 5 \cdot 10^{19}$	$P(C)$

Table D.3: Growth recipe of TAIWAN-wafer

NBI-wafer						
layer no.	no. of repeats	material	comp. x	thickness nm	doping cm^{-3}	dopant type
1		$GaAs$		*substrate*		
2		$Al(x)GaAs$	0.80	313.0		
3		$GaAs$		67.85		
4		$AlAs$		81.00		
5		$GaAs$		50.00	$4 \cdot 10^{18}$	$N(Si)$
6		$GaAs$		85.70	$3 \cdot 10^{18}$	$N(Si)$
7	5	$GaAs$		57.85	$5 \cdot 10^{17}$	$N(Si)$
8		$GaAs$		20.00	$4 \cdot 10^{18}$	$N(Si)$
9		$GaAs$		57.80	$5 \cdot 10^{17}$	$N(Si)$
10		$GaAs$		67.85	$3 \cdot 10^{18}$	$N(Si)$
11		$AlAs$		20.00	$5 \cdot 10^{17}$	$N(Si)$
12		$AlAs$		21.00		
13		$Al(x)GaAs$	0.15	5.000		
14		$In(x)GaAs$	0.175	8.000		
15		$Al(x)GaAs$	0.015	10.00		
16		$In(x)GaAs$	0.175	8.000		
17		$Al(x)GaAs$	0.015	10.00		
18		$In(x)GaAs$	0.175	8.000		
19		$Al(x)GaAs$	0.15	5.000		
20		$AlAs$		29.00		
21		$AlAs$		20.00	$3 \cdot 10^{18}$	$P(Be)$
22		*deltadoping*		120*sec*		$P(Be)$
23	9	$GaAs$		67.85	$2 \cdot 10^{18}$	$P(Be)$
24		$AlAs$		81.12	$2 \cdot 10^{18}$	$P(Be)$
25		*deltadoping*		120*sec*		$P(Be)$
26	19	$GaAs$		67.85	$3 \cdot 10^{18}$	$P(Be)$
27		$AlAs$		81.12	$3 \cdot 10^{18}$	$P(Be)$
28		*deltadoping*		120*sec*		$P(Be)$
29		$GaAs$		7.850	$2 \cdot 10^{19}$	$P(Be)$
30		$GaAs$		60.00	$1 \cdot 10^{20}$	$P(Be)$

Table D.4: Growth recipe of the NBI-wafer. The $Al_{0.8}GaAs$ layer (layer no. 2) is a digital alloy of 73 layers of $1nm$ $Al_{0.15}GaAs$ and $3.3nm$ $AlAs$.

Appendix E

Table of abbreviations and symbols

A	s^{-1}	defect recombination coefficient
$A(t)$		nonlinear intensity absorption
a	cm^{-1}	absorption coefficient
A_a	cm^2	aperture area
a_g	cm^2	differential gain in linear approximation
α_H		linewidth enhancement factor
α_i	cm^{-1}	internal loss
α_m	cm^{-1}	mirror loss
AR-coating		antireflection coating
B	cm^3/s	bimolecular recombination coefficient
β_{TPA}	cm/MW	two photon absorption coefficient
β		spontaneous emission factor
χ	eV	affinity
C	cm^6/s	Auger recombination coefficient
CW		continuous wave
D_a	μm	aperture diameter
ΔR		reflectivity modulation
DBR		distributed Bragg Reflector
$E_{g,300}$	eV	Band gap at 300 K
η_i		injection efficiency
ηext		external quantum efficiency
$E_{sat,0.9}$	nJ	pulse energy to saturate eVCA 10 %
eVCA		electrically pumped vertical-cavity amplifier
eVECSEL		electrically pumped vertical-external cavity surface emitting lase
F_p	J/cm^2	pulse fluence
F_{sat}	J/cm^2	saturation fluence
FWHM		full width at half maximum
G		total gain of structure
G_s		single pass gain
Γ		confinement factor
Γ_{QW}		longitudinal confinement factor
g	cm^{-1}	gain coefficient
g_0	cm^{-1}	gain fitting parameter in first order approx.
g_i	cm^{-1}	initial gain before pulse
GDD	fs^2	group delay dispersion

HH		heavy hole
HMDS		hexamethyldisilansane
I	mA	current
I_{tr}	mA	current at transparency
J	A/cm^2	current density
J_{tr}	A/cm^2	current density at transparency
k	J/K	Boltzmanns constant
λ_B	nm	design wavelength
L_a	cm	total thickness of quantum wells
L_{eff}	cm	effective cavity-length
LED		light-emitting diode
LT		low temperature
LH		light hole
MBE		molecular beam epitaxy
MOCVD		metal-organic chemical vapor deposition
n		refractive index
N	cm^{-3}	carrier density
N_0	cm^{-3}	carrier density at operating point
N_{tr}	cm^{-3}	carrier density at transparency
ω_{long}	Hz	longitudinal mode frequency
P_{ext}	W	external input signal
PL		photoluminescence
QW		quantum well
R_0		reflectivity of eVCA with $g = 0\ cm^{-1}$
$R(0)$		small signal reflectivity (absorber)
R_{abs}		reflectivity of absorber
R_b		bottom mirror reflectivity
RCLED		resonant-cavity light-emitting diode
R_G		total reflection of structure
R_n	$s^{-1}cm^{-3}$	non-radiative recombination rate
R_{nl}		non-linear reflectivity
R_{ns}		non-saturable loss
R_{out}	$s^{-1}cm^{-2}$	recombination rate outside QWs
R_{QW}	$s^{-1}cm^{-2}$	recombination rate in QWs
R_{st}	$s^{-1}cm^{-3}$	stimulated recombination rate
R_t		top mirror reflectivity

S	cm^{-3}	photon density
τ_A	s	absorber recovery time
τ_g	s	gain recovery time
τ_p	s	pulse width
τ_R	s	repetition time
TPA		two photon absorption
V_a	cm^3	volume of active region
V_{eff}	cm^3	effect volume of structure
v_g	cm/s	group velocity
V_{tr}	V	voltage across eVCA at transparency
VCSEL		vertical-cavity surface-emitting laser
VCSOA		vertical-cavity semiconductor optical amplifier
VECSEL		vertical external-cavity surface-emitting laser
z_{eff}	cm	effective absorber thickness